

Computational modelling of fluid-structure interaction in abdominal aortic aneurysms

Citation for published version (APA):

Wolters, B. J. B. M. (2009). *Computational modelling of fluid-structure interaction in abdominal aortic aneurysms*. [Phd Thesis 1 (Research TU/e / Graduation TU/e), Biomedical Engineering]. Technische Universiteit Eindhoven. <https://doi.org/10.6100/IR642019>

DOI:

[10.6100/IR642019](https://doi.org/10.6100/IR642019)

Document status and date:

Published: 01/01/2009

Document Version:

Publisher's PDF, also known as Version of Record (includes final page, issue and volume numbers)

Please check the document version of this publication:

- A submitted manuscript is the version of the article upon submission and before peer-review. There can be important differences between the submitted version and the official published version of record. People interested in the research are advised to contact the author for the final version of the publication, or visit the DOI to the publisher's website.
- The final author version and the galley proof are versions of the publication after peer review.
- The final published version features the final layout of the paper including the volume, issue and page numbers.

[Link to publication](#)

General rights

Copyright and moral rights for the publications made accessible in the public portal are retained by the authors and/or other copyright owners and it is a condition of accessing publications that users recognise and abide by the legal requirements associated with these rights.

- Users may download and print one copy of any publication from the public portal for the purpose of private study or research.
- You may not further distribute the material or use it for any profit-making activity or commercial gain
- You may freely distribute the URL identifying the publication in the public portal.

If the publication is distributed under the terms of Article 25fa of the Dutch Copyright Act, indicated by the "Taverne" license above, please follow below link for the End User Agreement:

www.tue.nl/taverne

Take down policy

If you believe that this document breaches copyright please contact us at:

openaccess@tue.nl

providing details and we will investigate your claim.

**Computational modelling of
fluid-structure interaction in
abdominal aortic aneurysms**

Part of this research was performed in the scope of the Hemodyn project, a cooperation between Philips Healthcare (Healthcare IT – Advanced Development), Best, Eindhoven University of Technology (Department of Biomedical Engineering), and the Erasmus University (Thoraxcenter, Biomedical Engineering), Rotterdam. The Hemodyn project is partly funded by SenterNovem (Dutch Ministry of Economic Affairs).

Financial support for the publication of this thesis was kindly provided by Philips Healthcare, Best.

Copyright © 2009 by B.J.B.M. Wolters

All rights reserved. No part of this book may be reproduced, stored in a database or retrieval system, or published, in any form or in any way, electronically, mechanically, by print, photoprint, microfilm or any other means without prior written permission of the author.

A catalogue record is available from the Eindhoven University of Technology Library

ISBN: 978-90-386-1692-6

Cover design by Berent Wolters and Jorrit van Rijt (Oranje Vormgevers)

Printed by Universiteitsdrukkerij Technische Universiteit Eindhoven

Computational modelling of fluid-structure interaction in abdominal aortic aneurysms

PROEFSCHRIFT

ter verkrijging van de graad van doctor
aan de Technische Universiteit Eindhoven,
op gezag van de Rector Magnificus, prof.dr.ir. C.J. van Duijn,
voor een commissie aangewezen door het College voor Promoties
in het openbaar te verdedigen op
woensdag 15 april 2009 om 16.00 uur

door

Berent Johannes Bernardus Maria Wolters

geboren te Eindhoven

Dit proefschrift is goedgekeurd door de promotor:

prof.dr.ir. F.N. van de Vosse

Copromotoren:

dr.ir. M.C.M. Rutten

en

dr. G.W.H. Schurink

Voor mijn ouders

Contents

| | |
|--|-----------|
| Summary | ix |
| 1 General introduction | 1 |
| 1.1 Abdominal aortic aneurysm | 1 |
| 1.2 Clinical problem | 2 |
| 1.3 Wall stress modelling | 4 |
| 1.4 Endoleak modelling | 5 |
| 1.5 Objectives and study outline | 5 |
| 2 A patient-specific computational model of fluid-structure interaction in abdominal aortic aneurysms | 7 |
| 2.1 Introduction | 7 |
| 2.2 Methods | 9 |
| 2.2.1 Imaging and segmentation | 9 |
| 2.2.2 Mesh generation | 10 |
| 2.2.3 Wall deformation and blood flow models | 13 |
| 2.2.4 Implementation and simulations | 14 |
| 2.3 Results | 16 |
| 2.4 Discussion | 20 |
| 2.5 Conclusion | 24 |
| 3 Computational modelling of fluid-structure interaction in abdominal aortic aneurysms: initial wall stress effects | 25 |
| 3.1 Introduction | 25 |
| 3.2 Methods | 26 |
| 3.2.1 Geometrical model | 26 |
| 3.2.2 Wall deformation and blood flow models | 26 |
| 3.2.3 Initial wall stress model | 28 |
| 3.2.4 Implementation and simulations | 29 |
| 3.3 Results | 30 |
| 3.4 Discussion | 32 |
| 3.5 Conclusion | 34 |

| | | |
|----------|--|------------|
| 4 | Computational modelling of endoleak after endovascular repair of abdominal aortic aneurysms | 41 |
| 4.1 | Introduction | 41 |
| 4.2 | Methods | 42 |
| 4.2.1 | Geometrical model | 42 |
| 4.2.2 | Fluid-structure interaction model | 43 |
| 4.2.3 | Fluid-structure coupling | 45 |
| 4.2.4 | Lumped parameter model | 45 |
| 4.2.5 | Implementation and simulations | 47 |
| 4.3 | Results | 48 |
| 4.4 | Discussion | 50 |
| 4.5 | Conclusion | 52 |
| 5 | Assessment of endoleak significance after endovascular repair of abdominal aortic aneurysms: a lumped parameter model | 59 |
| 5.1 | Introduction | 59 |
| 5.2 | Methods | 61 |
| 5.2.1 | Aortic tree model | 61 |
| 5.2.2 | Experimental setup | 64 |
| 5.2.3 | Validation and simulations | 67 |
| 5.3 | Results | 68 |
| 5.4 | Discussion | 70 |
| 5.5 | Conclusion | 77 |
| 6 | General discussion | 79 |
| 6.1 | Introductory remarks | 79 |
| 6.2 | Study results | 79 |
| 6.3 | General conclusions and future perspective | 81 |
| | References | 84 |
| A | Appendices to Chapter 2 | 95 |
| A.1 | Centreline description | 95 |
| A.2 | Mesh transformation | 96 |
| A.3 | Point-surface projection | 97 |
| B | Appendices to Chapter 5 | 99 |
| B.1 | Windkessel module parameters | 99 |
| B.2 | Physiologic model properties | 100 |
| B.3 | Experimental model properties | 100 |
| | Samenvatting | 103 |
| | Dankwoord | 105 |
| | Curriculum vitae | 107 |

Summary

Computational modelling of fluid-structure interaction in abdominal aortic aneurysms

An abdominal aortic aneurysm (AAA) is a localised dilatation of the abdominal aorta. Rupture of an AAA can lead to a life-threatening situation for the patient. For a diagnosed AAA, rupture can be prevented by placing a regular vascular graft by means of transabdominal surgery, or by placing a so-called stent-graft by means of a minimally invasive procedure (endovascular repair). For the patient, transabdominal surgery is a relatively tough procedure. Nevertheless, after placement of a regular vascular graft, the risk of rupture is decreased rather permanently. The procedure of endovascular repair, on the other hand, is relatively easy on the patient. After placement of an endoprosthesis, however, there is a considerable risk of late complications. As a result, patients undergoing endovascular repair need extensive follow-up.

In the decision on surgical intervention, the risks associated with the surgery itself and those associated with post-operative complications need to be weighed against the risk of rupture. This is not a trivial procedure. In current clinical practice, the risk of rupture is considered high when the AAA diameter exceeds 5.5 cm. However, it is uncertain that a smaller AAA will not rupture. A larger AAA, on the other hand, could remain stable. With respect to post-operative complications, in endovascular repair, the most important complication is that of endoleak, or leakage into the excluded cavity of the AAA. Although it has been demonstrated that endoleak leads to a persistent risk of rupture and that it therefore needs to be counteracted, the causes and effects of endoleak on a patient-specific basis remain unclear.

The objectives of the studies described in this thesis are (1) to provide computational tools for improved decision making in the treatment of AAA and (2) to provide insight into the level of detail required by such models. In particular, these objectives are pursued by application of computational fluid-structure interaction (FSI) modelling techniques. It is assumed that these techniques can help to better predict the development and rupture of an AAA before treatment, and to determine the effects of endoleak on the risk of rupture after treatment. These objectives are based on previous studies in which a relationship was found between the risk of rupture and the numerically computed stress in the vessel wall. Furthermore, these studies build on previous studies of mechanical and fluid-dynamical quantities in patient-specific models of AAA and on experimental studies into the effects of endoleak on the pressure

in the excluded cavity of the AAA after treatment.

With respect to the modelling of FSI in AAA before treatment, among other things, a method for generating patient-specific hexahedral finite element meshes of the AAA lumen and wall is developed. The purpose of such a mesh is illustrated by a simulation of the wall stress, the blood velocity distribution, and the wall shear stress (WSS) in a characteristic AAA. Furthermore, the importance of incorporating the initial wall stress is studied. In previous studies of FSI in AAA, the initial stress, or the wall stress already present at diastolic pressure, was not incorporated. However, it appears that neglect of the initial stress leads to an overestimation of the wall deformation, overall stress level, and peak wall stress. In addition, it promotes a more smooth stress distribution and it further leads to an underestimation of the WSS. Nevertheless, it also appears that the WSS pattern in the presence of initial stress can be well approximated using a rigid geometry.

With respect to the modelling of endoleak, among other things, the benefits of the so-called lumped parameter modelling method are assessed as compared to coupled FSI. Both modelling methods are used to study the pressure in the excluded cavity of an AAA after treatment for different degrees of endoleak and for different values of the endoprosthesis compliance. From the results, it appears that for the modelling of endoleak, the lumped parameter modelling method provides a useful and cheap alternative to coupled FSI, and that the pressure in the cavity of the AAA computed using such a model could serve well as a boundary condition for simulations of the vessel wall to determine the risk of rupture after treatment. Furthermore, the lumped parameter modelling method is applied to reconcile various results of previous experimental endoleak studies. It appears that in the presence of endoleak, the mean pressure in the AAA cavity is mainly dependent on the resistance of a possible outflow tract, while the pulse pressure is dependent on both the size of the endoleak and the compliance of the endoprosthesis.

The results and conclusions of this thesis are mainly of importance within the scope of previous and future studies aimed at better understanding the development and pathogenesis of AAA and significance of endoleak after endovascular repair. For application of the developed models in clinical practice, additional model developments are required and the added value of the simulated quantities in clinical decision making needs to be further demonstrated. Nevertheless, based on the demonstrated possibilities for simulating the effects of endoleak using the lumped parameter modelling method and for simulating the WSS in the presence of initial wall stress using a rigid wall model, it can be concluded that for the simulation of quantities relevant for the treatment of AAA, FSI not necessarily needs to be incorporated explicitly. With this conclusion, this thesis provides the foundation for a simplification of the decision making tools being developed, that is expected to positively influence their impact in clinical practice.

Chapter 1

General introduction

1.1 Abdominal aortic aneurysm

An abdominal aortic aneurysm (AAA) is a permanent localised dilatation of the abdominal aorta. AAAs are generally located between the branch points of the renal arteries supplying blood to the kidneys, and the bifurcation of the aorta into the iliac arteries supplying blood to the lower limbs and the pelvic region (see Figure 1.1(a)). In general, a dilatation of an artery is classified as an aneurysm when the increase in diameter exceeds 50 percent of the expected normal diameter (Johnston *et al.*, 1991). For the abdominal aorta, this means that an aneurysm is present when the vessel diameter exceeds about 3.0 cm. In many AAAs, the channel available for blood flow, or lumen, is limited by a mass of clotted blood, or thrombus, deposited onto the vessel wall (see Figure 1.1(b)). Typical risk factors for the occurrence of AAA are male gender, advanced age, and Caucasian descent. Other indicators include a positive family history and established cardiovascular risk factors such as smoking, hypertension, and hypercholesterolemia (Pleumeekers *et al.*, 1994; Singh *et al.*, 2001). In a population-based study of around 6400 men and women aged 25 to 84 years, aneurysms were found present in around 9 percent of the men and 2 percent of the women (Singh *et al.*, 2001).

Although the mechanism of AAA formation is not fully understood, AAAs are believed to originate in local weakening of the aortic wall. In healthy aortic wall tissue, the forces resulting from the blood pressure acting on the vessel wall are borne by a network of elastin and collagen fibers. In aneurysmatic tissue, the elastin content is decreased due to increased activity of proteolytic enzymes, and the load is progressively shifted towards the collagen. Due to uncoiling of the collagen fibers, the diseased part of the aorta is left dilated and less distensible. Depending on the collagen properties and the net effect of collagen degradation and remodelling, the dilated aorta is prone to further dilation and rupture (MacSweeney *et al.*, 1994; Wills *et al.*, 1996). In addition, it is suspected that AAA formation is influenced by haemodynamic factors. It seems reasonable to assume that specific changes in the architecture of the aorta resulting from the normal aging process play a role by affecting for instance the

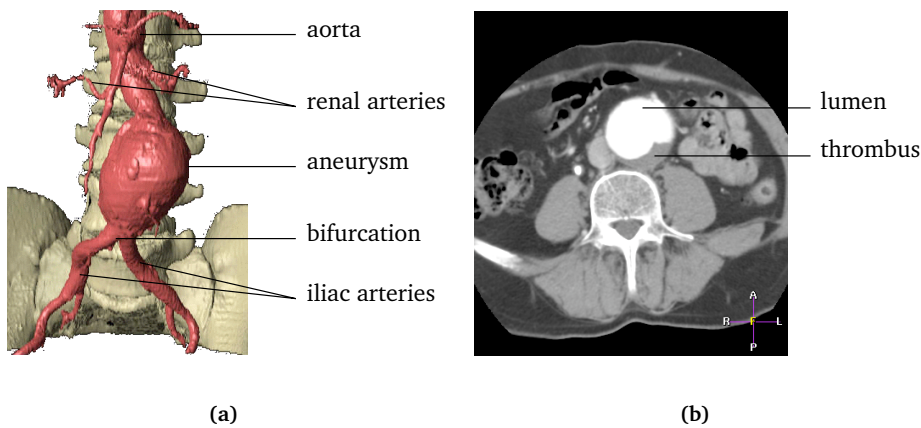


Figure 1.1: 3-D Visualisation (a) and CT angiographic image (b) of an abdominal aortic aneurysm (Philips Healthcare).

speed of the arterial pulse wave and the reflection of the pulse wave at the aortic bifurcation (Lasheras, 2007). Based on the demonstrated effect of the wall shear stress (WSS) on endothelial cell expression and wall remodelling (Sho *et al.*, 2004), it is also hypothesised that AAA formation is influenced by WSS. Specific patterns of high and low WSS occurring in aneurysms also have been related to thrombus formation (Bluestein *et al.*, 1996), which in turn has been related to wall inflammation, local hypoxia, and wall weakening (Vorp *et al.*, 2001; Kazi *et al.*, 2003).

The main risk associated with AAA is that of rupture. The overall mortality associated with the rupture of AAA is 60 to 80 percent (Singh *et al.*, 2001). For patients that reach the hospital alive, these figures are still around 25 to 50 percent (Verhoeven *et al.*, 2008). AAA rupture accounts for 1.2 percent of deaths in men and 0.6 percent in women over the age of 65, and ranks the 13th cause of death in the United States (Wolf and Bernstein, 1994). The most important indicators of AAA rupture risk are the maximal transverse diameter and the expansion rate (Choke *et al.*, 2005). Biological risk factors include female gender, hypertension, chronic obstructive pulmonary disease, and smoking (Pleumeekers *et al.*, 1994; Cronenwett, 1996; Choke *et al.*, 2005). Unruptured AAAs are mostly asymptomatic, however, and therefore only get diagnosed by chance (Karkos *et al.*, 2000).

1.2 Clinical problem

The main treatment option for AAA is to depressurise the aneurysm by excluding it from the circulation, either through conventional transabdominal surgery (open repair), or through the less invasive method of endovascular aneurysm repair (EVAR). In open repair, as introduced by Dubost *et al.* (1952), the wall is excluded by means of

a regular vascular graft sutured to healthy parts of the vessel. Due to significant morbidity rates associated with this procedure, open repair is mainly used for younger, otherwise healthy patients. In EVAR, as introduced by Parodi *et al.* (1991), the exclusion is performed using a self-expandable stent-graft placed inside the AAA by means of a guide wire inserted in the femoral artery. As compared to open repair, EVAR is associated with reduced perioperative mortality and shorter hospital stay (Greenhalgh *et al.*, 2004). Therefore, in the case of elderly patients with comorbidities such as other types of cardiovascular disease, EVAR is the most feasible option. In the long term, however, the perioperative survival advantage of EVAR is not sustained (Blankensteijn *et al.*, 2005). Further, because of a considerable risk of late complications, patients undergoing EVAR need extensive follow-up (Leurs *et al.*, 2007).

The decision on surgical intervention is made by weighing the cumulative risks associated with the surgery against the risk of rupture. In current clinical practice, the risk of rupture is assessed based on the maximal transverse AAA diameter as visualised on CT angiographic images, and surgery is considered necessary when the diameter exceeds 5.5 cm, or when the expansion rate exceeds 1 cm per year (UK Small Aneurysm Trial participants, 2002; Lederle *et al.*, 2002a). Although rupture is highly related to increased aneurysm size (Szilagyi *et al.*, 1972; Lederle *et al.*, 2002b), rupture can also occur in smaller AAAs (UK Small Aneurysm Trial participants, 1998; Lederle *et al.*, 2002a). Therefore, in some cases, surgical repair may already be advisable at an earlier stage. To find more accurate rupture risk predictors than the diameter, geometric properties other than the diameter as well as non-geometric patient characteristics have been considered (Hatakeyama *et al.*, 2001; Fillinger *et al.*, 2004). The most prominent trend, however, is to study the mechanical behaviour of the AAA wall using patient-specific computational models. As rupture is characterised by mechanical failure, it is generally believed that the risk of rupture can be assessed better based on the wall stress distribution computed with these models. In some studies, the peak wall stress has already been related to the occurrence (Fillinger *et al.*, 2002, 2003) and location (Venkatasubramaniam *et al.*, 2004) of rupture. The use of a patient-specific pressure load in such models seems of critical importance (Truijers *et al.*, 2007). For AAAs under observation, peak wall stress seems a better predictor of rupture than diameter (Fillinger *et al.*, 2003).

The treatment success is determined by the absence of leakage, or endoleak, after surgery, and in the long term by the stabilisation or decrease of the AAA volume. In general, AAAs that continue to expand after surgery have been associated with significantly higher intra-aneurysm pressure than shrinking aneurysms, and are therefore subject to continued risk of rupture (Dias *et al.*, 2004). Persistent or recurrent pressurisation of the aneurysm sac without evidence of endoleak is called endotension (White and May, 2000). Possible causes of endotension are pressure transmission through thrombus, presence of an endoleak not amenable to detection, and ultrafiltration through the graft material (Hinchliffe and Hopkinson, 2003). In EVAR, endotension occurs in about 1 percent of the patients without endoleak (Buth *et al.*, 2003). Endoleak is generally defined as persistent flow between the stent-graft and the excluded vessel wall (White *et al.*, 1997, 1998). Post-operative endoleak occurs in about 20 percent of all patients undergoing EVAR (van Marrewijk *et al.*, 2002),

and can be classified according to the origin of the flow. Since all types of endoleak lead to continued pressurisation of the aneurysmal sac (Baum *et al.*, 2001), endoleak is assumed responsible for continued risk of rupture. For endoleak related to the stent-graft attachment sites (type I) and endoleak related to stent-graft failure and disconnection (type III), this effect has been demonstrated in a clinical study (van Marrewijk *et al.*, 2002). Although not significantly associated with increased risk of rupture, endoleak due to collateral perfusion (type II endoleak) has been associated with both AAA pressurisation (Dias *et al.*, 2004) and expansion (van Marrewijk *et al.*, 2004). On a patient-specific basis, however, the nature and significance of endoleak remain poorly understood (Veith *et al.*, 2002).

1.3 Wall stress modelling

In the search for better predictors of AAA rupture risk, previously, several studies of the AAA wall stress based on computational models have been reported in literature. Models based on idealised geometries were used to show that AAA wall stress is significantly reduced in the presence of thrombus, depending on its size and constitutive properties (Inzoli *et al.*, 1993; Mower *et al.*, 1997; Di Martino *et al.*, 1998; Di Martino and Vorp, 2003). Similarly, it was shown that the wall stress is increased in the presence of atherosclerotic plaques and calcifications (Inzoli *et al.*, 1993; Speelman *et al.*, 2007). Furthermore, the wall stress distribution was shown to be dependent on the actual shape of the AAA as well as its maximum diameter (Stringfellow *et al.*, 1987; Vorp *et al.*, 1998; Hua and Mower, 2001). As the in-vivo shape of AAA is highly complex and far from axisymmetric (Sacks *et al.*, 1999), this means that for patient-specific wall stress assessment, finite element models need to be based on detailed three-dimensional descriptions of the AAA geometry. Indeed, models based on patient-specific geometries show complex wall stress distributions (Raghavan and Vorp, 2000b; Thubrikar *et al.*, 2001b; Fillinger *et al.*, 2002), which again are influenced by the presence of thrombus (Wang *et al.*, 2002).

To improve wall stress based indications of rupture risk and better understand AAA formation and development, patient-specific computational models have been developed including the effects of fluid-structure interaction (FSI). Such models have been applied to study for instance the effects of fluid dynamic loading and wall distensibility, and additional flow features such as the wall shear stress (WSS) (Di Martino *et al.*, 2001; Leung *et al.*, 2006; Papaharilaou *et al.*, 2007; Scotti and Finol, 2007). Further effort has been put into the development of methods for incorporating the initial wall stress, meaning the stress already present in the AAA wall at diastolic pressure, and to study the effects thereof on computed model results (Raghavan *et al.*, 2006; Lu *et al.*, 2007a,b; De Putter *et al.*, 2007). Incorporation of the initial stress has been found to affect the peak wall stress by up to 10 to 20 percent, depending on the compliance of the AAA wall material (Lu *et al.*, 2007b). Further, several studies have focussed on the determination of the mechanical properties of the AAA wall tissue, which serve as input to the computational models (e.g., Raghavan and Vorp, 2000a; Thubrikar *et al.*, 2001a; Van Dam *et al.*, 2008).

1.4 Endoleak modelling

The causes and effects of endoleak have mainly been investigated in experimental studies. In an animal study of saccular aneurysms connected to the aorta by an endoleak channel, Schurink *et al.* (2000a) showed that irrespective of the channel dimensions, endoleak yields an identical intrasac mean pressure compared to the systemic mean pressure measured in the aorta. The intrasac pressure pulsatility, however, was inversely related to the endoleak channel diameter, and was obliterated by thrombosis of the channel. The first finding was confirmed both by Skillern *et al.* (2002) using animal models of an excluded aneurysm with an attachment site failure and by Chong *et al.* (2003) using setups of an excluded aneurysm with either an attachment site failure or a partially permeable stent-graft. The second finding was also confirmed by Chong *et al.* (2003), who reported a decrease of the intrasac pressure pulsatility for lesser degrees of endoleak. Further, in a study on thrombosed endoleak channels by Mehta *et al.* (2001), it was reported that the reduction of the intrasac peak systolic pressure was inversely proportional to the channel diameter and directly proportional to its length. In studies of setups of incompletely excluded AAAs it was further shown that the intrasac pressure due to endoleak is reduced in the presence of an outflow tract formed by a branching vessel (Parodi *et al.*, 2001; Chong *et al.*, 2003). Finally, pulsatility of the intrasac pressure was also shown present in fully excluded aneurysms in both studies of experimental setups (Parodi *et al.*, 2001; Chong *et al.*, 2003; Gawenda *et al.*, 2003a; Mehta *et al.*, 2003) and animal studies (Skillern *et al.*, 2002).

Only a small number of studies on endoleak has focussed on the application of computational models. The main aim of these studies was to better understand the effects of endoleak on the aneurysm intrasac pressure using models based on coupled FSI techniques. In a study by Li and Kleinstreuer (2005b), endoleak was represented by small changes of the fluid volume contained by the aneurysmal sac. It was concluded that for small endoleaks, the intrasac pressure is greatly increased compared to full exclusion. In another study by Li and Kleinstreuer (2006), endoleak was represented by flow through a physical connection of the aneurysmal sac with the aortic lumen. In this study, it was concluded that relatively large endoleaks yield intrasac pressures close to the systemic pressure. Based on various simulations, the above authors further concluded that in the absence of endoleak, intrasac pressure pulsatility can still be present due to interactions between the luminal blood flow, the stent-graft, the blood comprised by the aneurysm, and the aneurysm wall (Li and Kleinstreuer, 2005a,b).

1.5 Objectives and study outline

The objectives of this thesis are (1) to provide computational tools for improved decision making in the treatment of AAA and (2) to provide insight into the level of detail required by such models. In particular, these objectives are pursued by application of computational FSI modelling techniques. The objectives arise from the need for

optimisation of clinical treatment to minimise morbidity and mortality rates and cost. By contributing to better insight into the pathogenesis of AAA and helping to predict AAA development and rupture on a patient-specific basis, computational models of FSI in AAA before treatment could support in selecting the optimal moment for surgical intervention and reducing the overall risk for the patient. Computational models of endoleak, on the other hand, could help to understand the effects of endoleak on the post-operative risk of rupture in the case of incomplete exclusion, both by providing pressure boundary conditions for 3D wall stress simulations and by supporting the interpretation of measurements from implantable pressure sensors.

Computational modelling of FSI in AAA before treatment is the main focus of Chapters 2 and 3. In Chapter 2, to facilitate the incorporation of FSI in the assessment of the AAA wall stress, a method for generating patient-specific hexahedral finite element meshes of the AAA lumen and wall is presented. The applicability of the meshes is illustrated by an FSI simulation in a characteristic AAA. In Chapter 3, the importance of incorporating the initial wall stress is investigated. It is determined to what extent the initial stress affects the wall deformation, the wall stress distribution, the velocity distribution, and WSS in an ideal AAA. Additionally, by varying the wall thickness and considering a rigid wall case, the effects of the wall distensibility are studied, and it is determined to what extent the initial stress affects the differences between rigid and distensible wall model results.

Computational modelling of endoleak is the main focus of Chapters 4 and 5. In Chapter 4, the benefits of lumped parameter models are assessed as compared to models based on coupled FSI. Both types of models are used to study the aneurysm intrasac pressure in an incompletely excluded AAA for different endoleak sizes and different values of the stent-graft compliance. Based on the agreement of the results, it is determined whether the lumped parameter modelling method provides a useful alternative to coupled FSI for modelling the aneurysm intrasac pressure in the presence of endoleak. In Chapter 5, a lumped parameter model of endoleak is used to both reconcile and physically substantiate various findings of experimental endoleak studies described in literature. To this end, a computational model of an incompletely excluded AAA is developed and validated using an experimental setup. Furthermore, a model of an incompletely excluded aneurysm is incorporated in a model of the arterial tree to study the effects of endoleak on the aneurysm intrasac pressure in a physiologic context.

In Chapter 6, the main results of the different studies are summarised, general conclusions are drawn, and a future perspective is presented regarding the implications of the study results for additional research and clinical practice.

Chapter 2

A patient-specific computational model of fluid-structure interaction in abdominal aortic aneurysms*

2.1 Introduction

An abdominal aortic aneurysm (AAA) is a dilatation of the abdominal aorta which may be prone to rupture. In current clinical practice, surgical treatment of AAA is generally considered necessary when the maximal diameter exceeds 5 to 6 cm (Lederle *et al.*, 2002a). Although rupture is highly related to increased aneurysm size (Szilagyi *et al.*, 1972; Lederle *et al.*, 2002b), rupture also occurs in smaller aneurysms (UK Small Aneurysm Trial participants, 1998; Lederle *et al.*, 2002a). To find more accurate rupture risk predictors, both geometric properties other than the diameter and non-geometric patient characteristics have been considered (Hatakeyama *et al.*, 2001; Fillinger *et al.*, 2004). Yet, due to recent improvements in imaging and segmentation, the most prominent trend in AAA rupture risk assessment is to study the mechanical behaviour of AAA by means of computational models (Stringfellow *et al.*, 1987; Inzoli *et al.*, 1993; Mower *et al.*, 1997; Di Martino *et al.*, 1998; Vorp *et al.*, 1998; Raghavan and Vorp, 2000b; Hua and Mower, 2001; Di Martino *et al.*, 2001; Thubrikar *et al.*, 2001b; Fillinger *et al.*, 2002; Wang *et al.*, 2002; Di Martino and Vorp, 2003; Fillinger *et al.*, 2003; Venkatasubramaniam *et al.*, 2004). As rupture is charac-

*The contents of this chapter are based on *Med Eng Phys*, 27, 871–883, 2005:

**A patient-specific computational model of fluid-structure interaction
in abdominal aortic aneurysms**

B.J.B.M. Wolters, M.C.M. Rutten, G.W.H. Schurink, U. Kose, J. de Hart, F.N. van de Vosse

terised by mechanical failure, it is generally believed that the wall stress distribution computed with these models could help to better assess AAA rupture risk.

Several studies of AAA wall stress by means of computational models have been reported in literature. Models based on idealised geometries were used to show that AAA wall stress is significantly reduced in the presence of intraluminal thrombus (ILT), depending on its size and constitutive properties (Inzoli *et al.*, 1993; Mower *et al.*, 1997; Di Martino *et al.*, 1998; Di Martino and Vorp, 2003). Similarly, the presence of atherosclerotic plaques was shown to have an increasing effect on the wall stress (Inzoli *et al.*, 1993). Further, the wall stress distribution was shown to be dependent on the actual shape of the AAA as well as its maximum diameter (Stringfellow *et al.*, 1987; Vorp *et al.*, 1998; Hua and Mower, 2001). As the in-vivo shape of AAA is highly complex and far from axisymmetric (Sacks *et al.*, 1999), this means that for patient-specific wall stress assessment, finite element models need to be based on detailed three-dimensional descriptions of the AAA geometry. Indeed, models based on patient-specific geometries show complex wall stress distributions (Raghavan and Vorp, 2000b; Thubrikar *et al.*, 2001b; Fillinger *et al.*, 2002), which again are influenced by the presence of ILT (Wang *et al.*, 2002). In some studies, the peak wall stress computed with these models has already been related to the occurrence (Fillinger *et al.*, 2002, 2003) and location (Venkatasubramaniam *et al.*, 2004) of rupture. For AAAs under observation, peak wall stress seems a better predictor of rupture than diameter (Fillinger *et al.*, 2003).

Although the behaviour of the AAA wall inherently is influenced by the behaviour of the blood that it comprises, previously published models for patient-specific assessment of the wall stress predominantly did not include fluid-dynamic effects. By application of the concept of fluid-structure interaction (FSI) to the cardiovascular system, the means for incorporating such effects however are available (van de Vosse *et al.*, 2003). Still, to the authors' knowledge, there has been only one study regarding FSI in patient-specific AAA (Di Martino *et al.*, 2001). In that study, the pressure load applied to the wall model resulted from a coupled simulation of the blood velocity and pressure fields. In the above mentioned structure based models, the load was set to a characteristic peak systolic value. Although the latter approach may give good insight into the spatial variation of the wall stress, it does not represent the in-vivo loading pattern.

In order to facilitate the incorporation of fluid-structure interaction in the assessment of AAA wall stress, in this study, a method for generating patient-specific hexahedral finite element meshes of the AAA lumen and wall is presented and its applicability is illustrated by simulations in a characteristic AAA. In addition to the possibility of computing the wall response to actual fluid dynamic loading, the incorporation of the lumen mesh allows for studies of the wall shear stress (WSS). As certain sequences of high and low WSS have been related to arterial wall remodelling (Sho *et al.*, 2004) and specific patterns of high and low WSS occurring in aneurysms have been related to thrombus formation (Bluestein *et al.*, 1996), modelling the WSS could be essential for modelling the pathogenesis of AAA and its development over time.

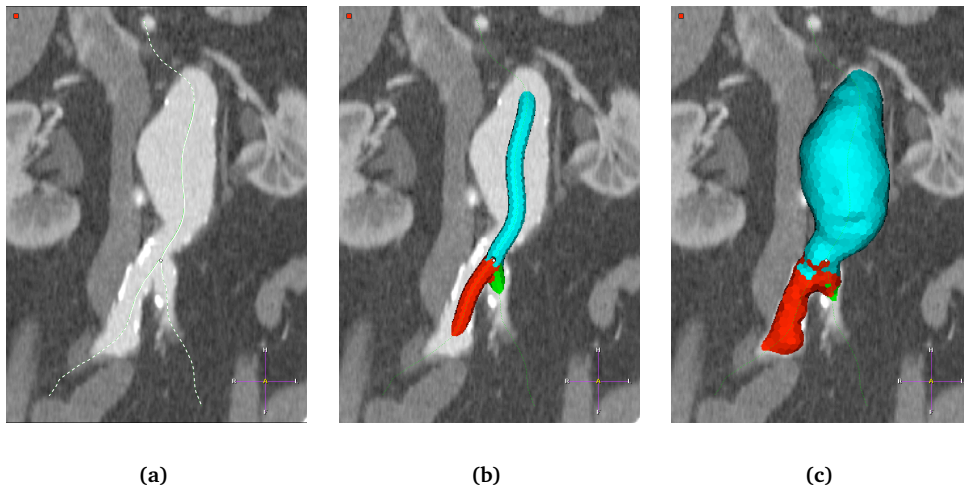


Figure 2.1: Segmentation of the AAA lumen using a 3D Active Object: centrelines (a); 3DAO initial shape (b); 3DAO final shape (c) (Philips Healthcare).

2.2 Methods

2.2.1 Imaging and segmentation

The patient-specific geometry used in this study is derived from a CT angiographic (CTA) image of an AAA that contained virtually no thrombus. The image was acquired at the University Hospital Maastricht using a Toshiba Aquilion spiral CT scanner (Toshiba Medical Systems Corporation, Tochigi, Japan). A typical AAA CTA protocol was applied, in which the scan was performed during one breath-hold of the patient to reduce motion artefacts. The slice thickness was 2 mm and the 2-D image size was 400×400 mm. At a resolution of 512×512 , the resulting voxel size was $0.78 \times 0.78 \times 2$ mm. A coronal cross section of the image is depicted in Figures 2.1(a) to 2.1(c).

From the CTA image, descriptions of the centrelines and the boundary surface of the lumen of the AAA are determined by means of semi-automated centreline tracking and segmentation using a 3-D Active Object (3DAO) (Gerard *et al.*, 2002). The centrelines are tracked between user-specified end points using a minimum cost path approach (Wink *et al.*, 2002). The 3DAO-technique of segmentation is a deformable-model type of technique, a prototype of which is implemented on the EasySCIL software platform, a development version of the EasyVision clinical image processing workstation (Philips Healthcare, Best, The Netherlands) (Breeuwer *et al.*, 2004). The 3DAO is initialised in a tubular shape around the tracked centrelines, after which it is incrementally inflated until it matches the lumen boundary. The image considered in this study was segmented between slightly above and below the levels of the renal

arteries and the iliac bifurcation, respectively. The tracked centrelines are shown in Figure 2.1(a). The tubular and final shapes of the 3DAO are shown in Figures 2.1(b) and 2.1(c).

2.2.2 Mesh generation

In order to generate a patient-specific combined mesh of the AAA lumen and wall, a standardised bifurcated mesh is transformed based on the centrelines and the boundary surface of the segmented AAA. The standardised mesh comprises both fluid and solid domains. The geometry of the mesh is based on the shape of three intersecting tubes, as shown in Figure 2.2(a). The topology of the fluid domain is chosen such that it contains smaller elements at locations closer to the wall. Both the fluid and wall domains consist of quadratic 27-noded elements. The boundary surface is represented by a surface triangulation (see Figure 2.2(b)). Due to the bifurcation, there are two centrelines, each running from the proximal end of the trunk of the bifurcation to either of the left and right distal branch ends (see Figure 2.2(c)). The centrelines are represented by sets of discrete points.

First, based on the centrelines, the fluid domain of the standardised mesh is transformed into a patient-specific initial shape that is orientated along the lumen of the AAA. To this end, the original centrelines are reconfigured as depicted in Figure 2.2(c), and of each of the centrelines a continuous description is determined (see Appendix A.1). Next, the fluid domain of the standardised mesh is transformed to an initial patient-specific mesh, that subsequently is orientated along the reconfigured centrelines. The latter transformation is based on local coordinate systems that are defined along the centrelines based on their continuous descriptions (see Appendix A.2). Finally, to correct for distorted elements that may occur at the connection of the trunk and the two branches, Laplacian smoothing is applied to the nodal points of the mesh. For a point \mathbf{x}_i , a new position \mathbf{x}'_i is calculated as

$$\mathbf{x}'_i = \mathbf{x}_i + \lambda \Delta \mathbf{x}_i, \quad (2.1)$$

with λ a scale factor and $\Delta \mathbf{x}_i$ the discrete Laplacian, defined as

$$\Delta \mathbf{x}_i = \sum_{j \in N_i} w_{ij} (\mathbf{x}_j - \mathbf{x}_i), \quad (2.2)$$

with N_i the set of indices of the nodal points connected to point i through element edges and w_{ij} the weights of these points, defined as

$$w_{ij} = \frac{\|\mathbf{x}_i - \mathbf{x}_j\|_2^{-1}}{\sum_{k \in N_i} \|\mathbf{x}_i - \mathbf{x}_k\|_2^{-1}}. \quad (2.3)$$

In this procedure, the planarity of the inflow and outflow surfaces is retained by means of hierarchical constraints, as described by Taubin (1995). The procedure is repeated 10 times with $\lambda = 0.25$. These parameters were chosen to obtain an only moderate degree of smoothing, to prevent the collapse of outer layer mesh elements.

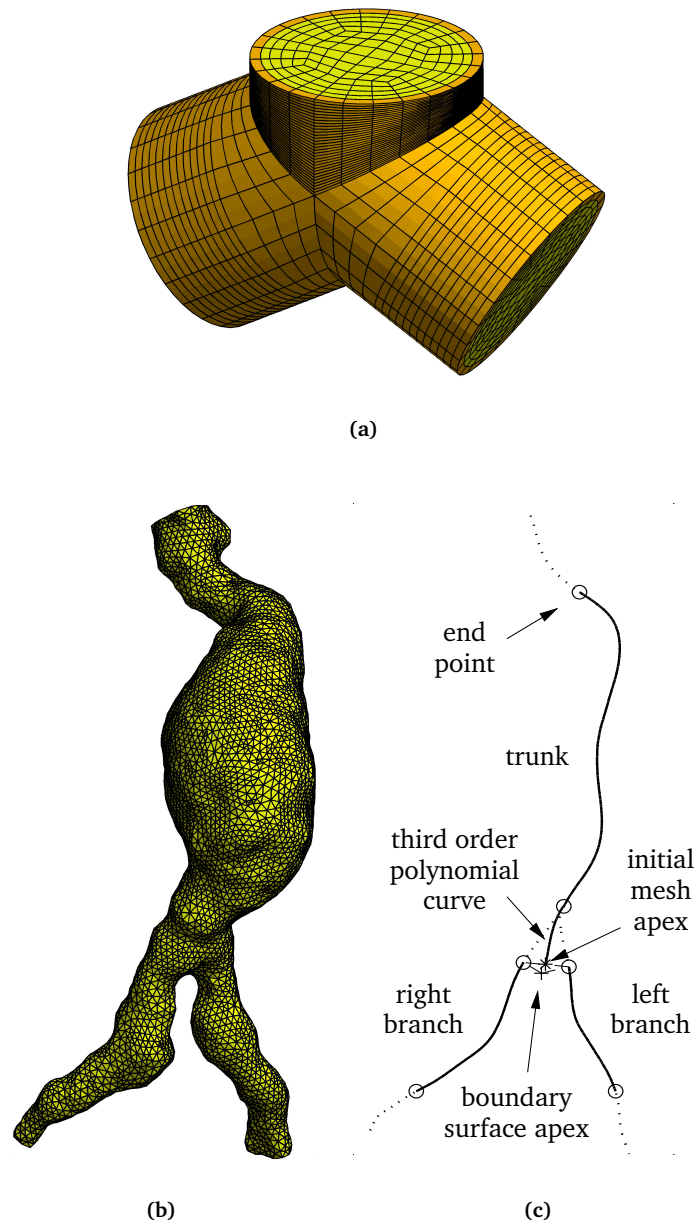


Figure 2.2: Input to the mesh generation procedure: standardised bifurcated mesh consisting of both fluid (light) and solid (dark) domains (a); boundary surface triangulation of the segmentation (b); original (dotted) and reconfigured (solid) centre-lines (c).

Next, based on the triangulated boundary surface, the initial fluid mesh is incrementally deformed to eventually fit the segmented AAA. First, for every point of the fluid-solid boundary of the mesh, the projection distance d to the triangulation is determined as described in Appendix A.3. Next, the transformation of the mesh into the patient-specific shape is determined by solving a linearly elastic deformation problem, where the inflow and outflow boundaries are constrained to in-plane motion. To each of the fluid-solid boundary points, a displacement is prescribed in a direction \mathbf{n}' that is determined by Laplacian smoothing of the local surface normal \mathbf{n} (see Figure A.2(e)). The smoothing procedure, necessary to prevent mesh warping, is again described by (2.1) to (2.3), where in (2.1) and (2.2), \mathbf{x} is substituted by \mathbf{n} . To obtain a high degree of smoothing, the procedure is repeated 50 times with $\lambda = 0.5$. After every step, \mathbf{n}' is normalized. The displacement δ of a point is based on d , where again Laplacian smoothing is applied between neighbouring points. This time, the smoothing procedure is only repeated 10 times. To promote smooth mesh deformation, the mesh is transformed in an incremental fashion, where in every increment, δ equals $d/2$. In addition, during a selected number of initial steps, δ is limited to d divided by the number of initial increments left:

$$\begin{aligned}\delta &= \frac{d}{h_i - h + 1} && \text{for } h < h_i, \\ \delta &= \frac{d}{2} && \text{for } h \geq h_i,\end{aligned}\tag{2.4}$$

with h the increment and h_i the number of initial increments. The transformation process is defined to converge after the increment when the mean variation of d over all boundary points has decreased below a criterion ε :

$$\bar{d}|_{h_c} - \bar{d}|_{h_c-1} \leq \varepsilon\tag{2.5}$$

with $\bar{d}|_h$ the mean projection distance at increment h and h_c the increment of convergence.

Next, the wall mesh is generated by transformation of the solid domain of the standardized mesh based on the determined shape of the fluid domain. First, for every node of the mesh, an associated node on the inner wall surface is found, based on the constant topology of the different layers of nodal points throughout the thickness of the wall. Next, the various nodal points are orientated in the direction of the normal to the inner wall surface, evaluated at the associated nodes. To prevent mesh warping, again Laplacian smoothing is applied to the surface normals. Further, the wall cross sections at the inflow and outflow boundaries of the lumen mesh are oriented in the planes associated with those boundaries. The relative transversal nodal point positions with respect to the inner wall surface are retained in the transformation. The total wall thickness is set to a characteristic value.

Finally, to correct for small element distortions that may occur in the transformation of the lumen and wall meshes, the positions of the edge and face mid-points with respect to the vertices of all elements are adjusted. Each of the edge mid-points is translated to the centre of a parabolic curve fitted through the edge end-points

and the mid-point itself. Next, each of the face mid-points is determined from the points along the face edges using Serendipity shape functions (Zienkiewicz and Taylor, 2000). These functions are also applied to finally determine the new positions of the element centroids.

2.2.3 Wall deformation and blood flow models

The stress and strain distributions in the AAA wall are computed by solving the equations of motion and continuity on the solid domain Ω_s of the AAA model. The inertial and gravitational forces acting on the wall are neglected because they are of a lesser order of magnitude than the wall forces associated with the intravascular pressure load. For an incompressible material with spatial coordinates \mathbf{x} , the equations then read

$$\begin{cases} \nabla \cdot \boldsymbol{\sigma} = \mathbf{0} \\ \det(\mathbf{F}) - 1 = 0 \end{cases} \quad \text{in } \Omega_s, \quad (2.6)$$

with $\boldsymbol{\sigma}$ the Cauchy stress tensor and $\mathbf{F} = (\nabla_0 \mathbf{x})^T$ the deformation gradient tensor with respect to the reference state. The AAA wall is considered a linearly elastic neo-Hookean material, the Cauchy stress tensor of which is defined by

$$\boldsymbol{\sigma} = -p\mathbf{I} + G(\mathbf{B} - \mathbf{I}), \quad (2.7)$$

with p the hydrostatic pressure, \mathbf{I} the unit tensor, G the shear modulus and $\mathbf{B} = \mathbf{F} \cdot \mathbf{F}^T$ the Finger tensor. With respect to the boundary conditions, at the cross sectional surfaces at the inflow and the two outflow locations, $\Gamma_{s,i}$, Γ_{s,o_1} and Γ_{s,o_2} , respectively, all displacements are constrained. At the fluid-solid boundary $\Gamma_{f,s}$, the normal stress is prescribed in terms of a given pressure load p , while the outer wall boundary $\Gamma_{s,w}$ is considered stress-free in normal direction:

$$\begin{cases} \mathbf{x} = \mathbf{x}_0 & \text{on } \Gamma_{s,i} \cup \Gamma_{s,o_1} \cup \Gamma_{s,o_2}, \\ (\boldsymbol{\sigma} \cdot \mathbf{n}) \cdot \mathbf{n} = -p & \text{on } \Gamma_{f,s}, \\ (\boldsymbol{\sigma} \cdot \mathbf{n}) \cdot \mathbf{t}_j = 0 & \\ \boldsymbol{\sigma} \cdot \mathbf{n} = \mathbf{0} & \text{on } \Gamma_{s,w}, \end{cases} \quad (2.8)$$

with \mathbf{n} the outward boundary normals and $\mathbf{t}_j|_{j=1,2}$ the tangential boundary vectors.

The blood velocity and wall shear stress distributions in the AAA are computed by solving the Navier-Stokes equations on the deforming fluid domain Ω_f of the AAA model based on the arbitrary Lagrangian–Eulerian (ALE) method (van de Vosse *et al.*, 2003). The gravitational forces acting on the blood are neglected, since the effects of geometrical factors independent of body posture are of primary interest. For an incompressible fluid with velocity \mathbf{v} and density ρ , the ALE formulation of the Navier-Stokes equations then reads:

$$\begin{cases} \rho \frac{\partial \mathbf{v}}{\partial t} + \rho(\mathbf{v} - \mathbf{w}) \cdot \nabla \mathbf{v} - \nabla \cdot \boldsymbol{\sigma} = \mathbf{0} \\ \nabla \cdot \mathbf{v} = 0 \end{cases} \quad \text{in } \Omega_f, \quad (2.9)$$

where t denotes time and with \mathbf{w} the velocity of the fluid domain. Blood is considered an inelastic generalised Newtonian fluid, the Cauchy stress tensor of which is defined by

$$\boldsymbol{\sigma} = -p\mathbf{I} + 2\eta\mathbf{D}, \quad (2.10)$$

with p the fluid pressure, η the viscosity and $\mathbf{D} = \frac{1}{2} [\nabla\mathbf{v} + (\nabla\mathbf{v})^T]$ the rate of deformation tensor. Shear-thinning behaviour is incorporated by making the viscosity dependent on the shear rate $\dot{\gamma}$ according to the Carreau-Yasuda model:

$$\frac{\eta - \eta_\infty}{\eta_0 - \eta_\infty} = [1 + (\lambda\dot{\gamma})^a]^{-\frac{n-1}{a}}, \quad (2.11)$$

with η_0 and η_∞ the viscosities at low and infinite shear rates, respectively, and λ , a and n parameters describing the transition between the two. The shear rate is defined as a function of the second invariant of the rate of deformation tensor:

$$\dot{\gamma} = \sqrt{2II_{\mathbf{D}}} = \sqrt{2\text{tr}(\mathbf{D}^2)}. \quad (2.12)$$

This approach to modelling the non-Newtonian behaviour of blood is discussed in Gijzen *et al.* (1999).

With respect to the boundary conditions, at the inflow boundary $\Gamma_{f,i}$, a plug velocity profile is prescribed in normal direction, at the outflow boundaries Γ_{f,o_1} and Γ_{f,o_2} , the fluid is considered stress-free and at the fluid-solid boundary, a no-slip condition is prescribed:

$$\begin{cases} (\mathbf{v} - \mathbf{w}) \cdot \mathbf{n} = -\frac{q}{A} \\ (\mathbf{v} - \mathbf{w}) \cdot \mathbf{t}_i = 0 \\ \boldsymbol{\sigma} \cdot \mathbf{n} = \mathbf{0} \\ \mathbf{v} - \mathbf{w} = \mathbf{0} \end{cases} \quad \begin{array}{l} \text{on } \Gamma_{f,i}, \\ \\ \text{on } \Gamma_{f,o_1} \cup \Gamma_{f,o_2}, \\ \text{on } \Gamma_{f,s}, \end{array} \quad (2.13)$$

with q a prescribed flow rate and A the area of the inflow boundary. The wall shear stress magnitude $|\boldsymbol{\tau}|$ at the fluid-solid boundary is determined by simple multiplication of the local shear rate with the viscosity:

$$|\boldsymbol{\tau}| = \eta(\dot{\gamma})\dot{\gamma}. \quad (2.14)$$

More detailed information on the applied equations can be found in van de Vosse *et al.* (2003).

2.2.4 Implementation and simulations

In order to provide a computed fluid domain velocity to the blood flow simulation, the wall deformation and blood flow problems are solved in a successive manner. First, the wall deformation problem is solved, giving the time-varying displacement field of the wall mesh. From the displacement field, the time-varying wall stress distribution

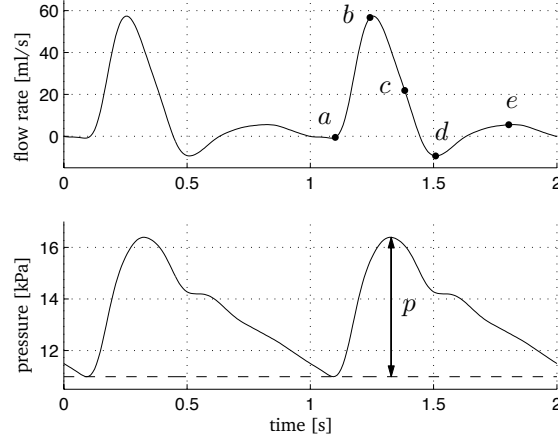


Figure 2.3: Prescribed blood flow rate and wall pressure load (after Olufsen *et al.*, 2000). The markings *a*, *b*, *c*, *d*, and *e* respectively denote end-diastole, peak-systole, late-systole, end-systole, and mid-diastole.

is determined using the wall constitutive behaviour. Next, the motion of the fluid mesh is computed by solving a linearly elastic deformation problem defined on the fluid domain, where the motion of the fluid-solid boundary surface is used as boundary condition. Finally, the blood flow problem is solved, giving the blood velocity and pressure fields with respect to the deforming fluid mesh. From the velocity field, the time-varying wall shear stress distribution is computed using the blood viscosity model. All sets of equations are linearised, discretised and solved using the SEPRAN finite element package (SEPRAN BV, The Hague, NL).

The boundary conditions imposed in the simulations are based on pressure and flow rate signals in the healthy aortic bifurcation as respectively simulated and measured by Olufsen *et al.* (2000). Both signals are scaled to obtain a time period of 1 s. The prescribed pressure load p in the wall deformation simulation equals the deviation from the minimum or end-diastolic value of the concerned pressure signal (see Figure 2.3). The flow rate q in the blood flow simulation is scaled to obtain a peak-systolic Reynolds number of 1000, based on the average inlet diameter and the viscosity at infinite shear rate (see Figure 2.3).

The wall and blood properties applied in the simulations are set in the order of magnitude of properties applied in literature. In the wall deformation simulation, the shear modulus of the wall material is set to 1.0 MPa, based on the elastic modulus of around 3 MPa applied by Di Martino *et al.* (2001). The wall thickness is set to 2.0 mm, based on measurements by Raghavan and Vorp (2000b) and Thubrikar *et al.* (2001a). In the blood flow simulation, the parameters of the Carreau-Yasuda viscosity model are determined by least-squares approximation of blood viscosity measurements by Thurston (1979), yielding $\eta_0 = 52$ mPa s, $\eta_\infty = 4.8$ mPa s, $a = 0.41$, $n = 0.19$ and $\lambda = 0.44$ s. The density is set to 1080 kg/m³ (Gijssen *et al.*, 1999).

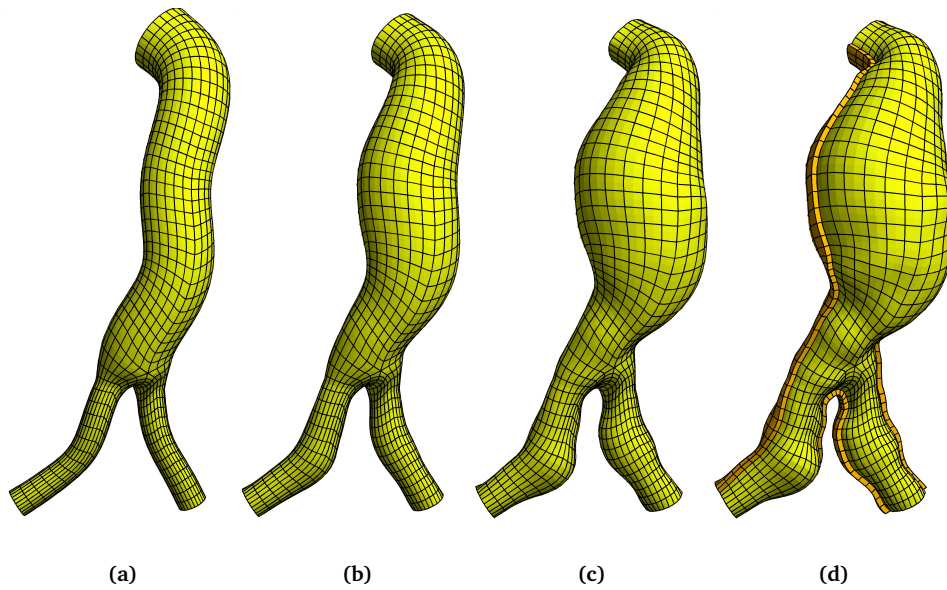


Figure 2.4: Incremental transformation of the initial fluid mesh: initial situation (a); after 4 increments (b); after 8 increments (c); after 16 increments, with wall mesh (d).

The simulations are performed on a single 900 MHz Itanium II processor of a SGI Altix system. To obtain a time periodic solution in the blood flow simulation, four consecutive periods are simulated.

2.3 Results

The incremental transformation of the initial lumen mesh results in a patient-specific mesh that closely resembles the triangulated boundary surface of the segmented AAA (see Figure 2.4). Based on the desired minimum variation of the mean distance of the lumen mesh boundary points towards the triangulated boundary surface of $5 \cdot 10^{-3}$ mm and 8 initial steps, the transformation process converges in 16 increments (see Figure 2.5). During the transformation, at the level of the bulge, the initial mesh is inflated to a great extent, while in the inflow region, the mesh is constricted. In the iliac arteries, the degree of inflation varies with the axial position. Both at the bifurcation and in other mesh parts, the inflation process results in a regular element distribution. The transformation of the solid part of the standardised mesh yields a wall geometry that closely surrounds the shape of the lumen (see Figure 2.4(d)).

The wall stress distribution in the AAA is characterised by a global increase of stress around the bulge combined with more localised areas of increased and de-

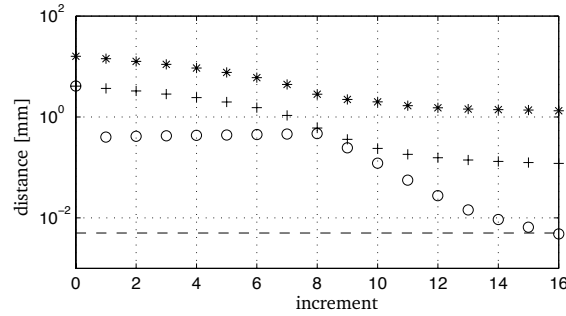


Figure 2.5: Convergence of the mesh transformation process in terms of maximum (*), mean (+) and variation of the mean (o) projection distance d of the fluid-solid boundary points to the surface triangulation. The dotted line denotes the desired minimum variation of the mean ($\varepsilon = 5 \cdot 10^{-3}$ mm).

creased stress distributed over the aneurysm (see Figure 2.6). The highest stresses occur at these localised areas. Furthermore, high stresses occur at the apex of the bifurcation at the inner wall. Although the wall stress distribution on the inner wall differs from that on the outer wall, the two are closely related. Either aside or opposite to stress concentrations on one side of the wall, on the other side similar or complementary concentrations occur.

The blood velocity distribution in the AAA is characterised by the consecutive formation and diminishing of 3-D vortices (see Figure 2.7). At end-diastole, there are few remains of the vortices formed in the previous flow cycle. In the iliac arteries, there is reversed flow near the wall. At peak systole, all remaining vortices have been washed out and except for a small area of flow separation at the inner bend of the inflow region, there is an attached flow pattern. During systolic deceleration, the area of flow separation has grown into a large 3-D vortex migrating from the wall. In the bifurcation region and at local dilatations in the iliac arteries there is vortex formation as well. At end-systole, the vortex in the inflow region has promoted a complicated flow pattern that balances the reversed flow at the inflow boundary. In the iliac arteries, the vortices have migrated towards the main stream and there are large areas of reversed flow near the wall. At mid-diastole, the vortices present at end-systole have translated and/or diminished and areas of reversed flow are not present.

The WSS distribution in the AAA comprises a time-varying pattern of both regions of high and low WSS that are determined by both the local diameter and locally occurring vortices (see Figure 2.8). At all instants, the WSS in the bulge is very low compared to the WSS in the inflow region and in the iliac arteries. At end-diastole, there are slight gradients between the central and the proximal and distal sides of the bulge. In the iliac arteries, the WSS is mainly determined by local constrictions and dilatations. At peak-systole, the bulge WSS has increased. The gradients over the bulge have increased as well, both at the proximal and the distal side. In the

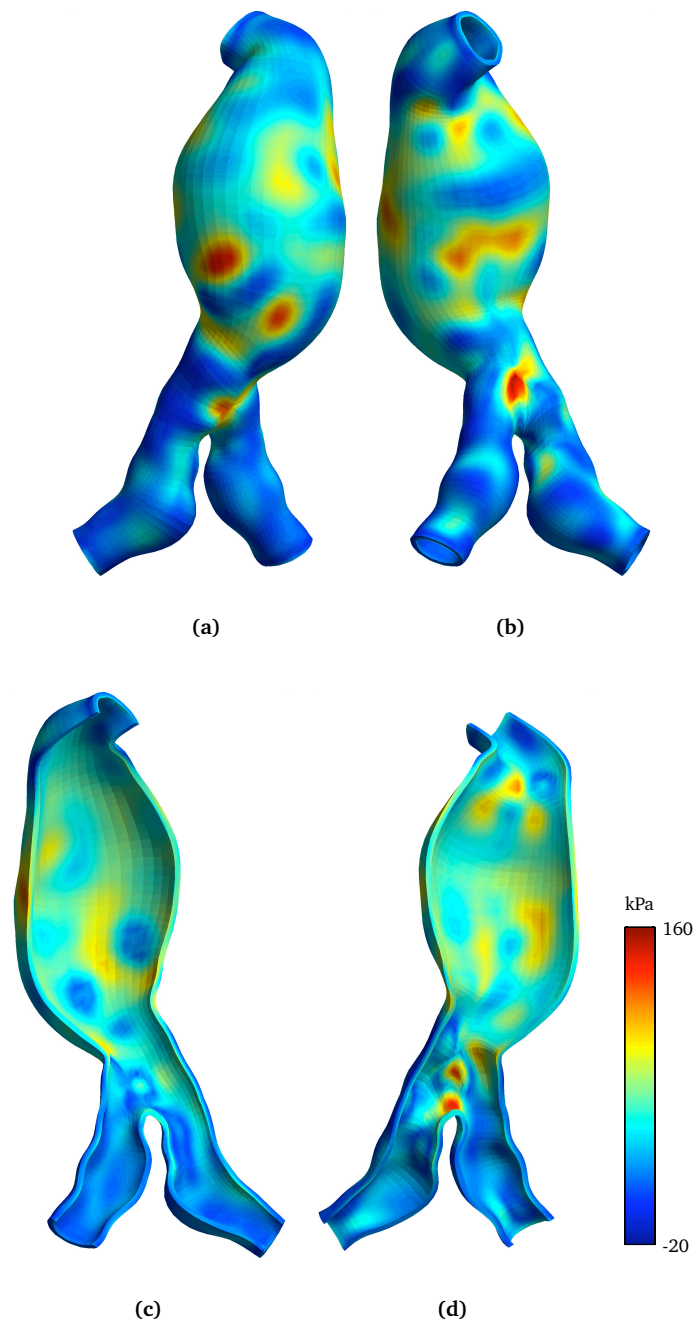


Figure 2.6: Maximal principal wall stress at peak systole: anterior/external (a); posterior/external (b); posterior/internal (c); anterior/internal (d).

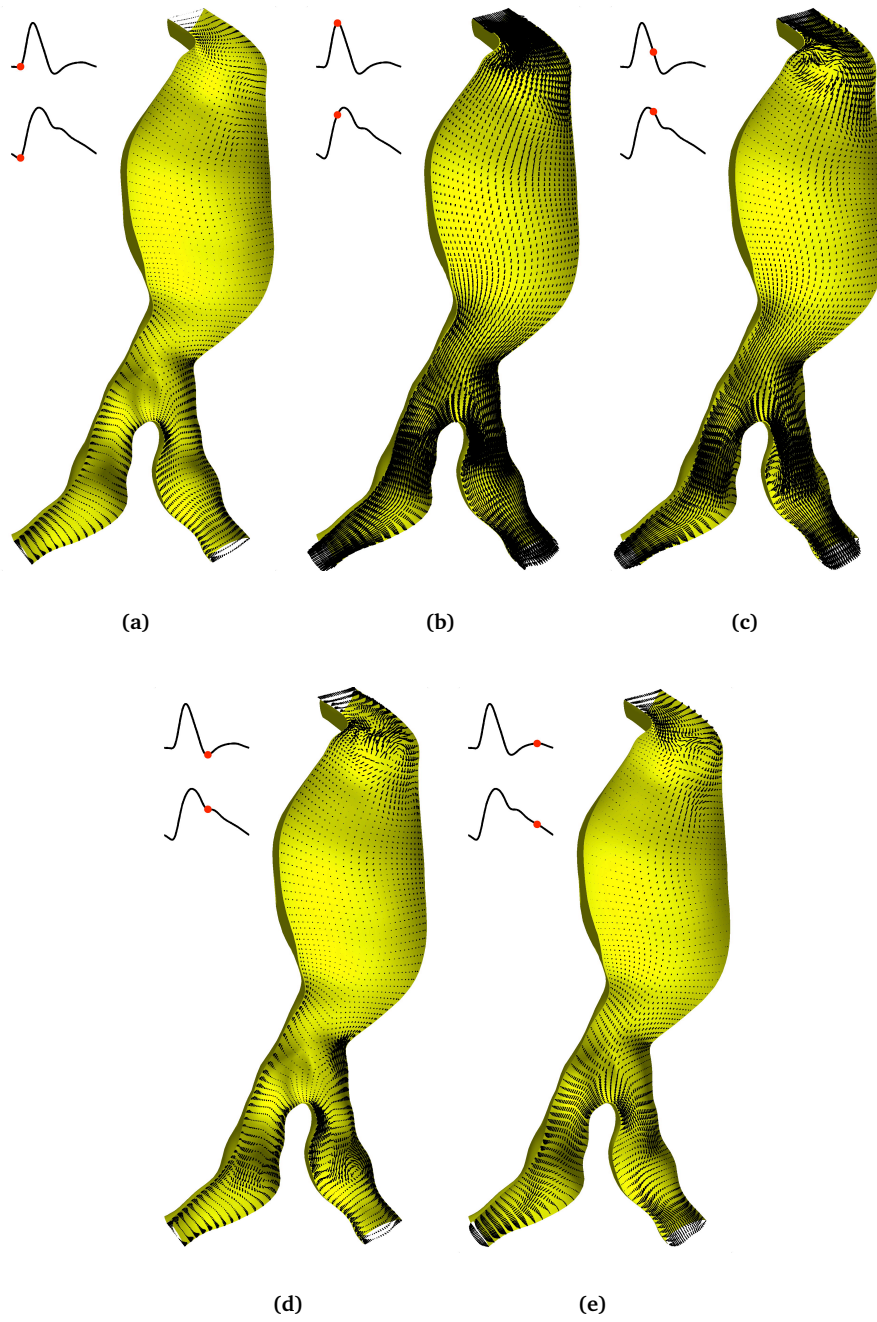


Figure 2.7: Blood velocity distribution in the deforming geometry at end-diastole (a), peak-systole (b), late-systole (c), end-systole (d), and mid-diastole (e).

iliac arteries, the WSS is still mainly determined by the diameter. During systolic deceleration, both the bulge WSS and the distal bulge gradient have decreased. At the proximal side, a local area of high WSS has migrated in distal direction. At the outer bend of the inflow region, the WSS has decreased. In the iliac arteries, the WSS has become less dependent on the diameter. At end-systole, the WSS has rather evened out than decreased. Yet, the proximal bulge gradient is still present. Further, in the iliac arteries, the WSS is not primarily determined by the diameter. At mid-diastole, the WSS and WSS gradients have diminished to a great extent. The effect on the WSS of the iliac artery diameter has once again become dominant.

The computational time needed for the simulations approximated 6 days per simulated period. It is expected that this time can be reduced by optimisation of the applied computational algorithms, but this was not pursued in the current study.

2.4 Discussion

In order to facilitate the incorporation of fluid-structure interaction (FSI) in the assessment of AAA wall stress, a method for generating patient-specific hexahedral finite element meshes of the AAA lumen and wall has been presented. In this method, first, the fluid domain of a standardised bifurcated fluid-solid mesh is transformed into an initial shape that is oriented along the centrelines of a segmented AAA. Next, the initial mesh is incrementally transformed to eventually fit a boundary surface triangulation of the segmented AAA. Finally, the wall mesh is generated by transformation of the solid domain of the standardised mesh based on the determined shape of the lumen mesh. The applicability of the meshes has been illustrated by simulations of the wall stress, blood velocity distribution and WSS in a characteristic AAA.

Although the considered method may take more effort than direct meshing by means of Delaunay methods, it is expected to limit the computational cost of rupture risk assessment models incorporating FSI. First, the application of hexahedral elements provides for more accurate descriptions of the computed quantities than the use of tetrahedral elements (van de Vosse *et al.*, 2003). Second, the application of standardised meshes allows for pre-defined element distributions, which can implicitly limit the amount of elements needed to describe certain geometries and computed quantities. Since patient-specific blood-wall interaction simulations are associated with considerable amounts of computational time, increased efficiency of such simulations could be a decisive factor in their clinical impact.

The main assumption in the method of mesh generation as it has been presented is that the segmented aneurysm does not contain thrombus. Irrespective of the morphology of the structures surrounding the lumen, the wall mesh is placed directly against the fluid mesh. To incorporate a thrombus model, the applied surface triangulation should represent the inner wall boundary rather than the outer lumen boundary. A mural thrombus could then possibly be modelled either by incorporating a standardised thrombus model in the initial mesh and deforming its inner boundary to fit the outer boundary of the lumen or by incorporating the thrombus in the wall model and spatially varying their combined thickness and mechanical properties. A

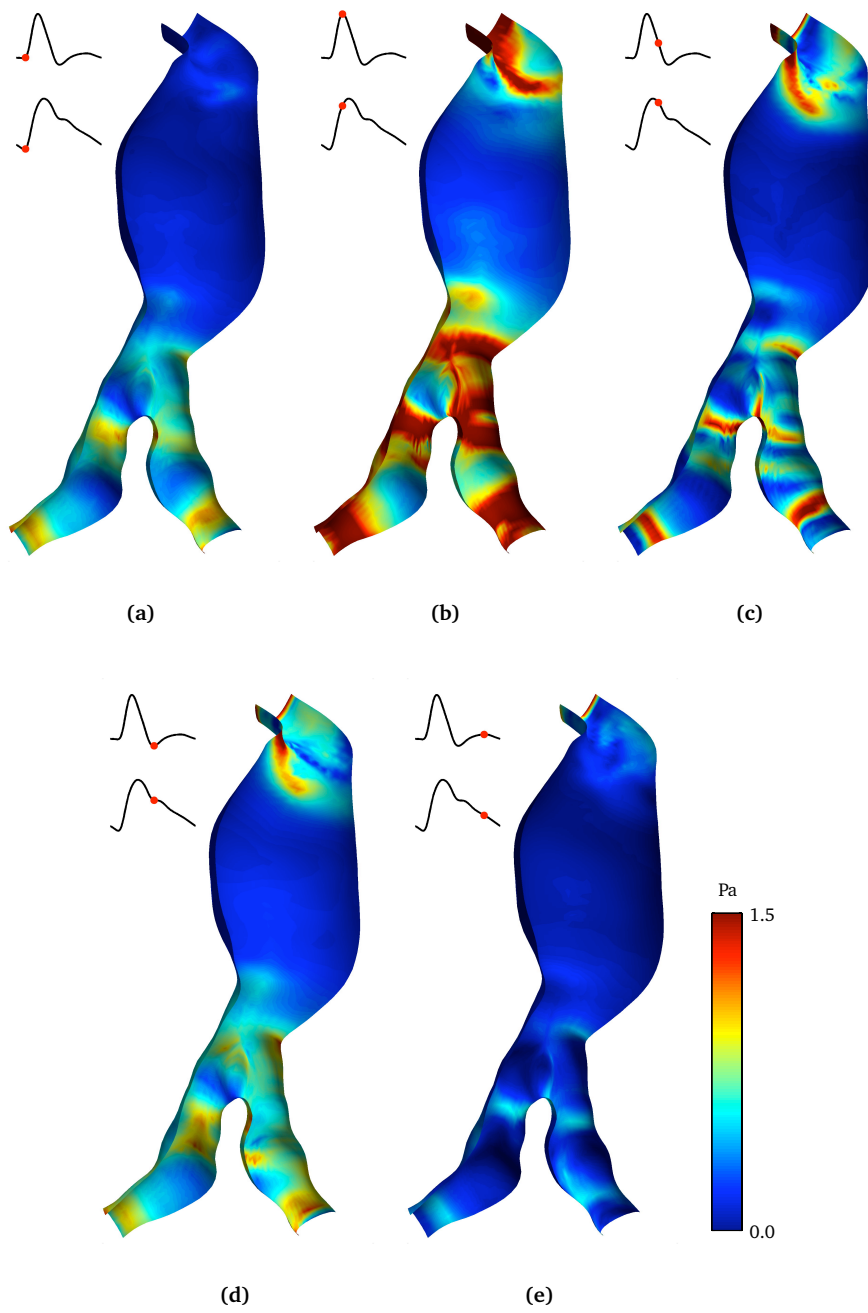


Figure 2.8: Wall shear stress in the deforming geometry at end-diastole (a), peak-systole (b), late-systole (c), end-systole (d), and mid-diastole (e).

more distributed thrombus could only be modelled using the latter approach.

For the AAA considered in this study, the hexahedral mesh obtained with the presented method closely represents the characteristics of the boundary surface triangulation of the segmentation. To what extent the mesh matches the vascular anatomy is dependent on both the accuracy of the segmentation and the accuracy of the mesh transformation procedure. In Figure 2.5 it is shown that the mean distance of the transformed mesh boundary points to the surface triangulation is in the order of 0.1 mm. Since this is more accurate than the possible error made during imaging and segmentation, which is in the order of 1 mm, the accuracy of the surface triangulation is the main determining factor.

In the blood-wall interaction model, it is assumed that the combined behaviour can be solved using a decoupled approach. This is motivated by the fact that in general, local pressures in the arterial system are mainly determined by the arterial pressure wave. With U a characteristic blood flow velocity, flow-induced pressure variations are in the order ρU^2 , which is negligible compared to the pressure wave magnitude. Based on an inflow boundary area of 220 mm² and a peak flow rate of 57 ml/s, in the current study, the peak inflow velocity is 0.27 m/s. The flow-induced pressure variations are therefore in the order of 0.1 kPa, while the pressure load is in the order of 10 kPa. Therefore the decoupled approach is permitted.

Other assumptions that can have an impact on the results are concerned by the choice of boundary conditions. First, the applied flow rate and pressure load signals are based on a young healthy male (Olufsen *et al.*, 2000). It cannot be expected that these signals represent the specific situations in older patients having cardiovascular disease affecting the arterial haemodynamics such as hypertension and atherosclerosis (Lakatta, 2002). Second, at the outflow boundaries of the lumen, the fluid is assumed to be stress-free. In reality, the outflow conditions are determined by the impedance of the distal parts of the arterial tree. To overcome these problems, a one-dimensional model of blood flow in arteries could be adopted, describing the flow and pressure waves in the arterial system (see for instance Formaggia *et al.*, 2003). This could provide physiologic flow and pressure boundary conditions that are in tune to one another. Finally, MRA-based 3-D velocity measurements in patients could provide a more specific inflow profile. Since the flow pattern close to the inflow boundary is always affected by the profile that is imposed, the adverse effects of non-physiologic profiles may be considerable in AAA geometries with shorter neck lengths. For the simulated case however, a measured profile was not available. A plug flow was applied instead to simulate inertia-dominated flow.

Although the situation modelled in the current paper is similar to the situation modelled by Di Martino *et al.* (2001), the results are difficult to compare. In the latter paper, no vector fields of the velocity distribution were presented. Furthermore, the applied geometry varied considerably from the geometry applied in the current paper. However, it should be noted that in both studies, the wall displacements were small. The extent to which the relatively larger blood flux associated with these displacements has an impact on the flow characteristics in patient-specific AAAs in general should be subject to further investigation. In the current situation however, the pulse wave velocity, which is in the order of $\sqrt{hE/(\rho R)}$, with h a characteristic

wall thickness and R a characteristic vessel radius, is about 11 m/s, so the wave length is about 11 m. Since this is rather high in relation to the axial length of the model, a comparison with rigid models of AAA flow may be appropriate.

The current study confirms the characteristic velocity patterns and accompanying WSS gradients observed in rigid AAA models. In resting conditions, for asymmetric models, the vortices formed at the proximal side of the bulge during systolic deceleration slowly expand and migrate (Egelhoff *et al.*, 1999; Finol *et al.*, 2003). In the current study, although the Reynolds number applied is in the order of the Reynolds number in resting conditions, vortex formation and translation is less prominent than in the above studies. This may be due to the fact that in the current study, an angulation is present at the neck of the aneurysm, while the above rigid models were straight. Because of the angulation, the vortex formed at the distal end of the neck inner bend is driven into the opposite wall, where it is diminished. The typical WSS gradients promoting thrombus formation (Bluestein *et al.*, 1996) are still present. Yet, due to the applied Carreau-Yasuda model, it is expected that the absolute WSS values better approximate the in-vivo values. Further, it should be noted that the WSS pattern near the inflow boundary is affected by the imposed inflow profile.

The wall stress simulations confirm previous studies in the sense that the AAA wall stress distribution is complex and to a great extent influenced by local wall curvature. Yet, it should be noted that the curvature-induced stress concentrations in the current study mainly occur at locations at which calcifications are present in the CTA image. The calcifications can be noted in Figure 2.1 by the white areas. Due to the high intensity of the calcifications compared to that of the lumen, dents are generated in the segmented lumen boundary surface and therefore in the wall model. This could be solved by more accurate segmentation of the lumen for instance by removal of the calcifications using local subtraction (van Straten *et al.*, 2003). Further, since the wall curvature in general is dependent on the accuracy of the segmented boundary surface, it should be studied to what extent the computed wall stress is affected by the protocol and the modality that were applied to generate the original image.

The wall simulations may provide good measures of geometry-based wall stress variations to relate to AAA rupture risk. For a more accurate correlation, probably a more dedicated material model will be necessary, such as the one proposed by Raghavan and Vorp (2000a). Also, the wall thickness should be varied to distinguish between healthy and diseased tissue (Raghavan and Vorp, 2000b) and between the aorta and the iliac arteries. Further, it should be considered whether the maximum principal stress as obtained in the current study provides a better criterion for correlation than the Von Mises stress obtained in previous studies (Raghavan and Vorp, 2000b; Wang *et al.*, 2002; Venkatasubramaniam *et al.*, 2004). Although Fillinger *et al.* (2002) report that the results of the two criteria are similar, the maximum principle stress criterion may become more important when considering the anisotropic behaviour of the aneurysm wall (Thubrikar *et al.*, 2001a).

If the developed model is applied in rupture risk assessment based on the wall stress to strength ratio rather than peak stress only, it should be considered whether the amplitude-based pressure load yields a better prediction than the peak-systolic pressure load applied in previous studies (Raghavan and Vorp, 2000b; Thubrikar

et al., 2001b; Fillinger *et al.*, 2002; Venkatasubramaniam *et al.*, 2004). Although currently the computed wall stress will be lower than physiologic for lack of an initial stress model, when applying a material model suitable for large displacements, the results obtained with a peak-systolic load may be less realistic. An exact simulation of AAA wall rupture is however further complicated by the need for knowledge on the patient-specific morphology, material properties, and boundary conditions. Also then, on the outer wall surface, an external stress and/or kinematic constrictions may have to be provided to simulate the presence of external tissues like the spinal column.

2.5 Conclusion

In conclusion, the method of mesh generation that has been presented provides a flexible, semi-automated approach for generating patient-specific hexahedral meshes of the AAA lumen and wall with pre-defined element distributions. The combined fluid-solid mesh allows for simulations of AAA blood dynamics and AAA wall mechanics and the interaction between the two. The mechanical quantities computed in these simulations need to be validated in a clinical setting, after which they could be included in clinical trials in search of risk factors for AAA rupture. In addition, the presented method provides a basis for the development of models for studying the role of blood-wall interaction in processes associated with AAA formation such as wall adaptation and thrombus formation.

Chapter 3

Computational modelling of fluid-structure interaction in abdominal aortic aneurysms: initial wall stress effects

3.1 Introduction

To better identify patients at high risk for rupture of an abdominal aortic aneurysm (AAA), in several studies, patient-specific computational models have been developed to provide a wall stress based indication of rupture risk. Traditionally, in these models, the wall stress is determined by loading a patient-specific wall model with a characteristic or measured systolic pressure load (Raghavan and Vorp, 2000b; Thubrikar *et al.*, 2001b; Fillinger *et al.*, 2002; Wang *et al.*, 2002; Venkatasubramanian *et al.*, 2004). For AAAs under observation, the peak wall stress determined using such models seems a better predictor of rupture than the maximal transverse diameter currently used in clinical practise (Fillinger *et al.*, 2003). In this relation, the use of a patient-specific pressure load seems of critical importance (Truijers *et al.*, 2007).

To both improve wall stress based indications of rupture risk and better understand AAA formation and development, in other studies similar models have been developed including the effects of fluid-structure interaction (FSI). Such models have been applied to study for instance the effects of fluid dynamic loading and wall distensibility, and additional flow features such as the wall shear stress (WSS) (Di Martino *et al.*, 2001; Wolters *et al.*, 2005; Leung *et al.*, 2006; Papaharilaou *et al.*, 2007; Scotti and Finol, 2007). Additional effort has been put into the development of methods for incorporating the initial wall stress, meaning the wall stress already present in the AAA wall at diastolic pressure, and to study the effects thereof on computed model results (Raghavan *et al.*, 2006; Lu *et al.*, 2007a,b; De Putter *et al.*, 2007). Incorpora-

tion of the initial stress has been found to affect the peak wall stress by up to 10 to 20 percent, depending on the compliance of the AAA wall material (Lu *et al.*, 2007b).

Although the results of AAA solid stress models have been found to be affected by the presence of initial wall stress, in previous FSI studies of AAA, the initial stress was not incorporated. In the case that the wall pressure load is represented by the absolute peak-systolic pressure as in Leung *et al.* (2006), Papaharilaou *et al.* (2007), and Scotti and Finol (2007), neglect of the stress already present at diastolic pressure will lead to an overestimation of the wall displacement and wall strain. Based on differences in computed model results of hemodynamic simulations using rigid and distensible geometries (Perktold and Rappitsch, 1995; Torii *et al.*, 2007), an overestimation of the displacement is expected to yield a significant underestimation of the WSS. By application of only the systolic pressure increase relative to the diastolic pressure as in Di Martino *et al.* (2001) and Wolters *et al.* (2005), the problem is only partly solved. Although the displacement field and WSS in that case presumably will be better estimated, by computing only the wall stress increase relative to the diastolic state, the peak wall stress will not be captured correctly. Further, in the latter approach, a material model of the AAA wall in the pressurised state is required. Without knowledge of the diastolic state of strain, more generalised non-linear AAA wall material models such as that by Raghavan and Vorp (2000a) are not applicable.

To investigate the importance of incorporating initial wall stress in FSI simulations of AAA, in this study, an FSI simulation of an idealised AAA is performed both in the presence and in the absence of initial stress. The two cases are compared by considering the differences in wall deformation, the wall stress distribution, the velocity distribution, and WSS. Additionally, by varying the wall thickness and considering a rigid wall case, the effects of the wall distensibility are studied. Based on the results, it is determined to what extent the initial stress affects the differences between rigid and distensible wall model results.

3.2 Methods

3.2.1 Geometrical model

The idealised AAA is modelled as a sinusoidally shaped dilatation of a straight tube. The geometrical model consists of both a fluid domain and a solid domain (see Figure 3.1). The model dimensions are chosen in the physiologic range, with inflow and maximal diameters of respectively 20 mm and 50 mm, and an aneurysm length of 80 mm. The total tube length is 160 mm. Depending on the simulation, the wall thickness is varied between 1.0 and 2.0 mm.

3.2.2 Wall deformation and blood flow models

The wall deformation is computed by solving the equations of motion and continuity defined on the solid domain. In the absence of body forces, for an incompressible

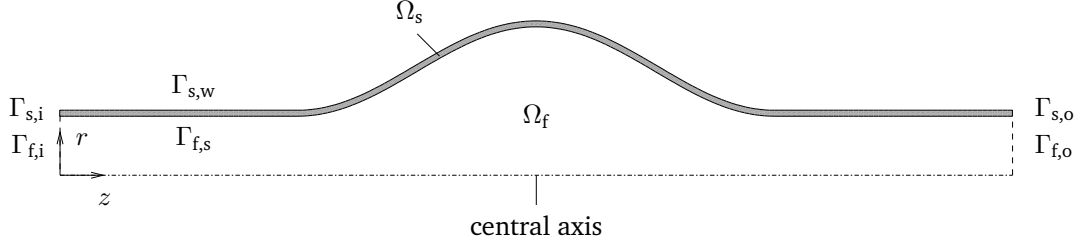


Figure 3.1: Geometry of the idealised AAA model. The fluid domain Ω_f is enclosed by the inlet boundary $\Gamma_{f,i}$, the outlet boundary $\Gamma_{f,o}$, and the fluid-solid boundary $\Gamma_{f,s}$. The solid domain Ω_s is enclosed by the boundaries $\Gamma_{s,i}$, $\Gamma_{s,o}$, $\Gamma_{f,s}$, and the outer wall boundary $\Gamma_{s,w}$.

material with spatial coordinates \boldsymbol{x} , these equations read

$$\begin{cases} \nabla \cdot \boldsymbol{\sigma} = \mathbf{0} \\ \det(\boldsymbol{F}) - 1 = 0 \end{cases} \quad \text{in } \Omega_s, \quad (3.1)$$

with $\boldsymbol{\sigma}$ the Cauchy stress tensor and $\boldsymbol{F} = (\nabla_0 \boldsymbol{x})^T$ the deformation gradient tensor with respect to the reference state. The constitutive behaviour is described using the material law proposed by Raghavan and Vorp (2000a), giving

$$\boldsymbol{\sigma} = -p\boldsymbol{I} + (2\alpha + 4\beta(I_B - 3))(\boldsymbol{B} - \boldsymbol{I}), \quad \boldsymbol{B} = \boldsymbol{F} \cdot \boldsymbol{F}^T, \quad (3.2)$$

with p the hydrostatic pressure, \boldsymbol{I} the unit tensor, \boldsymbol{B} the Finger tensor, I_B the first invariant of \boldsymbol{B} , and α and β model parameters indicative of the mechanical properties of the AAA wall. At the inlet and outlet boundaries, all displacements are constrained. At the fluid-solid boundary, the normal stress is prescribed in terms of a given pressure load p . The outer wall boundary in normal direction is considered stress-free:

$$\begin{cases} \boldsymbol{x} = \boldsymbol{x}_0 & \text{on } \Gamma_{s,i} \cup \Gamma_{s,o}, \\ (\boldsymbol{\sigma} \cdot \boldsymbol{n}) \cdot \boldsymbol{n} = -p & \text{on } \Gamma_{f,s}, \\ (\boldsymbol{\sigma} \cdot \boldsymbol{n}) \cdot \boldsymbol{t}_j = 0 & \text{on } \Gamma_{f,s}, \\ \boldsymbol{\sigma} \cdot \boldsymbol{n} = \mathbf{0} & \text{on } \Gamma_{s,w}, \end{cases} \quad (3.3)$$

with \boldsymbol{n} the boundary outward normal and $\boldsymbol{t}_j|_{j=1,2}$ the boundary tangential vectors.

The blood velocity and WSS distributions are determined by solving the Navier-Stokes equations defined on the fluid domain. In the absence of body forces, for an incompressible fluid with velocity \boldsymbol{v} and density ρ , the arbitrary Lagrangian-Eulerian (ALE) formulation of these equations reads

$$\begin{cases} \rho \frac{\partial \boldsymbol{v}}{\partial t} + \rho(\boldsymbol{v} - \boldsymbol{w}) \cdot \nabla \boldsymbol{v} - \nabla \cdot \boldsymbol{\sigma} = \mathbf{0} \\ \nabla \cdot \boldsymbol{v} = 0 \end{cases} \quad \text{in } \Omega_f, \quad (3.4)$$

where t denotes time and with \mathbf{w} the velocity of the fluid domain. The constitutive behaviour of the fluid is described using an inelastic Newtonian model:

$$\boldsymbol{\sigma} = -p\mathbf{I} + 2\eta\mathbf{D}, \quad \mathbf{D} = \frac{1}{2}[\nabla\mathbf{v} + (\nabla\mathbf{v})^T], \quad (3.5)$$

with p the fluid pressure, η the viscosity, and \mathbf{D} the rate of deformation tensor. Shear-thinning behaviour is incorporated by means of a shear rate dependent viscosity according to the Carreau-Yasuda model, with the shear rate defined as a function of the second invariant of the rate of deformation tensor:

$$\frac{\eta - \eta_\infty}{\eta_0 - \eta_\infty} = [1 + (\lambda\dot{\gamma})^a]^{-\frac{n-1}{a}}, \quad \dot{\gamma} = \sqrt{2II_{\mathbf{D}}} = \sqrt{2\text{tr}(\mathbf{D}^2)}, \quad (3.6)$$

with η_0 and η_∞ the viscosities at low and infinite shear rates, respectively, and λ , a and n parameters describing the transition between the two. This approach to modelling the non-Newtonian behaviour of blood is discussed in Gijssen *et al.* (1999). Further, the wall shear stress magnitude $|\boldsymbol{\tau}|$ is determined by multiplication of the shear rate with the viscosity:

$$|\boldsymbol{\tau}| = \eta(\dot{\gamma})\dot{\gamma}. \quad (3.7)$$

At the inlet boundary, a time-varying velocity profile $v_z(r, t)$ is prescribed based on a given flow rate as a function of time. At the outflow boundary, the fluid is considered stress-free, and at the fluid-solid boundary, a no-slip condition is prescribed:

$$\begin{cases} (\mathbf{v} - \mathbf{w}) \cdot \mathbf{n} = v_z(r, t) & \text{on } \Gamma_{f,i}, \\ (\mathbf{v} - \mathbf{w}) \cdot \mathbf{t}_i = 0 & \\ \boldsymbol{\sigma} \cdot \mathbf{n} = \mathbf{0} & \text{on } \Gamma_{f,o}, \\ \mathbf{v} - \mathbf{w} = \mathbf{0} & \text{on } \Gamma_{f,s}, \end{cases} \quad (3.8)$$

with r the radial coordinate.

3.2.3 Initial wall stress model

The initial wall stress is determined using the backward incremental approach by De Putter *et al.* (2007). In this method, for a domain Ω subject to a certain pressure load, the initial stress is defined by the transformation of an unloaded domain Ω_0 into Ω combined with a constitutive model. The domain Ω_0 is determined in an incremental procedure, where the initial estimate equals Ω . During the procedure, the pressure load on Ω is incrementally increased from zero to the pressure load given. At each increment, the transformation \mathbf{F}_Δ describing the deformation of Ω corresponding to the load step is computed as in an updated Lagrange method used in regular solid mechanics problems. Unlike in regular problems, however, \mathbf{F}_Δ is interpreted as contributing to the transformation of Ω_0 into Ω , rather than to the deformation of Ω itself into Ω_Δ . As a result, by application of the inverse transformation \mathbf{F}_Δ^{-1} to Ω , a new estimate of Ω_0 can be determined after the first increment. After several increments, the estimate $\hat{\Omega}_0$ is related to Ω through the transformation

$$\hat{\mathbf{F}} = \mathbf{F}_\Delta^{-1}\hat{\mathbf{F}}_n, \quad (3.9)$$

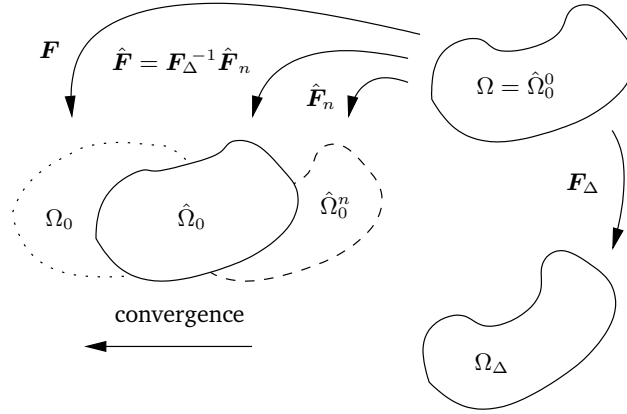


Figure 3.2: Schematic representation of the backward incremental approach to determine the initial wall stress.

where \hat{F}_n describes the transformation of Ω into the last known estimate of the unloaded domain $\hat{\Omega}_0^n$ (see Figure 3.2). Due to the fact that the deformation problem is defined on Ω rather than $\hat{\Omega}_0$, the latter is not in equilibrium with the imposed load. The procedure can be made to provide a domain Ω_0 that is stress-free, however, by application of a flattening load curve (De Putter *et al.*, 2007).

3.2.4 Implementation and simulations

The FSI simulation is based on a decoupled approach. During initialisation, either the wall deformation problem is solved to provide the initial wall coordinates in the absence of initial stress, or the initial wall stress is computed using the backward incremental approach. Next, every time step, the wall deformation problem is solved to give the wall displacement field. Next, the fluid mesh is deformed in accordance with the wall displacement, and the fluid mesh deformation is computed by solving a linearly elastic deformation problem. Based on the calculated mesh motion, the fluid mesh velocity is determined. Finally, the blood flow problem is solved to give the blood velocity and pressure distributions on the deforming fluid domain. Based on the computed velocity distribution and the constitutive model for the fluid, the WSS distribution is determined. The wall stress distribution is determined based on the wall displacement field and the constitutive model for the solid. All sets of equations are linearised, discretised and solved using the SEPRAN finite element package (SEPRAN BV, The Hague, NL).

The boundary conditions are based on pressure and flow rate signals in the healthy aorta from Olufsen *et al.* (2000) (see Figure 3.3). The wall pressure load p in the wall deformation problem is directly based on the given pressure signal. The pressure used for initialisation of the wall deformation problem and computation of the initial wall stress is the pressure signal value at 0 s. From the given flow rate signal, the velocity profile $v_z(r, t)$ in the blood flow problem is determined based on the Womersley

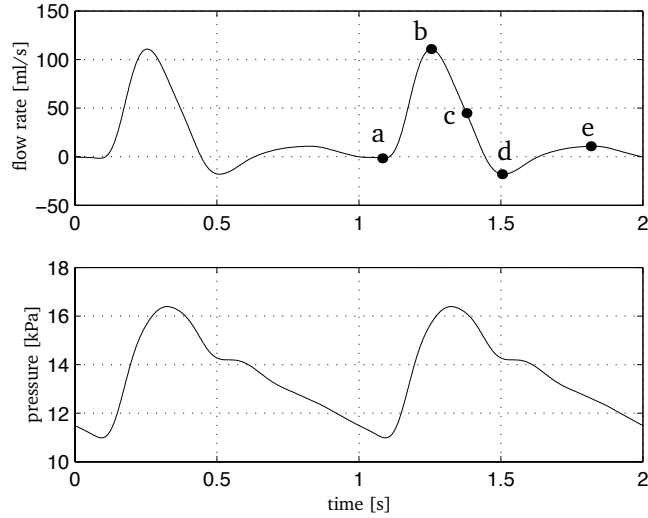


Figure 3.3: Prescribed blood flow rate and wall pressure load (after Olufsen *et al.*, 2000). The markings respectively denote end-diastole (a), peak-systole (b), late-systole (c), end-systole (d), and mid-diastole (e).

solution for fully developed pulsatile flow (Milnor, 1989).

The different results are obtained using distensible wall models of 1.0, 1.5, and 2.0 mm thickness. For comparison purposes, additional results are obtained using a rigid wall model. Further, to obtain a time periodic solution in the blood flow simulation, four periods are simulated. The wall material properties are based on Raghavan and Vorp (2000a), with $\alpha = 17.4 \text{ N/cm}^2$ and $\beta = 188 \text{ N/cm}^2$. In the blood flow simulation, the parameters of the Carreau-Yasuda viscosity model are determined by least-squares approximation of blood viscosity measurements by Thurston (1979), yielding $\eta_0 = 52 \text{ mPa s}$, $\eta_\infty = 4.8 \text{ mPa s}$, $a = 0.41$, $n = 0.19$, and $\lambda = 0.44 \text{ s}$. With the density set to 1080 kg/m^3 , the peak-systolic Reynolds number based on the viscosity at infinite shear rate is around 1600.

3.3 Results

In the presence of initial wall stress, the wall deformation is decreased dramatically compared to when the wall initially is considered stress free (see Figure 3.4). From the vessel radius at peak systolic pressure it can be gathered that in the latter case, the aneurysm is inflated by in the order of 10 percent. In the first case, the aneurysm largely retains its original shape (see Figure 3.4(a)). From the circumferential strain it can be gathered that the largest deformations resulting from the pressurisation occur at the sides of the bulge proximal and distal to the centre. Further, in the absence of initial stress, the wall deformation is clearly dependent on the wall thickness. In the

presence of initial stress, this dependence is less distinct (see Figure 3.4(b)).

With respect to the wall stress distribution, incorporation of the initial stress yields a redistribution in axial direction, while the overall stress level is decreased (see Figure 3.5). In all cases, a local maximal stress value occurs at the centre of the bulge, while the absolute maximal stress values occur at the sides of the bulge. By incorporation of the initial stress, the difference between the local and absolute maximal values is decreased, and the local maximum becomes more apparent, giving a more oscillatory profile. All changes are more pronounced for thinner walls.

The main effect of incorporating the initial stress on the blood velocity distribution is an increased recirculation, discernable from the increased intensity of the vortices present at various stages of the flow cycle (see Figures 3.6 and 3.7). Both in the absence and presence of initial stress, at end-diastole, a vortex remaining from the previous flow cycle is present at the distal side of the aneurysm. At peak-systole, this vortex has been washed out and the velocity distribution is characterised by an attached pattern. Due to the flow deceleration at late-systole, a new vortex is formed at the aneurysm proximal side. At end-systole, the vortex is travelling with the main stream, and at mid-diastole, it has reached the aneurysm distal side. The increase in vortex intensity by incorporation of the initial stress is most prominent during late-systole, end-systole, and mid-diastole. Additionally, the initial stress promotes a shift of the vortex locations, for instance towards the centre of the aneurysm at late-systole and mid-diastole, and an increase of the vortex travel speed, discernable from the vortex location at end-systole. Further it promotes the presence of a secondary vortex at end-diastole. Due to a dependency on the wall deformation, the effects of incorporating the initial stress are also dependent on the wall thickness. Of the cases considered, the effects are most prominent for the 1.0 mm thickness case as shown in the regarded figures.

With respect to the WSS distribution, incorporation of the initial stress yields axially varying profiles globally similar to those in the stress-free case, with more pronounced regions of high WSS (see Figures 3.8 and 3.9). In both cases, the various profiles are typical of the instants of the flow cycle. At end-diastole, the overall WSS level is low due to relatively low flow, and local regions of high WSS are present nearby the vortices inside the aneurysm. At peak-systole, the overall WSS level has increased due to relatively high flow, and a region of high WSS is present at the local constriction of the geometry at the aneurysm distal side. Inside the aneurysm, apart from a small region at the proximal side showing that the flow pattern is not completely attached, there is low WSS due to the local low fluid velocity. At late-systole, the overall WSS level and the distal peak have decreased due to decreased flow, and a region of high WSS is present nearby the vortex originating at the proximal side of the aneurysm. At end-systole, despite the decreased flow compared to late-systole, the overall WSS level has increased due to a phase difference between the boundary layer flow and the flow in the vessel core. At mid-diastole, the overall level is low due to low flow, and a peak is present near the vortex occurring at aneurysm distal side. The emphasis of regions of high WSS by incorporation of the initial stress is most prominent at mid-diastole and peak-systole. Additional shifting of the WSS peaks due to displacement of the vortices inside the aneurysm is discernable at late-systole, end-

systole and mid-diastole. The initial stress additionally promotes local WSS peaks nearby the secondary vortex at end-diastole and a similar one apparently present at mid-diastole. The effects of incorporating the initial stress are more pronounced for thinner walls. In the presence of initial stress, the WSS profiles for different values of the wall thickness are rather similar. Furthermore, when comparing the distensible wall cases with a rigid wall case, it should be noted that the initial stress case is better approximated by the rigid results than the stress-free case.

3.4 Discussion

With respect to the solid problem, it can be concluded that neglect of the initial wall stress leads to an overestimation of the wall deformation. The overestimation is dependent on the wall thickness, which is mainly due to differences in deformation for different values of the wall thickness in the absence of initial stress. In the presence of initial stress, the wall deformation, although generally small, is hardly influenced by the wall thickness. This is caused by the fact that for a given model geometry, the initial stress and initial strain themselves are dependent on the wall thickness. With a geometrically non-linear formulation of the constitutive behaviour, to obtain the level of stress necessary to balance the pressure load acting on the model in the initial state, a thin walled model is required to have gone through larger deformations than a similar model that is thick walled. Therefore, a thin walled model subject to initial stress will exhibit relatively more stiff behaviour than a thick walled model. As a result, the dependence on the wall thickness of the wall deformation during the final pressurisation is decreased.

Neglect of the initial wall stress also leads to an overestimation of the overall stress level and peak wall stress. With respect to the overall stress level, this finding is consistent with findings in solid stress models by Raghavan *et al.* (2006) and Lu *et al.* (2007b). In the latter study, the finding is also confirmed with respect to the peak wall stress. In the first study the peak wall stress was not significantly altered by incorporation of the initial stress, which was probably due to the method used to determine the latter. By the assumption that the displacement field from the stress-free geometry to the model geometry was linearly related to the displacement field resulting from conventional pressurisation of the latter in the absence of initial stress, the model geometry differs from the stress-free geometry only in terms of size. However, it was explained that a spatially varying stress distribution may be more sensitive to differences in shape (Raghavan *et al.*, 2006). In Lu *et al.* (2007b) and in the current study, the initial stress is determined by an inverse solid stress analysis, in which shape differences are accounted for.

Neglect of the initial stress further promotes a more smooth stress distribution, which is consistent with the results of De Putter *et al.* (2007). In that study, incorporation of the initial stress increased the intensity of both high stress and low stress regions, giving a greater span of computed stress values. Unlike in the current study, however, the peak wall stress was found to be increased. This could be due to the fact that in the regarded study, the model geometries were patient-specific and asymmet-

ric, and the computed stress distributions were to a great extent dependent on the local wall curvature. In the current study, the geometry is of an ideal shape, giving a smooth and symmetric stress distribution. For the modelled aneurysm, incorporation of the initial stress will therefore have a similar effect as for the connected straight tube ends. This effect comprises a limitation of the deformation upon loading, as a result of the stress initially present in the wall. Due to the geometrical non-linearity of the computational model, the limited deformation will lead to a decreased surface area subjected to the pressure load as well as an increased wall thickness. Both these effects will lead to a decrease of the stress eventually computed. The fact that this could be different for more arbitrary geometries, is substantiated by the redistribution of the oscillatory stress pattern in the curved wall of the aneurysm itself.

With respect to the fluid problem, neglect of the initial stress leads to an underestimation of the recirculation inside the aneurysm, and an underestimation of the WSS. These results are consistent with previous studies on the effects on the blood velocity distribution and WSS resulting from wall displacement due to vessel distensibility. Although in the current study, the differences in wall displacement between the various cases are due to the presence or absence of initial wall stress, the comparison with the rigid wall case with respect to the WSS profiles indicates that the incorporation of vessel distensibility when regarding a rigid case and the lack of an initial stress model when regarding a distensible case have similar effects. For the sinus of a compliant carotid artery bifurcation model, Perktold and Rappitsch (1995) report a slight decrease of flow separation and recirculation when compared to a rigid wall case, and a decrease of high WSS values by up to 25 percent, while the global flow and stress patterns remain unchanged. For a distensible model of a cerebral aneurysm, Torii *et al.* (2007) report a decrease of the maximal WSS of again 25 percent when compared to a rigid case, with little difference in the global WSS distribution. In the current study, the absolute differences in WSS magnitude are of the same order, with an underestimation of the high WSS values at peak-systole of around 15 percent for the 2.0 mm wall thickness case to 22 percent for the 1.0 mm case. Furthermore, also in the current study there is little difference in the global flow patterns and WSS profiles. The flow patterns and WSS profiles further correspond well with the results of previous studies focussing on the blood velocity distribution and WSS pattern specifically in AAAs (e.g., Egelhoff *et al.*, 1999; Finol *et al.*, 2003; Salsac *et al.*, 2006).

By considering the results of the solid and fluid problems separately, it can further be concluded that for the fluid problem the effects of incorporating the initial stress are of lesser significance than for the solid problem. In the latter, the initial stress affects both the peak wall stress and the overall stress level. In the fluid problem, the initial stress affects mainly the peak WSS values, while the global WSS pattern remains unchanged. This difference is due to the fact that the stress distribution in the solid problem is strongly dependent on the wall displacement, while at a given instant of the flow cycle the WSS pattern in the fluid problem is mainly governed by the global geometry. This is illustrated by respectively the differences between the wall stress distributions and the resemblance of the WSS profiles for different values of the wall thickness in the absence of initial stress, and by the resemblance of the latter with the rigid wall case profiles. Additionally, the dependency of the WSS pattern on the

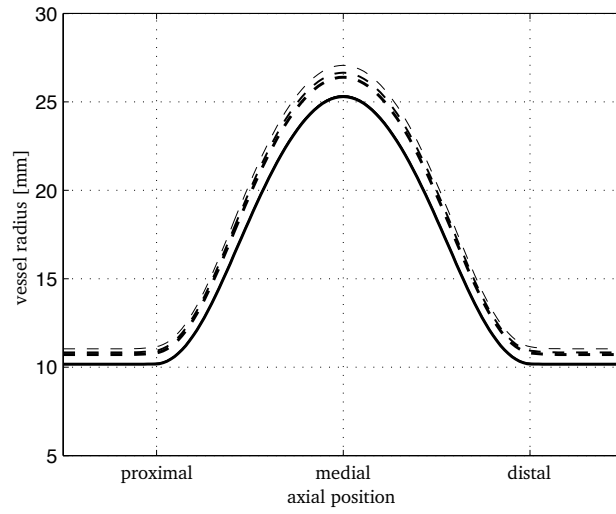
wall displacement is affected by the flow rate. This is illustrated by the WSS profiles at peak-systole and late-systole, where in similar geometries resulting from similar values of the wall pressure load, varying the wall thickness in the absence of initial stress has dissimilar effects.

Finally, based on the resemblance of the WSS profiles of the initial stress case with those of the rigid wall case, it can be concluded that the WSS pattern in the presence of initial stress can be well approximated using a rigid geometry. As such, this finding justifies the rigid wall assumption applied in previous studies (e.g., Salsac *et al.*, 2006; Papaharilaou *et al.*, 2007). It should be noted, however, that for the initial stress case there is better agreement than when comparing the rigid case with the stress-free case. This means that based on the results of the initial stress case, the rigid wall assumption is better justified.

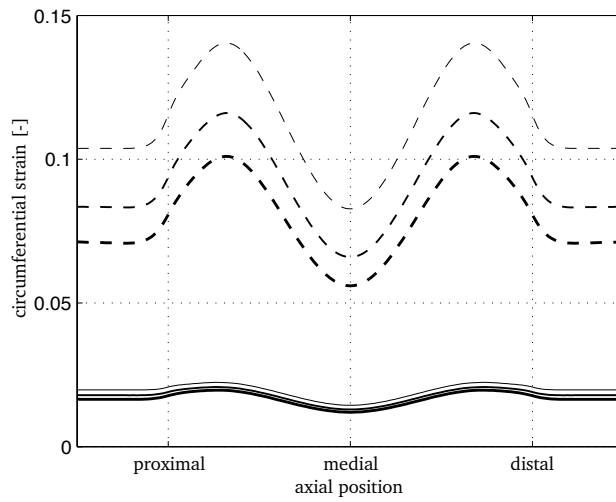
In the interpretation of this study, it should be noted that certain assumptions were made regarding the problem definition and simulation setup. First, the FSI solution procedure was based on a decoupled approach, in which the wall pressure load is independent from the fluid pressure. This approach was substantiated based on previous studies showing no significant difference in peak wall stress for solid stress models and FSI models (Leung *et al.*, 2006; Borghi *et al.*, 2008). Papaharilaou *et al.* (2007) and Scotti and Finol (2007) for FSI models, however, report an increased pressure in the AAA sac compared to solid stress models. It should be noted that the difference in the latter studies is due to the relatively large pressure drop along the aortic bifurcation and iliac arteries that were included in the model geometry. Other assumptions made in the current study were the symmetrical geometry and the homogenous distribution of wall thickness and material properties. Since actual AAAs are of highly complex shape (Sacks *et al.*, 1999) and are characterised by inhomogeneously distributed wall thickness and material properties (Raghavan *et al.*, 2006), the simulation results of the FSI problem will be more irregular for patient-specific geometries than for the current geometry. This however does not invalidate the current study main results, which were obtained comparatively.

3.5 Conclusion

In FSI simulations of AAA, neglect of the initial wall stress leads to an overestimation of the wall deformation, overall stress level, and peak wall stress, and promotes a more smooth stress distribution. It further leads to an underestimation of the recirculation inside the aneurysm, and an underestimation of the WSS. For the fluid problem, however, the effects of incorporating the initial stress are of lesser significance than for the solid problem. As a result, incorporating the initial stress in FSI simulations of AAA mostly is important for accurate modelling of the wall stress. The WSS pattern in the presence of initial stress can be well approximated using a rigid geometry.



(a)



(b)

Figure 3.4: Vessel radius (a) and circumferential strain (b) at peak systolic pressure for 1.0 mm (thin), 1.5 mm (medium), and 2.0 mm (thick) wall thickness in the absence (dashed) and presence (solid) of initial wall stress. It should be noted that the graphs of the vessel radius in the presence of initial stress for different values of the wall thickness appear to coincide.

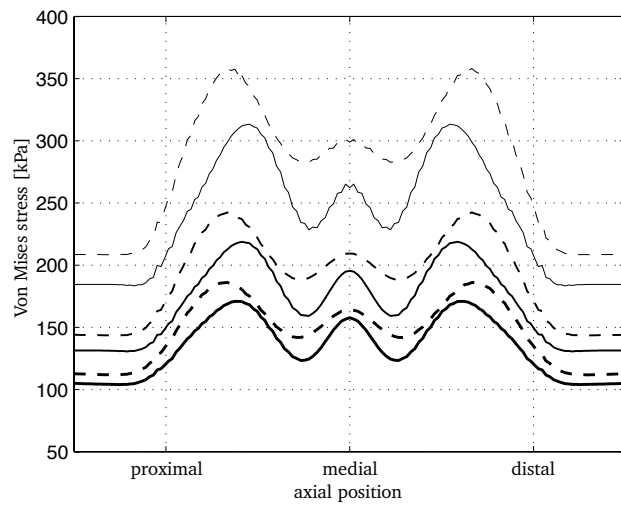


Figure 3.5: Von Mises stress at the wall inner surface at peak systolic pressure for 1.0 mm (thin), 1.5 mm (medium), and 2.0 mm (thick) wall thickness in the absence (dashed) and presence (solid) of initial wall stress.

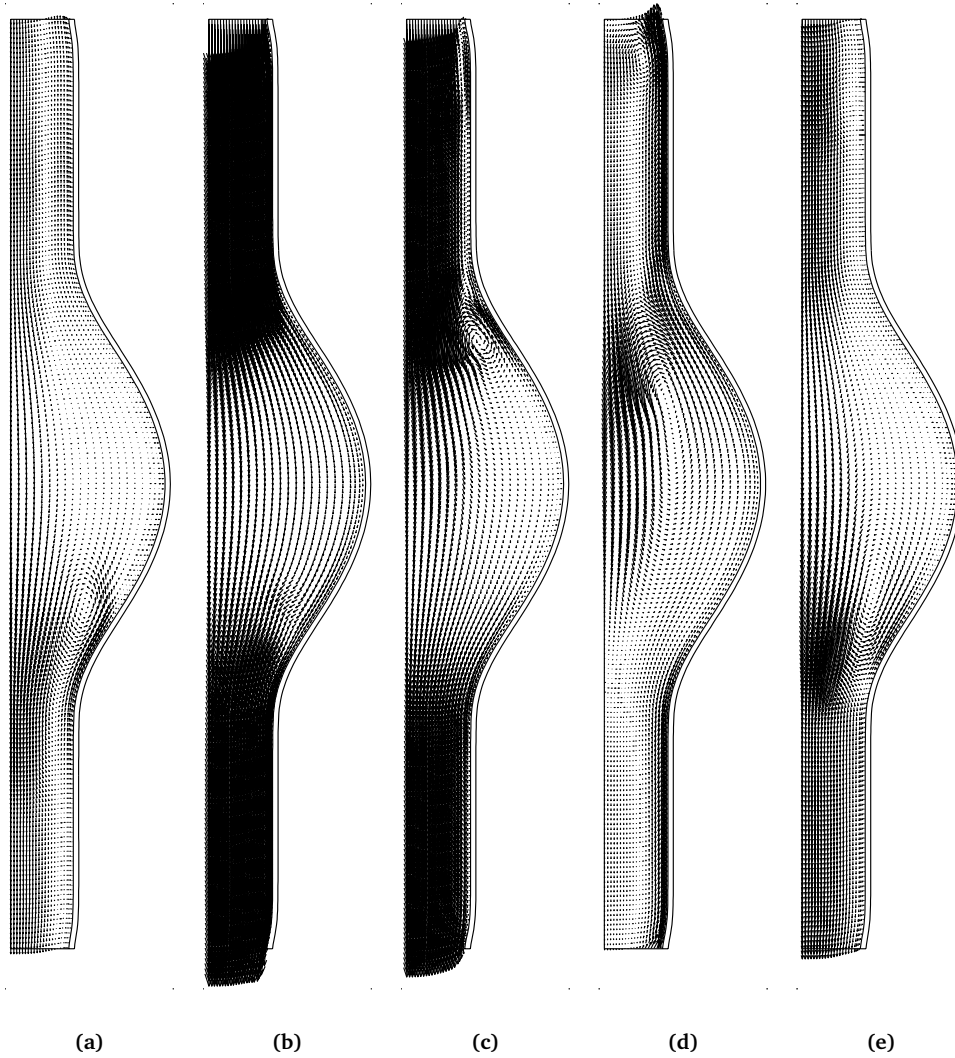


Figure 3.6: Blood velocity distribution and wall geometry at end-diastole (a), peak-systole (b), late-systole (c), end-systole (d), and mid-diastole (e) for 1.0 mm wall thickness in the absence of initial wall stress.

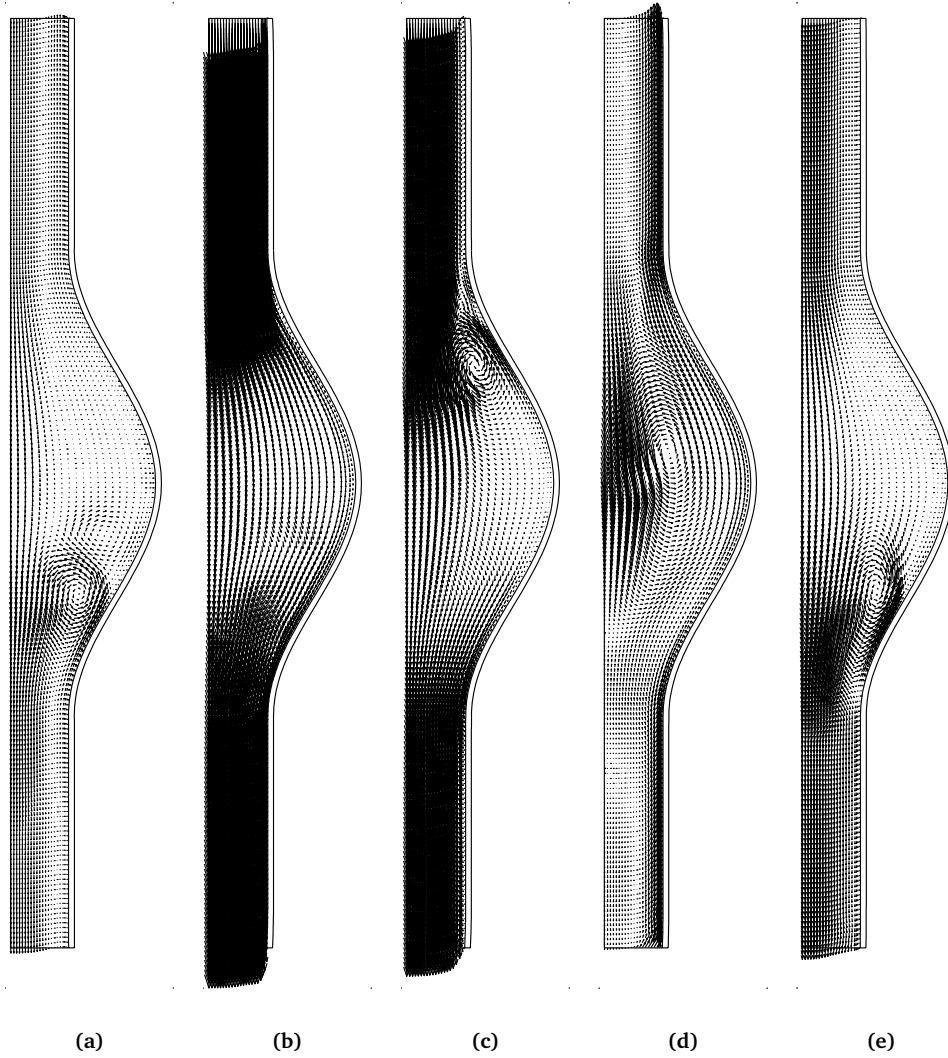
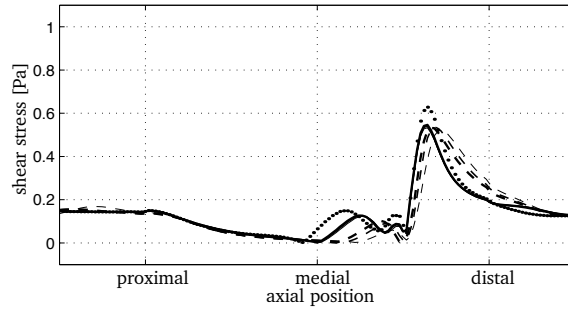
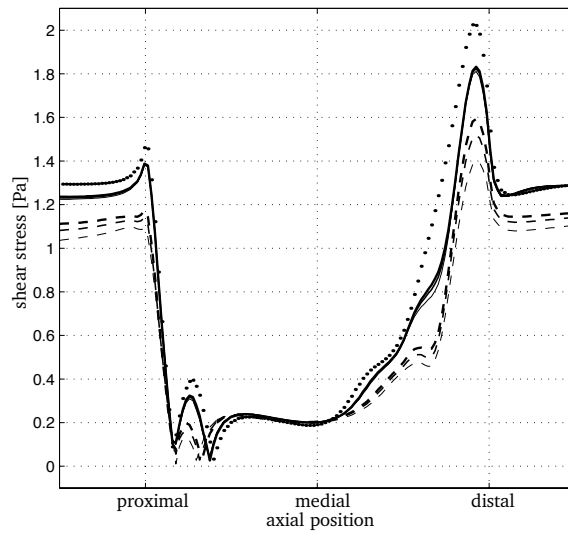


Figure 3.7: Blood velocity distribution and wall geometry at end-diastole (a), peak-systole (b), late-systole (c), end-systole (d), and mid-diastole (e) for 1.0 mm wall thickness in the presence of initial wall stress.

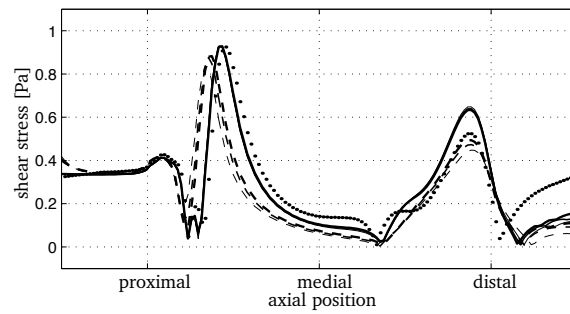


(a) end-diastole

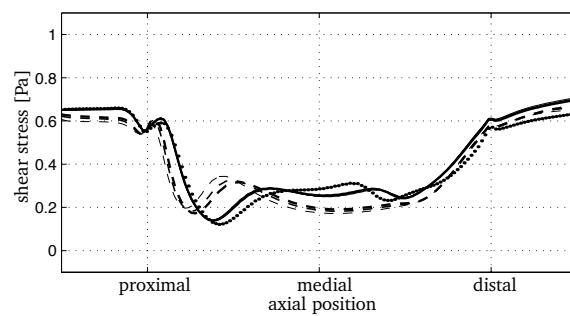


(b) peak-systole

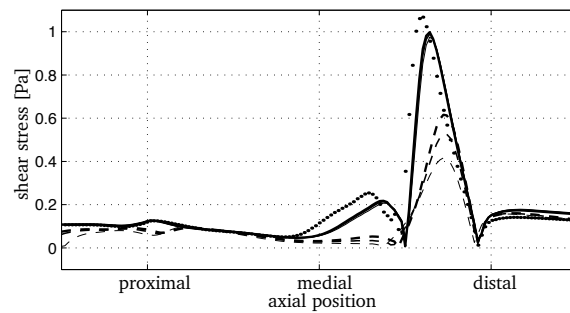
Figure 3.8: Wall shear stress at various instants for 1.0 mm (thin), 1.5 mm (medium), and 2.0 mm (thick) wall thickness in the absence (dashed) and presence (solid) of initial wall stress. It should be noted that the graphs in the presence of initial stress for different values of the wall thickness appear to coincide. The dotted line depicts the rigid wall case.



(a) late-systole



(b) end-systole



(c) mid-diastole

Figure 3.9: Wall shear stress at various instants for 1.0 mm (thin), 1.5 mm (medium), and 2.0 mm (thick) wall thickness in the absence (dashed) and presence (solid) of initial wall stress (continued). It should be noted that the graphs in the presence of initial stress for different values of the wall thickness appear to coincide. The dotted line depicts the rigid wall case.

Chapter 4

Computational modelling of endoleak after endovascular repair of abdominal aortic aneurysms

4.1 Introduction

The outcome of endovascular aneurysm repair (EVAR) of abdominal aortic aneurysms (AAAs) is compromised by the possible occurrence of endoleak (Veith *et al.*, 2002). In EVAR, to reduce the risk of aneurysm rupture, the aneurysmal part of the vessel wall is excluded from the circulation by means of a stent-graft. Endoleak is generally defined as persistent flow between the stent-graft and the excluded vessel wall, and can be classified according to the origin of the flow (White *et al.*, 1997, 1998). Since all types of endoleak lead to continued pressurisation of the aneurysmal sac (Baum *et al.*, 2001), endoleak is assumed responsible for continued risk of rupture. For endoleak related to the stent-graft attachment sites (type I) and endoleak related to stent-graft failure and disconnection (type III), this effect has been demonstrated in a clinical study (van Marrewijk *et al.*, 2002). On a patient-specific basis, however, the nature and significance of endoleak remain poorly understood (Veith *et al.*, 2002).

To better understand the effects of endoleak on the aneurysm intrasac pressure, in a small number of studies, numerical models have been developed for the simulation of endoleak based on coupled fluid-structure interaction (FSI). In a study by Li and Kleinstreuer (2005b), endoleak was represented by small changes of the fluid volume contained by the aneurysmal sac. In this study, it was concluded that for small endoleaks, the intrasac pressure is greatly increased compared to full exclusion. In another study by Li and Kleinstreuer (2006), endoleak was represented by flow through a physical connection of the aneurysmal sac with the aortic lumen. In this

study, it was concluded that relatively large endoleaks yield intrasac pressures close to the systemic pressure. Based on various simulations, the above authors further concluded that in the absence of endoleak, intrasac pressure pulsatility can still be present due to interactions between the luminal blood flow, the stent-graft, the blood comprised by the aneurysm, and the aneurysm wall (Li and Kleinstreuer, 2005a,b).

Although FSI-based models can provide useful information on the fluid dynamics and structural deformations in aneurysms after EVAR, such models may computationally be too expensive if one is solely interested in the effects of endoleak on the risk of aneurysm rupture. In the simulation of endoleak using a weakly coupled method as commonly applied in the simulation of cardiovascular problems (e.g., van de Vosse *et al.*, 2003), numerical instabilities as those observed in the modelling of flow through long compliant vessels (Rutten, 1998) are to be expected. As a result, numerical relaxation of the FSI algorithm is required, that especially for small endoleaks can drastically increase the CPU time needed (see also Li and Kleinstreuer, 2006). The risk of aneurysm rupture could also be gained, however, using only a solid stress model of the aneurysm wall, with an appropriate value of the intrasac pressure applied as boundary condition. The latter could then be determined using a more simplified lumped parameter model describing the relation between the systemic and intrasac pressures as a function of the endoleak size, the stent-graft compliance, and the compliance of the aneurysm wall (Wolters *et al.*, 2007). To this end, however, it should first be determined to what extent lumped parameter models are able to capture the effects of three-dimensional FSI on the aneurysm intrasac pressure in the presence of endoleak as observed in more elaborate models.

To assess the value of lumped parameter models in the simulation of endoleak, in the current study, a lumped parameter-based computational model of an incompletely excluded AAA is developed as well as one based on coupled FSI. The FSI model consists of equations describing the structural deformation of the vessel wall and stent-graft and the blood flow in the endoleak lumen and aneurysmal sac, combined with a solution procedure dedicated to deal with numerical instabilities associated with the simulation of small endoleaks. The lumped parameter model is based on a representation of endoleak using viscosity dominated flow in which fluid inertia is neglected to simulate typical endoleak flow rates. Both models are used to study the aneurysm intrasac pressure for different endoleak sizes and different values of the stent-graft compliance. Based on the agreement of the results of the two models, it is determined whether the lumped parameter modelling method provides a useful alternative to coupled FSI for modelling the aneurysm intrasac pressure in the presence of endoleak and ultimately predicting the risk of aneurysm rupture after EVAR.

4.2 Methods

4.2.1 Geometrical model

The incompletely excluded AAA is modelled as a sinusoidally shaped dilatation of a straight vessel with an inserted cylindrical stent-graft (see Figure 4.1). The problem

is considered symmetrical with respect to both the mid-axial plane and the vessel central axis. At the attachment site, the stent-graft and the aortic wall are separated by an annular region representing the lumen of an endoleak. The vessel dimensions are chosen in the anatomic range, with inflow and maximal diameters of 20 mm and 50 mm, respectively, a total aneurysm length of 80 mm, and a vessel wall thickness of 2.0 mm. The stent-graft wall thickness and endoleak lumen width each are defined as 0.5 mm. The endoleak lumen length is 10 mm.

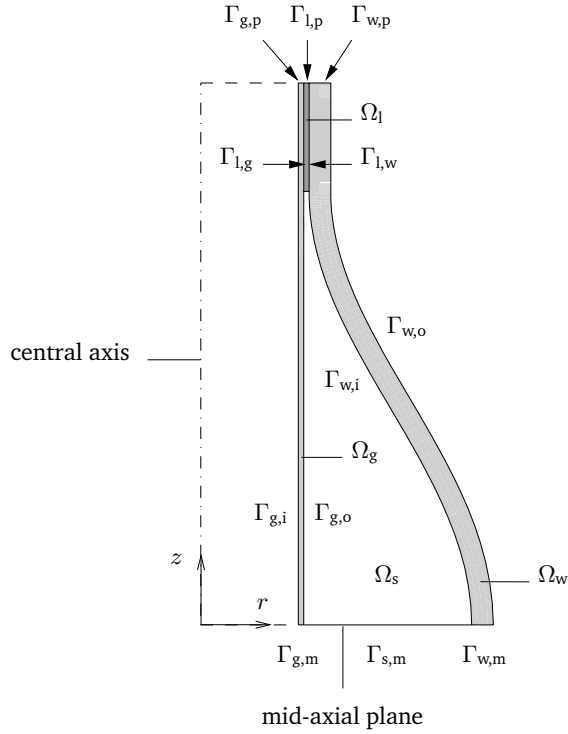


Figure 4.1: Geometry of the incompletely excluded AAA model. The structural domain of the model comprises the stent-graft domain Ω_g , enclosed by the boundaries $\Gamma_{g,i}$, $\Gamma_{g,o}$, $\Gamma_{g,p}$, and $\Gamma_{g,m}$, and the vessel wall domain Ω_w , enclosed by $\Gamma_{w,i}$, $\Gamma_{w,o}$, $\Gamma_{w,p}$, and $\Gamma_{w,m}$. The fluid domain comprises the endoleak domain Ω_l and the aneurysmal sac domain Ω_s . The fluid domain as a whole is enclosed by $\Gamma_{g,o}$, $\Gamma_{w,i}$, $\Gamma_{l,p}$, and $\Gamma_{s,m}$.

4.2.2 Fluid-structure interaction model

In the FSI model, the deformation of the structural part of the model comprising the stent-graft and the vessel wall is described using the equations of motion and continuity. In the absence of body forces, for an incompressible material, these equations

read

$$\begin{cases} \nabla \cdot \boldsymbol{\sigma} = \mathbf{0} \\ \det(\mathbf{F}) - 1 = 0 \end{cases} \quad \text{in } \Omega_g \cup \Omega_w, \quad (4.1)$$

with $\boldsymbol{\sigma}$ the Cauchy stress tensor, and $\mathbf{F} = (\nabla_0 \mathbf{x})^T$ the deformation gradient tensor with respect to the reference state, where \mathbf{x} is the spatial coordinate. The constitutive behaviour of the stent-graft and the vessel wall is described using a linearly elastic neo-Hookean material model:

$$\boldsymbol{\sigma} = -p\mathbf{I} + G(\mathbf{B} - \mathbf{I}), \quad \mathbf{B} = \mathbf{F} \cdot \mathbf{F}^T, \quad (4.2)$$

with p the hydrostatic pressure, \mathbf{I} the unit tensor, \mathbf{B} the Finger tensor, and G the shear modulus. The stent-graft and vessel wall mid-axial cross sections and the proximal wall end are constrained in axial direction. At the endoleak lumen, the local stent-graft boundary is rigidly coupled to the local wall boundary. At the stent-graft inner boundary, the normal stress is prescribed in terms of a given systemic pressure p_{sys} . At the fluid-solid boundaries, the normal stress is prescribed in terms of the local fluid pressure p_f :

$$\begin{aligned} x_z &= x_{z,0} && \text{on } \Gamma_{g,m} \cup \Gamma_{w,m} \cup \Gamma_{w,p}, \\ \nabla_0 \mathbf{x} &= \nabla_0 \mathbf{x}_{\Gamma_{l,w}} && \text{on } \Gamma_{l,g}, \\ \boldsymbol{\sigma} \cdot \mathbf{n} &= -p_{\text{sys}} \mathbf{n} && \text{on } \Gamma_{g,i}, \\ \boldsymbol{\sigma} \cdot \mathbf{n} &= -p_f \mathbf{n} && \text{on } \Gamma_{g,o} \cup \Gamma_{w,i}, \end{aligned} \quad (4.3)$$

with \mathbf{n} the boundary outward normal. If a variable is not prescribed on a certain boundary, a homogeneous Neumann condition is assumed.

The flow in the endoleak lumen and the aneurysmal sac is described using the arbitrary Lagrangian-Eulerian (ALE) formulation of the Navier-Stokes equations. In the absence of body forces, for an incompressible fluid, these equations read

$$\begin{cases} \rho \frac{\partial \mathbf{v}}{\partial t} + \rho(\mathbf{v} - \mathbf{w}) \cdot \nabla \mathbf{v} - \nabla \cdot \boldsymbol{\sigma} = \mathbf{0} \\ \nabla \cdot \mathbf{v} = 0 \end{cases} \quad \text{in } \Omega_l \cup \Omega_s, \quad (4.4)$$

where t denotes time, and with \mathbf{v} the fluid velocity, \mathbf{w} the velocity of the fluid domain, and ρ the density. The constitutive behaviour of the blood is described using an inelastic Newtonian model:

$$\boldsymbol{\sigma} = -p\mathbf{I} + 2\eta\mathbf{D}, \quad \mathbf{D} = \frac{1}{2} [\nabla \mathbf{v} + (\nabla \mathbf{v})^T], \quad (4.5)$$

with p the fluid pressure, \mathbf{D} the rate of deformation tensor, and η the viscosity. At the endoleak lumen proximal end again the normal stress is prescribed in terms of the given systemic pressure p_{sys} , and the radial velocity is constrained to the mesh velocity. At the sac mid-axial cross section, the fluid velocity is constrained in axial direction, and at the fluid-solid boundaries, a no-slip condition is prescribed:

$$\begin{cases} (\boldsymbol{\sigma} \cdot \mathbf{n}) \cdot \mathbf{n} = -p_{\text{sys}} && \text{on } \Gamma_{l,p}, \\ v_r - w_r = 0 && \\ v_z = 0 && \text{on } \Gamma_{s,m}, \\ \mathbf{v} - \mathbf{w} = \mathbf{0} && \text{on } \Gamma_{g,o} \cup \Gamma_{w,i}, \end{cases} \quad (4.6)$$

with r the radial coordinate. Again, if a variable is not prescribed on a certain boundary, a homogeneous Neumann condition is assumed. The fluid domain velocity \boldsymbol{w} is derived from the fluid domain displacement, which is computed using a compressible linearly elastic deformation problem as described in van de Vosse *et al.* (2003), using the wall displacement as boundary condition.

4.2.3 Fluid-structure coupling

The equations of the FSI model are solved in a weakly coupled approach (see Figure 4.2). At initialisation, the fluid velocity \boldsymbol{v} and the mesh velocity \boldsymbol{w} are set to zero, and the fluid pressure p is set to the systemic mean pressure \bar{p}_{sys} . By pressurisation of the structural model, the initial coordinates \boldsymbol{x}_0 are determined. Next, every time step, first, the structural problem is solved to give the wall displacement. Next, the fluid mesh displacement is computed by solving the linearly elastic deformation problem defined on the fluid domain. Finally, the fluid problem is solved, providing the fluid velocity and pressure distributions on the deforming mesh.

To account for numerical instabilities associated with the fluid-structure coupling, the different solution steps are combined in an iterative loop for underrelaxation of the mesh velocity. In this loop, at every iteration, the mesh deformation and the associated mesh velocity \boldsymbol{w} are determined for a given estimate of p . Next, iteratively, without the adjustment of \boldsymbol{w} , the new fluid problem solution and updated mesh coordinates are determined. The loop is set to have converged when the error of p with respect to the initial estimate p^e is less than a criterion ε_p . Next, based on the estimated mesh velocity \boldsymbol{w}^e set at the beginning of the time step, the convergence of \boldsymbol{w} is checked against a criterion ε_w . The iterative loop for the pressure solution is repeated until \boldsymbol{w} has converged. Underrelaxation of \boldsymbol{w} is applied at every first iteration.

4.2.4 Lumped parameter model

The lumped parameter model consists of a resistor representing the flow resistance of the endoleak lumen (R), and two capacitors respectively accounting for the compliance of the stent-graft (C_g) and the compliance of the vessel wall (C_w) (see Figure 4.3). Based on this model, the intrasac pressure p_{sac} can be defined as a function of the systemic pressure p_{sys} . When the signals are expressed as discrete Fourier series:

$$p_{\text{sac}} = \sum_{n=0}^N \hat{p}_{\text{sac},n} e^{in\omega t}, \quad p_{\text{sys}} = \sum_{n=0}^N \hat{p}_{\text{sys},n} e^{in\omega t}, \quad (4.7)$$

with $\hat{p}_{\text{sac},n}$ and $\hat{p}_{\text{sys},n}$ the complex Fourier coefficients of p_{sac} and p_{sys} , respectively, N the number of harmonics, n the harmonic number, ω the fundamental frequency, and i the imaginary number, the relation between p_{sac} and p_{sys} be written as

$$\frac{\hat{p}_{\text{sac},n}}{\hat{p}_{\text{sys},n}} = \frac{1 + in\omega R C_g}{1 + in\omega R (C_g + C_w)}. \quad (4.8)$$

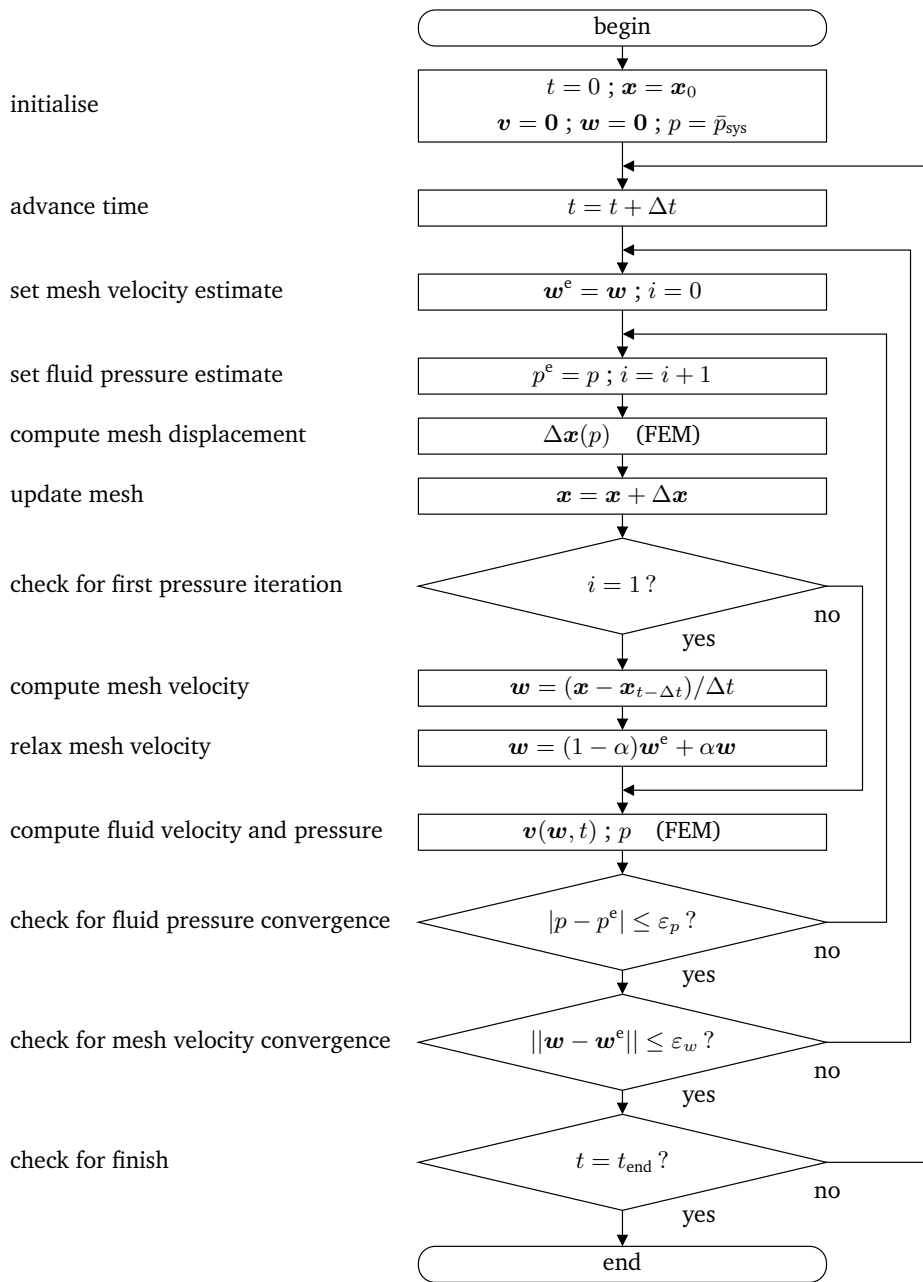


Figure 4.2: Fluid-structure interaction solution procedure (after Rutten, 1998).

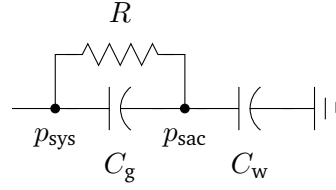


Figure 4.3: Lumped parameter model of the incompletely excluded AAA. The parameters R , C_g , and C_w respectively denote the endoleak resistance, the stent-graft compliance, and the compliance of the vessel wall. The variables p_{sys} and p_{sac} respectively denote the systemic pressure and the intrasac pressure.

In this definition it is assumed that the represented endoleak situation is in periodic state, meaning that both p_{sac} and p_{sys} are time-periodic.

The parameter values of the model are based on geometrical and physical assumptions. The stent-graft compliance and the compliance of the vessel wall are based on the variational area-to-pressure relation of thin-walled tubes:

$$\frac{\partial A}{\partial p} = \frac{2\pi a^3 (1 - \nu^2)}{Eh}, \quad (4.9)$$

with A the tube cross-sectional area, p the internal pressure, a the tube radius, ν the wall material Poisson ratio, E the elastic modulus, and h the wall thickness. The compliance values are determined by integrating (4.9) along the central axis as depicted in Figure 4.1. The resistance of the endoleak lumen is based on the pressure-flow relation for axial flow through an annulus:

$$R = \frac{(P_0 - P_L)}{Q} = \left(\frac{\pi r_o^4}{8\eta L} \left(1 - \kappa^4 + \frac{(1 - \kappa^2)^2}{\ln \kappa} \right) \right)^{-1}, \quad \kappa = \frac{r_i}{r_o}, \quad (4.10)$$

with $(P_0 - P_L)$ the pressure drop, Q the volume rate of flow, L the annulus length, and r_i and r_o the annulus inner and outer radii, respectively (Bird *et al.*, 1960).

4.2.5 Implementation and simulations

For the FSI model, the intrasac pressure to be compared to the lumped parameter model response for a given systemic pressure is defined as the pressure computed in a central point inside the aneurysm, located at the centre of the mid-axial boundary $\Gamma_{s,m}$. The equations of the FSI model are linearised, discretised and solved using the SEPRAN finite element package (SEPRAN BV, The Hague, NL). The lumped parameter model response is the intrasac pressure as computed using (4.8), where the Fourier representation of the systemic pressure signal and the different element parameter values defined by (4.9) and (4.10) are used as input. The response is computed using Matlab (The MathWorks, Inc., Natick, MA). The systemic pressure is based on the

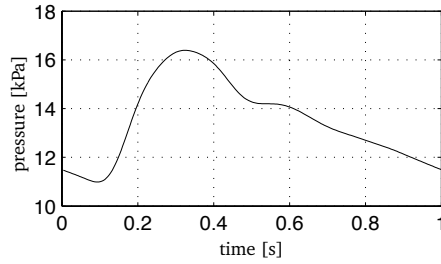


Figure 4.4: Prescribed systemic pressure (after Olufsen *et al.*, 2000).

pressure in the healthy aorta according to Olufsen *et al.* (2000) (see Figure 4.4). The signal is represented using 11 harmonics.

The intrasac pressure is obtained for seven different endoleak sizes and five different values of the stent-graft compliance. The endoleak size is varied by varying the resistance of the endoleak lumen through adjustments to the local viscosity. The stent-graft compliance is varied by adapting the stent-graft shear modulus. For the initial cases, the two parameters equal respectively the viscosity of the blood and the shear modulus of the vessel wall. For the other cases, both parameters are multiplied by increasing powers of two. The viscosity and density of the blood are set to respectively 3.5 mPa s and 1080 kg/m³ (Milnor, 1989). The stent-graft and the vessel wall both are considered incompressible. The shear modulus and elastic modulus of the vessel wall are set to 1.0 MPa and 3.0 MPa, respectively, based on an elastic modulus of around 3 MPa applied by Di Martino *et al.* (2001).

For each of the endoleak sizes, a number of time periods is simulated until the endoleak situation has stabilised. The situation is considered stable when for a certain simulated period, the intrasac mean pressure as compared to the previous period does not vary by more than 1.0 Pa. To limit the simulation time, the solution of the fluid problem for a certain viscosity case is used as initial condition for the following case. Further, the relaxation factor applied for the underrelaxation of the mesh velocity is varied. For the first three viscosity cases, a relaxation factor of 0.05 is used. For the other cases, this value is repeatedly halved. The convergence criteria for the pressure and mesh velocity solutions as described in the appendix are 0.5 Pa and $0.5 \cdot 10^{-3}$ mm/s, respectively.

4.3 Results

For the studied values of the endoleak resistance and stent-graft compliance, the lumped parameter model yields a good approximation of the intrasac pressure as computed by the FSI model (see Figure 4.5). For high stent-graft compliance (see Figure 4.5(a)), the intrasac pressure at low values of the endoleak resistance approximates systemic values. When the resistance is increased, the intrasac pressure is attenuated, while the pressure signal largely remains of the same shape. For higher

resistance, there is better agreement between the lumped parameter model results and the results of the FSI model. For low stent-graft compliance (see Figure 4.5(b)), the intrasac pressure at low endoleak resistance again approximates systemic values. When the resistance is increased, the intrasac pressure signal is both attenuated and subjected to a change of shape. In this case, the attenuation is larger than in the case of high stent-graft compliance. For the FSI model, the intrasac pressure at high endoleak resistance is slightly decreased as compared to the lumped parameter model.

Also the variation of the endoleak flow rate for different values of the endoleak resistance and stent-graft compliance as computed by the FSI model is well approximated by the lumped parameter model (see Figure 4.6). For both high and low stent-graft compliance, the flow rate is decreased with an increase of the endoleak resistance. For low compliance, however, the flow rate at higher values of the endoleak resistance is increased as compared to the case of high compliance. For both cases, for higher endoleak resistance, there is slightly better agreement between the lumped parameter model results and the results of the FSI model.

The agreement of the lumped parameter model results with the results of the FSI model is reflected by the transfer function of the systemic pressure to the intrasac pressure (see Figures 4.7 and 4.8). With an increase of the endoleak resistance, the modulus of the transfer function, describing the amplification of the intrasac pressure signal as compared to the systemic signal, is decreased for all higher harmonics. The minimal level attained by the different moduli is lower for low stent-graft compliance. There is better agreement between the modulus of the lumped parameter model and that of the FSI model for higher resistance (see Figure 4.7). Further, with an increase of the endoleak resistance, the phase of the transfer function, describing the time shift of the intrasac pressure signal, is decreased for the lower harmonics. For the higher harmonics, the phase initially is decreased, after which it is increased again. For low stent-graft compliance, the maximal phase shift is larger than for the case of high compliance. Yet, fluctuations occurring at some of the higher harmonics for the FSI model are also larger. In general, there is better agreement between the phase of the lumped parameter model and that of the FSI model for higher endoleak resistance, except for when the resistance is maximal (see Figure 4.8).

By an analysis of the intrasac pressure in terms of its mean and amplitude it can be seen that the differences occurring between the lumped parameter model results and the results of the FSI model themselves are dependent on the endoleak resistance and stent-graft compliance as well (see Figure 4.9). For the intrasac pressure mean, irrespectively of the endoleak resistance, the value predicted by the lumped parameter model equals the systemic mean. As predicted by the FSI model, however, for higher values of the endoleak resistance, the intrasac pressure mean is lower. The deviation from the systemic mean further is dependent on the stent-graft compliance. With respect to the intrasac pressure amplitude, irrespectively of the stent-graft compliance, the agreement between the results of the two models is better for higher resistance.

4.4 Discussion

The FSI model and the lumped parameter model both predict a decrease of the intrasac pressure amplitude and a decrease of the endoleak flow rate for increasing endoleak resistance. These findings are consistent with the findings of the FSI-based study by Li and Kleinstreuer (2006), who report a decrease of the intrasac peak pressure and a decrease of the endoleak flow rate for smaller endoleak apertures. The findings further agree with experimental studies in which endoleak was found to lead to intrasac pressure pulsatility proportionally related to the flow rate (Schurink *et al.*, 2000a; Mehta *et al.*, 2001; Chong *et al.*, 2003; Wolters *et al.*, 2007). According to the lumped parameter model for all cases studied and according to the FSI model for low endoleak resistance, the size of the endoleak does not seem to influence the intrasac mean pressure. As observed previously in both animal studies (Schurink *et al.*, 2000a; Skillern *et al.*, 2002) and studies using experimental setups (Chong *et al.*, 2003; Wolters *et al.*, 2007), for the cases stated, endoleak yields an intrasac mean pressure that approximates the systemic mean pressure irrespective of the associated flow rate.

For an increase of the stent-graft compliance, the computational models predict a decrease of the intrasac pressure amplitude at low endoleak resistance, an increase of the intrasac pressure amplitude at high endoleak resistance, and associated changes of the endoleak flow rate. The increased pressure amplitude agrees with the findings in Li and Kleinstreuer (2005b), where in the absence of endoleak, the intrasac pressure versus systemic pressure ratio was found to be decreased for an increasing elastic modulus of the stent-graft. Similar findings were reported in Li and Kleinstreuer (2005a). From the synchronicity of the intrasac pressure signal at high stent-graft compliance and maximal endoleak resistance with the systemic pressure signal it can be gathered that the increase of the intrasac pressure amplitude is due to transmission of the systemic pressure pulse to the aneurysmal sac by deformation of the stent-graft. At low stent-graft compliance, the intrasac pressure signal is mainly dependent on transmission through the endoleak lumen. From the intrasac pressure signal for this case it can be deduced that this type of transmission is concerned with significant changes to the signal shape.

From the improved agreement of the lumped parameter model results with the results of the FSI model for higher endoleak resistance it can be gathered that the lumped parameter model in the current configuration is most suited for the simulation of small endoleaks. For the larger endoleaks simulated, where the Reynolds number can obtain values of up to 500, the assumption of viscosity-dominated flow will not always be valid. Therefore, the deviations between the results of the two models at low endoleak resistance presumably are due to neglect of the inertance of the fluid inside the endoleak lumen and aneurysmal sac. This neglect becomes apparent by the relative overshoot of the endoleak flow rate in the FSI model, and relatively low values of the pressure transfer function modulus for the high frequencies in the lumped parameter model. The deviations further can be due to neglect of the flow resistance of the fluid inside the aneurysmal sac. The latter mostly becomes clear from a relative shift of the transfer function phase. Deviations of both kinds decrease

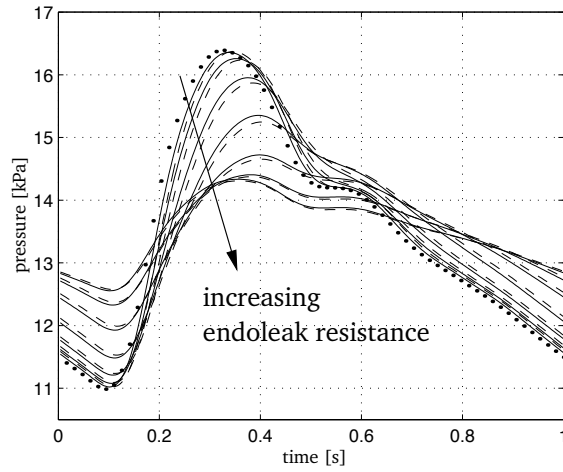
for increasing endoleak resistance due to increasingly dominant viscous flow through the endoleak lumen. To optimise the agreement for large endoleaks, the lumped parameter model should be extended with an inductor in parallel to the main resistor to represent the inertance of the endoleak, and an additional resistor and inductor to represent the flow resistance and inertance of the fluid inside the aneurysmal sac.

The deviations of the intrasac mean pressure in the FSI model as compared to that in the lumped parameter model and the deviations of the pressure transfer function phase for high values of the endoleak resistance denote that for the simulation of small endoleaks the lumped parameter model is better suited than the FSI model. The deviations are likely due to the fact that the applied convergence criteria used to check for a time periodic solution are too large with respect to the applied relaxation factors. A more accurate solution could be obtained using more stringent criteria, at the cost of computational efficiency. Due to inherent instability of the weak fluid-structure coupling of the FSI problem solution procedure, underrelaxation of the mesh velocity, however, remains necessary. The instability is due to the fact that in the current implementation, during the iterative procedure to obtain complementary solutions for the structural problem and the fluid problem, the intermediate solutions of the latter need to comply to the conservation of mass. As a result, at low endoleak resistance, relatively small variations of the wall displacement can lead to significant variations of the endoleak flow. At high resistance, the endoleak flow, however, is limited. The pressure variations resulting from this limitation give rise to the numerical instabilities also observed in the modelling of flow through long compliant vessels (Rutten, 1998). The problem is more serious for higher endoleak resistance, and cannot be solved by selecting a smaller timestep. More stable computations at lower computational cost could possibly be achieved by implementation of a solution procedure that is fully coupled.

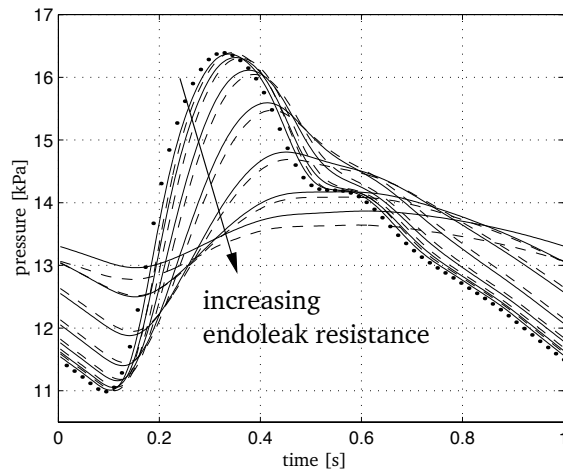
Based on the agreement of the results of the two models it is concluded that the lumped parameter modelling method provides a useful alternative to coupled FSI for modelling the aneurysm intrasac pressure in the presence of endoleak and to give a pressure boundary condition for solid stress analyses to predict the risk of aneurysm rupture after EVAR. It should be noted, however, that the models developed in this study are intended to give a phenomenological representation of endoleak rather than one that is anatomically and physiologically realistic. In reality, type I endoleak is not likely to occur along the full circumference of the inserted stent-graft. Further, the intrasac pressure will also depend on factors not included in the models, such as endoleak thrombosis and the presence of thrombus inside the aneurysmal sac, the presence of an outflow tract connected to the sac, and the occurrence of other types of endoleak. With respect to the vessel wall and the stent-graft, the current models do not incorporate realistic geometries, non-homogeneous mechanical properties, or initial stress. Due to the comparative nature of this study, however, these shortcomings are of limited importance.

4.5 Conclusion

In the current study, a lumped parameter-based computational model of an incompletely excluded AAA has been developed as well as one based on coupled FSI. Both models predict a decrease of the intrasac pressure amplitude and a decrease of the endoleak flow rate for increasing endoleak resistance. For an increase of the stent-graft compliance, the models predict a decrease of the intrasac pressure amplitude at low endoleak resistance, an increase of the intrasac pressure amplitude at high endoleak resistance, and associated changes of the endoleak flow rate. Based on the agreement of the results of the two models it is concluded that the lumped parameter modelling method provides a useful alternative to coupled FSI for modelling the aneurysm intrasac pressure in the presence of endoleak and to give a pressure boundary condition for solid stress analyses to predict the risk of aneurysm rupture after EVAR.

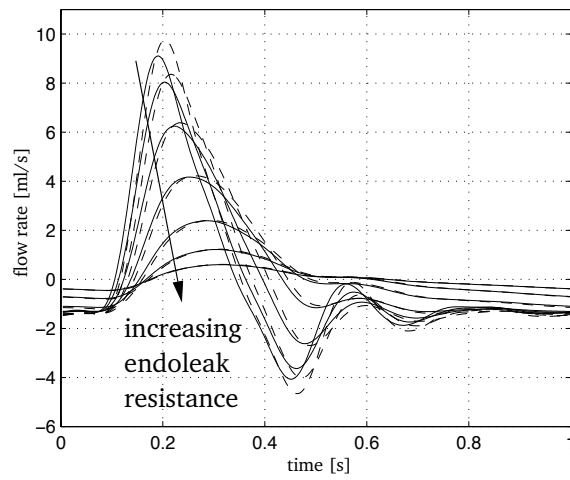


(a) high stent-graft compliance

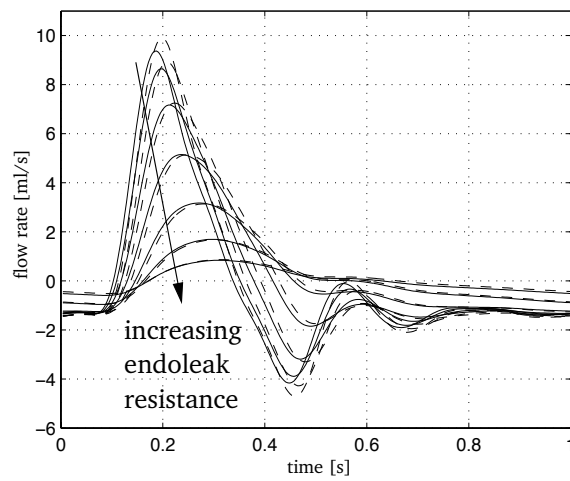


(b) low stent-graft compliance

Figure 4.5: Intrasac pressure for different values of the endoleak resistance in the FSI model (dashed) and lumped parameter model (solid) for high and low stent-graft compliance. The dotted line depicts the systemic pressure.

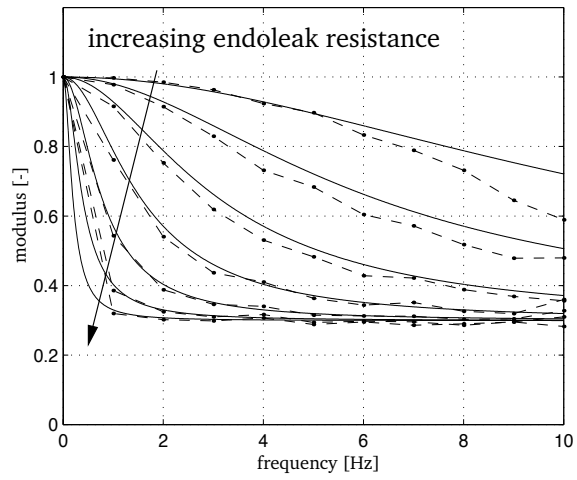


(a) high stent-graft compliance

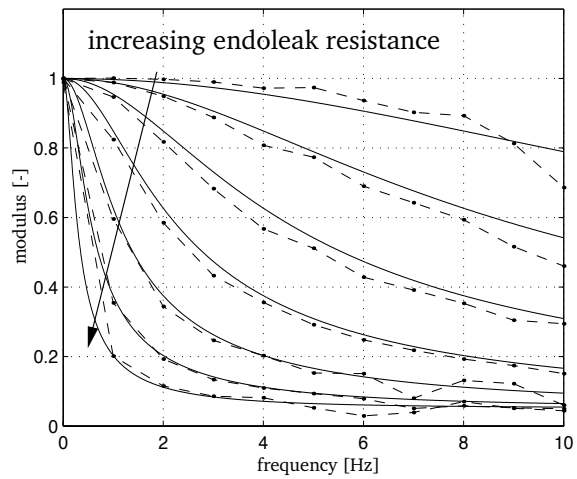


(b) low stent-graft compliance

Figure 4.6: Endoleak flow rate for different values of the endoleak resistance in the FSI model (dashed) and lumped parameter model (solid) for high and low stent-graft compliance.

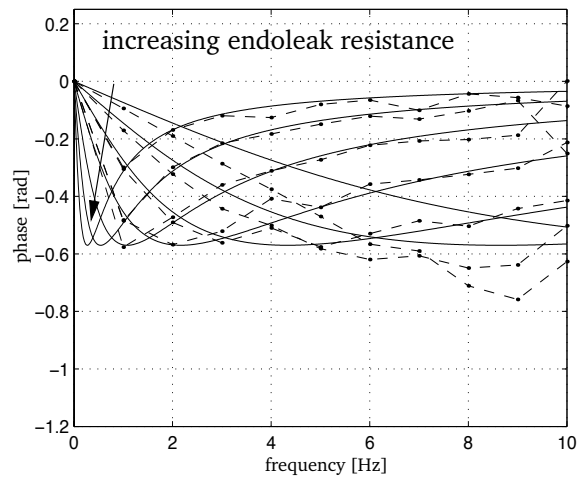


(a) high stent-graft compliance

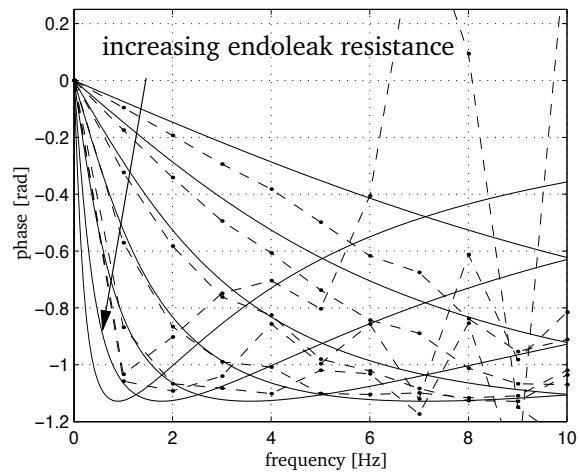


(b) low stent-graft compliance

Figure 4.7: Modulus of the transfer function of the systemic pressure to the intrasac pressure for different values of the endoleak resistance in the FSI model (dashed) and lumped parameter model (solid) for high and low stent-graft compliance.

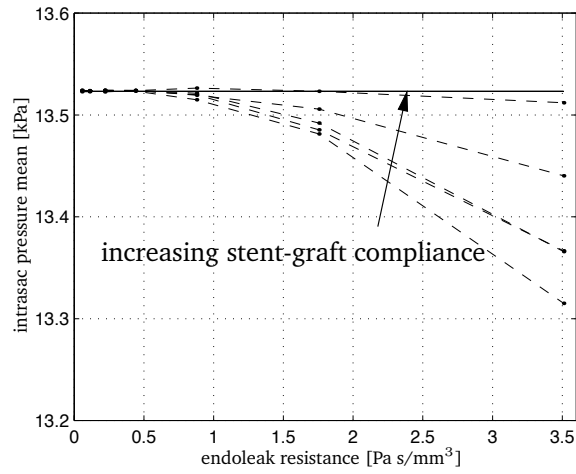


(a) high stent-graft compliance

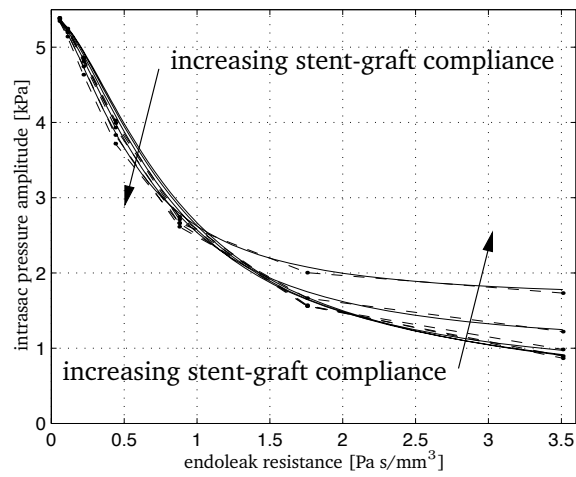


(b) low stent-graft compliance

Figure 4.8: Phase of the transfer function of the systemic pressure to the intrasac pressure for different values of the endoleak resistance in the FSI model (dashed) and lumped parameter model (solid) for high and low stent-graft compliance.



(a) mean



(b) amplitude

Figure 4.9: Intrasac pressure mean and amplitude for different values of the endoleak resistance and stent-graft compliance in the FSI model (dashed) and lumped parameter model (solid).

Chapter 5

Assessment of endoleak significance after endovascular repair of abdominal aortic aneurysms: a lumped parameter model*

5.1 Introduction

The outcome of endovascular aneurysm repair (EVAR) of abdominal aortic aneurysms (AAAs) is greatly compromised by the possible occurrence of endoleak (Veith *et al.*, 2002). In general, endoleak is defined as persistent flow between the stent-graft and the excluded vascular segment (White *et al.*, 1997, 1998). All types of endoleak yield continued pressurisation of the aneurysm sac (Baum *et al.*, 2001). Since high intrasac pressure is associated with AAA expansion (Dias *et al.*, 2004), endoleak is assumed responsible for increased risk of rupture. In a recent multicenter study, for both endoleak related to the stent-graft attachment sites (type I) and endoleak related to stent-graft failure and disconnection (type III), this effect has indeed been demonstrated (van Marrewijk *et al.*, 2002). On a patient-specific basis, however, the nature and significance of endoleak remain poorly understood (Veith *et al.*, 2002).

Previously, the causes and effects of endoleak originating from the aortic lumen have mainly been investigated in experimental studies. In an animal study of saccular

*The contents of this chapter are based on *Med Eng Phys*, 29, 1106–1118, 2007:

**Assessment of endoleak significance after endovascular repair of abdominal aortic aneurysms:
a lumped parameter model**

B.J.B.M. Wolters, M. Emmer, M.C.M. Rutten, G.W.H. Schurink, F.N. van de Vosse

aneurysms connected to the aorta by an endoleak channel, Schurink *et al.* (2000a) showed that irrespective of the channel dimensions, endoleak yields an identical intrasac mean pressure (\bar{p}_{sac}) compared to the systemic mean pressure (\bar{p}_{sys}) measured in the aorta. The intrasac pressure pulsatility, however, was inversely related to the endoleak channel diameter, and was obliterated by thrombosis of the channel. The first finding was confirmed both by Skillern *et al.* (2002) using animal models of an excluded aneurysm with an attachment site failure and by Chong *et al.* (2003) using setups of an excluded aneurysm with either an attachment site failure or a partially permeable stent-graft. The second finding also was confirmed by Chong *et al.* (2003), who reported a decrease of the intrasac pressure pulsatility for lesser degrees of endoleak. Further, in a study on thrombosed endoleak channels by Mehta *et al.* (2001), it was reported that the reduction of the intrasac peak systolic pressure ($p_{\text{sac}}^{\text{s}}$) was inversely proportional to the channel diameter and directly proportional to its length. In studies of setups of incompletely excluded AAAs it was further shown that the intrasac pressure due to endoleak is reduced in the presence of an outflow tract formed by a branching vessel (Parodi *et al.*, 2001; Chong *et al.*, 2003). Finally, pulsatility of the intrasac pressure was also shown present in fully excluded aneurysms in both studies of experimental setups (Parodi *et al.*, 2001; Chong *et al.*, 2003; Gawenda *et al.*, 2003a; Mehta *et al.*, 2003) and animal studies (Skillern *et al.*, 2002).

Despite that experimental studies themselves can provide insight into the consequences of endoleak in specific situations, the results of various experiments from literature are hard to compare. This is mainly due to the fact that of different studies using apparently similar setups, varying results have been reported. Using a setup comparable to that of Chong *et al.* (2003), Schurink *et al.* (1998) for various degrees of endoleak found that \bar{p}_{sac} was decreased compared to \bar{p}_{sys} . The value of $p_{\text{sac}}^{\text{s}}$ was decreased as well compared to the systemic peak systolic pressure ($p_{\text{sys}}^{\text{s}}$), while the intrasac and systemic diastolic pressures ($p_{\text{sac}}^{\text{d}}$ and $p_{\text{sys}}^{\text{d}}$) were similar. Again for various degrees of endoleak, Parodi *et al.* (2001) found that \bar{p}_{sac} was increased compared to \bar{p}_{sys} . Again, $p_{\text{sac}}^{\text{s}}$ was decreased compared to $p_{\text{sys}}^{\text{s}}$, but $p_{\text{sac}}^{\text{d}}$ was higher than $p_{\text{sys}}^{\text{d}}$. Using a perforated stent-graft, Mehta *et al.* (2003) found $p_{\text{sac}}^{\text{d}}$ and $p_{\text{sac}}^{\text{s}}$ both to be even higher than $p_{\text{sys}}^{\text{s}}$. With respect to the effect of a possible outflow tract, the latter further reported that the intrasac pressure pulsatility was increased rather than reduced in the case of full exclusion, and that $p_{\text{sac}}^{\text{s}}$ and $p_{\text{sac}}^{\text{d}}$ were equal rather than reduced compared to systemic pressures in the presence of endoleak. Finally, Schurink *et al.* (1998) found the intrasac pressure in fully excluded aneurysms to be fully obliterated rather than being non-zero.

In order to both reconcile and physically substantiate the various findings of the experimental endoleak studies described in literature, in this study, a computational model of an incompletely excluded AAA is developed. After experimental validation, the model is applied to study the effects on the intrasac pressure after EVAR of AAA of the degree of endoleak, the degree of stent-graft compliance, and the resistance of a possible outflow tract formed by a branching vessel. In addition to elucidating previous observations, the results of this study could help to assess the significance of endoleak in individual patients using intrasac pressure measurements by means of implantable sensors (e.g., Ellozy *et al.*, 2004; Milner *et al.*, 2004). Furthermore,

the computational model developed in this study could help to provide boundary conditions for simulations of the effects of endoleak on the AAA wall stress using computational methods based on 3D fluid-structure interaction (e.g., Wolters *et al.*, 2005).

5.2 Methods

5.2.1 Aortic tree model

Based on the arterial tree model by Westerhof *et al.* (1969), a lumped parameter model of the human aortic tree is generated, incorporating an excluded AAA in the presence of both an endoleak channel and an outflow tract. The model comprises several modules representing segments of the aorta and large connected vessels (see Figure 5.1(a)). Each module is built from resistors, inductors, and/or capacitors, that respectively account for the blood viscous properties, the blood inertial properties, and the vessel wall or stent-graft compliance (see Figures 5.1(b) and 5.1(c)). The elements are mutually connected by nodal points. At the branch ends, the modelled vessels are terminated by Windkessel modules representing distal vascular beds (see Figure 5.1(d)). The AAA is modelled by a single capacitor, and the endoleak channel and the outflow tract are both modelled by single resistors (see Figure 5.1(a)). All outflow resistors and the capacitors of the segmental and Windkessel modules as well as the capacitor representing the AAA are connected to a standard reference at zero-pressure. For the capacitors of the stent-graft modules, the reference pressure is the intrasac pressure p_{sac} .

The behaviour of the lumped parameter model is described by a set of equations that is derived from the behaviour of the constituting elements. With $\underline{q} = (q_1, q_2)^T$ the column of locally defined nodal flows, and $\underline{p} = (p_1, p_2)^T$ the column of local nodal pressures, the behaviour of the resistors, inductors, and capacitors, respectively, can be described by

$$\dot{q}_R(t) = \underline{R}\dot{\underline{p}}(t); \quad \dot{q}_L(t) = \underline{L}\underline{p}(t); \quad \dot{q}_C(t) = \underline{C}\ddot{\underline{p}}(t), \quad (5.1)$$

with

$$\underline{R} = \frac{1}{R} \begin{pmatrix} 1 & -1 \\ -1 & 1 \end{pmatrix}; \quad \underline{L} = \frac{1}{L} \begin{pmatrix} 1 & -1 \\ -1 & 1 \end{pmatrix}; \quad \underline{C} = C \begin{pmatrix} 1 & -1 \\ -1 & 1 \end{pmatrix} \quad (5.2)$$

the element matrices, where R denotes the element resistance, L the element inductance, and C the element capacitance. By assembling the equations describing the behaviour of the different elements in the aortic tree model, using the property that coinciding local nodes have equal pressures and balanced flows, the set of equations describing the total model behaviour can be written as:

$$\underline{C}\ddot{\underline{p}}(t) + \underline{R}\dot{\underline{p}}(t) + \underline{L}\underline{p}(t) = \dot{\underline{q}}(t), \quad (5.3)$$

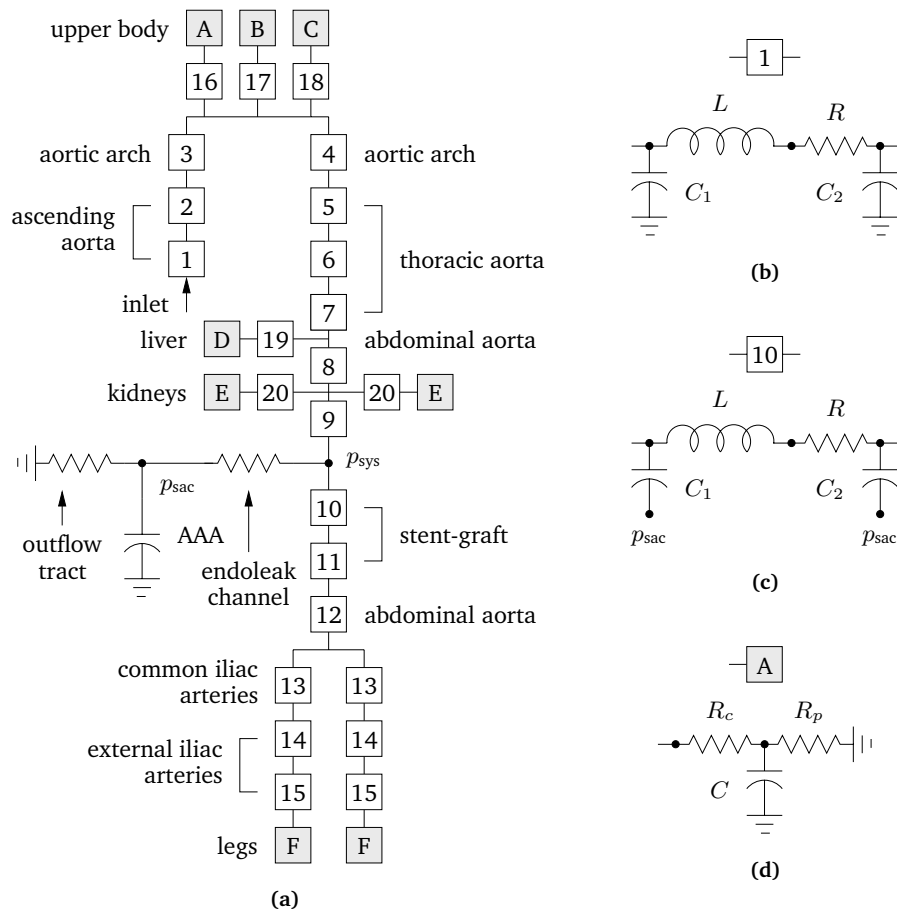


Figure 5.1: Layout of the aortic tree model with an excluded AAA in the presence of an endoleak channel and an outflow tract (a), and configurations of the segmental modules (b), stent-graft modules (c), and Windkessel modules (d). Resistors are indicated by their resistance R , inductors by their inductance L , and capacitors by their capacitance C . The variables p_{sac} and p_{sys} denote the intrasac pressure and the systemic pressure measured in the aorta, respectively.

where now \underline{p} denotes the column of pressures in the globally numbered nodal points, \underline{q} denotes the column of globally prescribed external flows, and \underline{C} , \underline{R} , and \underline{L} contain the assembled element matrices.

The parameter values of the elements constituting the different modules of the aortic tree model are based on literature. Of the segmental modules, the parameter values are directly gathered from Westerhof *et al.* (1969), who for the various segments of the arterial tree in Figure 5.1(a) report the laminar flow resistance, the fluid inertance, and the wall compliance. These properties are assigned to respectively the resistor, the inductor and the two capacitors depicted in Figure 5.1(b), where C_1 and C_2 each represent half of the total compliance C . Of the Windkessel modules, the parameters are determined such that the module input impedance approximates that of the represented vascular bed (e.g., Stergiopoulos *et al.*, 1999, see Appendix B.1).

The parameter values of the remaining elements are either determined based on geometrical and physical assumptions, or considered as free model parameters. Based on the assumption that the modelled stent-graft is of the same shape as the excluded section of the abdominal aorta in healthy state, the resistance and the inductance of the stent-graft modules are based on the properties of the abdominal aortic segments of the original model by Westerhof *et al.* (1969). The compliance of the element representing the aneurysm is based on the variational area-to-pressure relation of thin-walled tubes

$$\frac{\partial A}{\partial p} = \frac{2\pi a^3 (1 - \nu^2)}{Eh}, \quad (5.4)$$

where A denotes the tube cross sectional area, p the internal pressure, a the tube radius, ν the wall material Poisson ratio, E the elastic modulus, and h the wall thickness (Milnor, 1989). The compliance is determined by integrating (5.4) along the axis of an aneurysm of an assumed sinusoidal shape. The remaining element parameter values that are considered as free model parameters are the compliance of the stent-graft modules, the resistance of the element representing the outflow tract, and the resistance of the element representing the endoleak channel.

The actual parameter values are given in Appendix B.2. To determine these values, the desired mean and pulse pressures that are applied in the definition of the Windkessel module parameters as described in Appendix B.1 are defined as 100 and 40 mmHg (or 13 and 5.3 kPa), respectively. Further, with a mean flow rate at the inlet of 95 ml/s, based on a physiologic flow signal as depicted in Figure 5.2, the time constant τ as defined in the appendix is determined as 1.36 s. Finally, the aneurysm compliance is determined as 0.65 ml/kPa, based on assumed minimal and maximal diameters of 20 and 55 mm, respectively, and a length of 85 mm, which is 80 percent of the length of the infrarenal abdominal aorta in the model by Westerhof *et al.* (1969). Other properties that are applied to determine the compliance are $\nu = 0.5$, $E = 2.7$ MPa (Di Martino *et al.*, 2001), and $h = 2.0$ mm (Raghavan and Vorp, 2000b; Thubrikar *et al.*, 2001a).

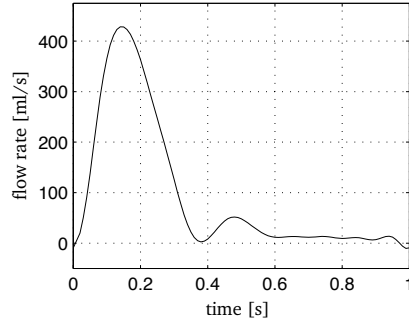


Figure 5.2: Flow rate at the inlet of the physiologic model (after Olufsen *et al.*, 2000).

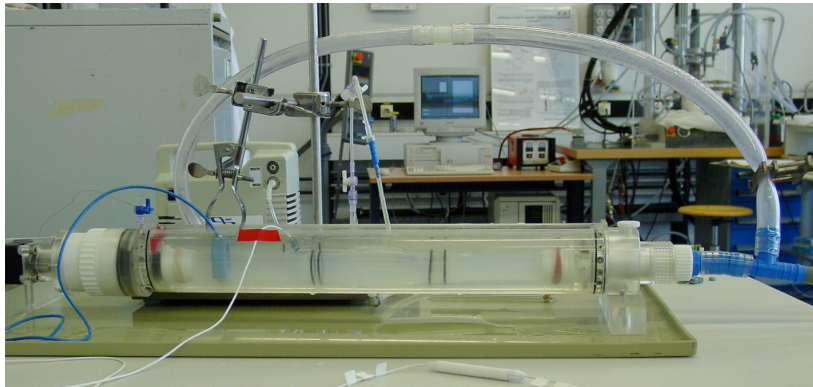
5.2.2 Experimental setup

To validate the lumped parameter modelling method, an experimental setup of an incompletely excluded aneurysm is developed (see Figures 5.3(a) and 5.3(b)). The aneurysm is modelled as a local dilatation of a poly-urethane (PU) tube. The input of the tube is connected to a piston pump driven by a computer-controlled linear motor (ETB32, Parker Hannifin Corp., Cleveland, OH), drawing fluid from a collecting system filled with water. By means of an adjustable outflow resistance, the output of the tube is also connected to the collecting system. In addition, the tube is connected to a Windkessel model consisting of a silicone tube partially filled with air that is locally constricted by means of an adjustable clamp to provide a resistance at its inlet. The aneurysm is excluded from the main circulation by means of an inserted glass tube. An endoleak is modelled by a small channel connecting the main tube to the aneurysm sac. The endoleak channel comprises two small PU tubes that are interconnected by a replaceable glass mid-section. By applying mid-sections of various diameters, the size of the channel can be varied.

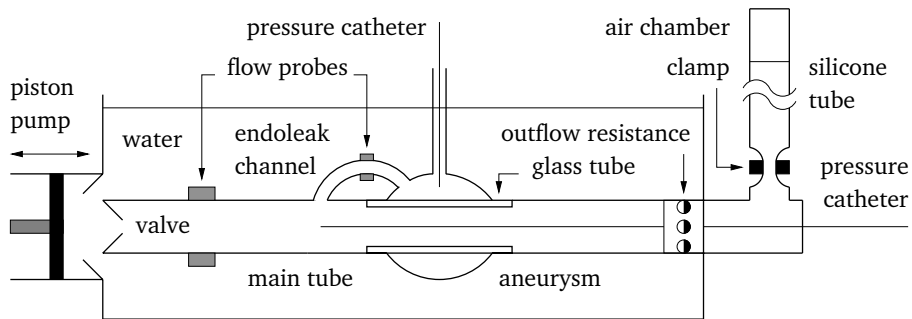
In both the aneurysm and the setup main tube, the pressure response to the flow prescribed at the inlet can be measured by means of pressure catheters (PressureWire-4, Radi Medical Systems AB, Uppsala, Sweden). Further, in both the main tube and the endoleak channel, fluid flow rates can be measured by means of ultrasonic flow meters (TS420, Transonic Systems Inc., Ithaca, NY). The piston pump is adjusted such that the prescribed mean flow is 1.2 l/min at 70 bpm, with a flow signal as depicted in Figure 5.4. The constriction of the silicone tube and the outflow resistance are adjusted such that the systemic pressure varies between 10 and 20 kPa.

Based on the experimental setup, an additional lumped parameter model is developed (see Figure 5.3(c)). Of this model, the segmental module resistance and inductance values are based on physical balance laws applied to tubular sections of the setup subjected to fully developed Newtonian flow (e.g., Milnor, 1989). In this respect, the parameter R in (5.1) is regarded as the laminar flow resistance, defined by

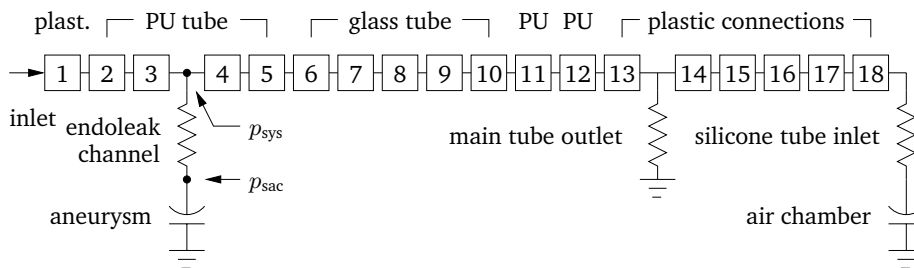
$$R = \frac{8\eta l}{\pi a^4}, \quad (5.5)$$



(a)



(b)



(c)

Figure 5.3: Experimental setup of an incompletely excluded abdominal aortic aneurysm: photographic image (a), schematic representation (b), and lumped parameter model (c). The variables p_{sac} and p_{sys} denote the intrasac pressure and the systemic pressure measured in the main tube, respectively.

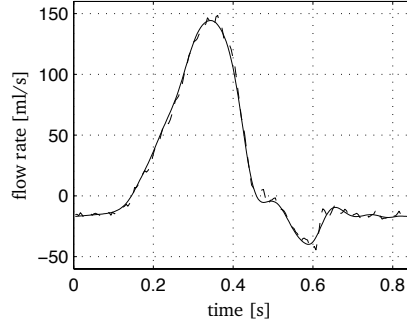


Figure 5.4: Flow rate at the inlet of the experimental setup: measured in the experiment (dashed) and prescribed in the simulation (solid).

with η the fluid viscosity, l the section length, and a the section radius. The parameter L is regarded as the inertance of the fluid contained by the section, defined by

$$L = \frac{\rho l}{\pi a^2}, \quad (5.6)$$

with ρ the fluid density. The actual parameter values are based on the physical properties of water ($\eta = 1.0 \text{ mPa s}$, $\rho = 1.0 \cdot 10^3 \text{ kg/m}^3$). Further, since the exact wall thickness and mechanical properties of the PU models are unknown, the compliance values of the modules representing the main tube sections are determined experimentally. By subjecting the tube to an internal pressure and measuring the additionally stored fluid volume in the absence of an endoleak channel, the main tube total compliance is estimated. From this value, the compliance per unit length is determined, which is then used to calculate the compliance per section. The glass tube and connecting plastic tubes are considered rigid.

The dimensions of the different tubular sections of the setup upon which the segmental module properties are based along with the properties of the remaining elements are given in Appendix B.3. The modelled aneurysm is of 80 mm length and 55 mm maximal diameter. The compliance of the aneurysm is estimated using an additional pressurisation experiment of the main tube with an endoleak channel present. The air chamber compliance is determined based on Boyle's law. With respect to the endoleak channel, the different mid-sections are of 50 mm length and of 0.85 (small), 1.6 (medium), and 2.4 mm diameter (large). Including the side tubes of 35 mm length and 4.0 mm diameter, the channel resistance values are again based on (5.5). Further, the resistance at the main tube outlet is determined by dividing the mean of the measured main tube pressure by the mean of the measured systemic flow. The resistance at the silicone tube inlet is determined experimentally, by subjecting the tube to a pressure difference and measuring the resulting flow.

5.2.3 Validation and simulations

Using the setup of Figure 5.3(a), an experiment is performed in which the pressure response to the prescribed flow at the inlet is measured in both the main tube and the modelled aneurysm. The experiment is performed both in the absence of an endoleak channel and in the presence of the small, medium, and large sized channels. At the start of the experiment, the measured pressures are initialised at 0 kPa. During the experiment, the pressures are monitored to check for differences between consecutive periods. The actual recordings are only performed after a periodic steady state has been reached.

The experiment is numerically simulated using the lumped parameter model of Figure 5.3(c). After passing the signal through a low-pass Butterworth filter in order to reduce noise, the measured systemic flow is prescribed as boundary condition at the inlet of the model (see Figure 5.4). At the points connected to the standard reference, a zero-pressure is prescribed. After specification of the initial conditions

$$\underline{p}(t=0) = 0 \quad ; \quad \underline{\dot{p}}(t=0) = 0 \quad ; \quad \underline{\ddot{p}}(t=0) = 0, \quad (5.7)$$

the pressure response of the model is determined by numerical integration of Eq. (5.3) using a Newmark difference scheme implemented in Matlab (The MathWorks, Inc., Natick, MA). The procedure is repeated for the resistance values representing the small, medium, and large sized endoleak channels. To compensate for possible pressure losses due to bends and sudden changes in flow area that are not incorporated in the calculation of these resistances, the values are scaled such that the simulated endoleak channel flow rates roughly match those in the experiment. Similarly, the measured value of the main tube compliance is adjusted in order to match the simulated systemic pulse pressure to the systemic pulse pressure that is measured, and the aneurysm compliance is adjusted to match the simulated and measured values of the pulse pressure inside the aneurysm. The scaling factors are given in Table B.5.

Finally, the lumped parameter model of the physiologic situation in Figure 5.1 is applied to simulate the in-vivo aortic and intrasac pressures after EVAR of AAA, and to assess the effects on these of the degree of endoleak, the degree of stent-graft compliance, and the resistance of the outflow tract. The boundary conditions, initial conditions, and solution procedure are again as described above, where the flow prescribed at the inlet is based on a measured physiologic flow signal from literature (see Figure 5.2). Using variations of the main model, three types of simulation are performed. In the first type, the effect of endoleak is ignored by removal of the element representing the endoleak channel. In the second type, the effect of the outflow tract is ignored by removal of the outflow tract element. In the last type, the stent-graft is assumed rigid by removal of the stent-graft module capacitors. In each type of simulation, results are obtained for various combinations of the remaining two degrees of freedom to be studied. Each of the two parameters is exponentially varied within a specific interval defined around a standard value. The lower and upper boundaries of the interval are defined in proportion to the standard value, at 10 and 1000 percent, respectively. With regard to the stent-graft compliance, the standard value is defined at 10 percent of the AAA compliance, which amounts to 0.65 ml/kPa.

Table 5.1: Measured (*meas.*) and simulated (*sim.*) mean systemic and intrasac pressures in the experimental setup in the absence of an endoleak channel and in the presence of small, medium, and large-sized channels.

| endoleak channel | systemic pressure (kPa) | | intrasac pressure (kPa) | |
|------------------|-------------------------|-------------|-------------------------|-------------|
| | <i>meas.</i> | <i>sim.</i> | <i>meas.</i> | <i>sim.</i> |
| none | 13.3 | 13.3 | -0.3 | 0.0 |
| small | 14.3 | 14.3 | 13.7 | 14.2 |
| medium | 14.4 | 14.4 | 13.7 | 14.4 |
| large | 14.0 | 14.0 | 13.3 | 14.0 |

The standard resistance value of both the endoleak and the outflow tract is defined at 100 times the highest resistance present in the original model, which amounts to 6.3 Pa s/ml.

5.3 Results

The lumped parameter model of the experimental setup yields good approximations of the experimentally measured pressure signals (see Figure 5.5). In the absence of an endoleak channel, in both the numerical model and the experiment, p_{sac} is negligible compared to p_{sys} . Further, the measured and simulated systemic signals have equal amplitudes. The simulated signal, however, is smoother than the measured signal, and the two present a mutual phase difference of about 0.05 times the time period. In the presence of an endoleak channel, for all channel sizes, \bar{p}_{sac} approximates \bar{p}_{sys} . Yet, while the two are about equal in the numerical model, in the experiment, \bar{p}_{sac} is slightly lower than \bar{p}_{sys} (see Table 5.1). In addition, the systemic pressure signal amplitude or pulse pressure (Δp_{sys}) is slightly larger in the numerical model than in the experiment. The endoleak channel flow rates in the two models have similar amplitudes. Again, however, the simulated signals are smoother than the measured signals. Additionally, minor shape differences are present at the signal maximum and near the end of the time period. Positive flow rates indicating flow into the modelled aneurysm are present while p_{sys} is higher than p_{sac} . During that period, p_{sac} is increased. Outflow from the aneurysm and a decreasing p_{sac} are present while p_{sac} is higher than p_{sys} . The variations of the flow rate signals are generally in phase with the variations of p_{sys} . Both the flow rate signal amplitude and the intrasac pulse pressure (Δp_{sac}) are increased with increasing endoleak channel size. Yet, in all cases, $p_{\text{sac}}^{\text{s}}$ is decreased compared to $p_{\text{sys}}^{\text{s}}$, and $p_{\text{sac}}^{\text{d}}$ is higher than $p_{\text{sys}}^{\text{d}}$.

In the physiologic situation, the absence of endoleak yields a mean intrasac pressure \bar{p}_{sac} that equals zero for all combinations of stent-graft compliance and outflow tract resistance, while the intrasac pressure amplitude Δp_{sac} varies as a function of both these parameters (see Figures 5.6(a) and 5.6(b)). The latter is increased for

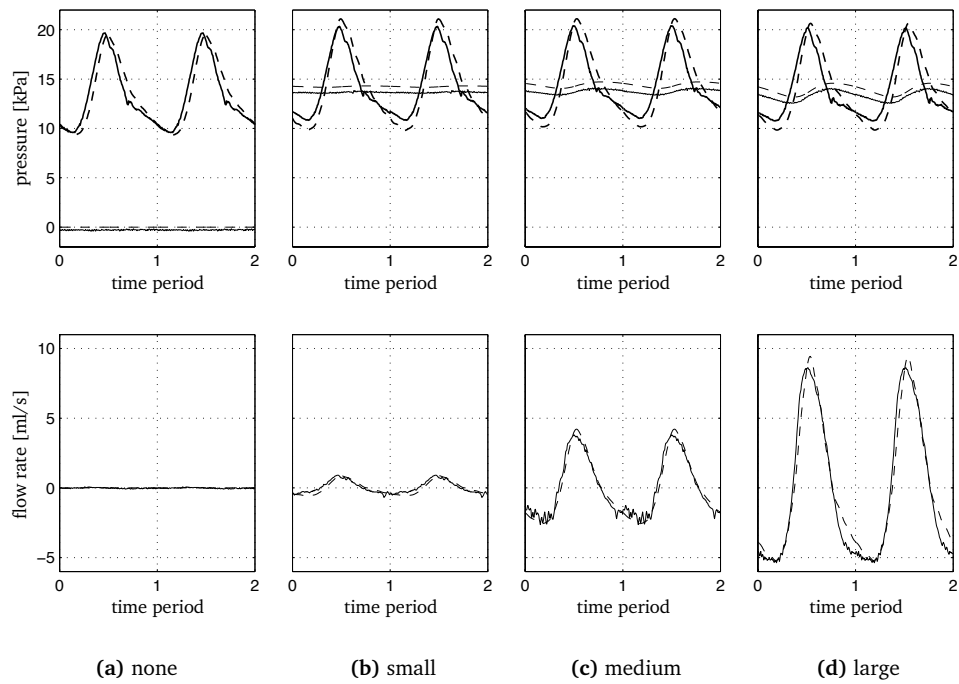


Figure 5.5: Validation of the lumped parameter model: measured (solid) and simulated (dashed) signals in the absence of an endoleak channel (a) and in the presence of small (b), medium (c), and large-sized (d) channels. Top: systemic (thick) and intrasac (thin) pressures. Bottom: endoleak channel flow rate.

increasing stent-graft compliance. At higher compliance values, it is further increased for increasing outflow tract resistance. The limiting cases of p_{sac} that are obtained at the boundaries of the parameter value intervals applied in this study are zero-pressure signals at minimal stent-graft compliance (see Figure 5.6, cases B and D), and a signal mimicking p_{sys} with a lower amplitude at maximal compliance and maximal outflow tract resistance (see Figure 5.6, case C). At maximal compliance and minimal resistance, p_{sac} has a different shape from p_{sys} , with a generally lower amplitude (see Figure 5.6, case A).

In the absence of an outflow tract, \bar{p}_{sac} is constant at a value of \bar{p}_{sys} for all combinations of endoleak resistance and stent-graft compliance, while Δp_{sac} again varies as a function of both the studied parameters (see Figures 5.7(a) and 5.7(b)). The latter is increased for both increasing stent-graft compliance and decreasing endoleak resistance. At minimal endoleak resistance, it approaches a maximal constant value. The limiting cases of p_{sac} are a signal of almost zero-amplitude at maximal endoleak resistance and minimal stent-graft compliance (see Figure 5.7, case D) and signals with an amplitude of almost Δp_{sys} at minimal endoleak resistance (see Figure 5.7, cases A and B). At maximal compliance and maximal resistance, p_{sac} has the shape of p_{sys} with a decreased amplitude (see Figure 5.7, case C).

In case of a rigid stent-graft, both \bar{p}_{sac} and Δp_{sac} are functions of both the endoleak resistance and the outflow tract resistance (see Figures 5.8(a) and 5.8(b)). The value of \bar{p}_{sac} varies between approximately zero and \bar{p}_{sys} , and is increased for both decreasing endoleak resistance and increasing outflow tract resistance. The value of Δp_{sac} varies similarly, although the increase with increasing outflow tract resistance is less prominent at higher endoleak resistance. The limiting cases of p_{sac} are a zero-pressure signal at minimal outflow tract resistance and maximal endoleak resistance (see Figure 5.8, case D) and a signal with an amplitude of almost Δp_{sys} and a mean of \bar{p}_{sys} at maximal outflow tract resistance and minimal endoleak resistance (see Figure 5.8, case A). In combination with the maximal outflow tract resistance, the maximal endoleak resistance yields a signal with a very small amplitude at a mean of about half the value of \bar{p}_{sys} (see Figure 5.8, case C). At minimal outflow tract resistance and minimal endoleak resistance, Δp_{sac} equals approximately half Δp_{sys} (see Figure 5.8, case B).

5.4 Discussion

In order to both reconcile and physically substantiate various findings of experimental endoleak studies described in literature, a computational model of an incompletely excluded AAA has been developed. Based on the arterial tree model by Westerhof *et al.* (1969), a lumped parameter model of the human aortic tree has been generated, incorporating an excluded AAA in the presence of both an endoleak channel and an outflow tract. After validation by means of an experimental setup, the model has been applied to study the effects on the intrasac pressure after EVAR of AAA of the degree of endoleak, the degree of stent-graft compliance, and the outflow tract resistance.

The experimental validation shows that the lumped parameter modelling method

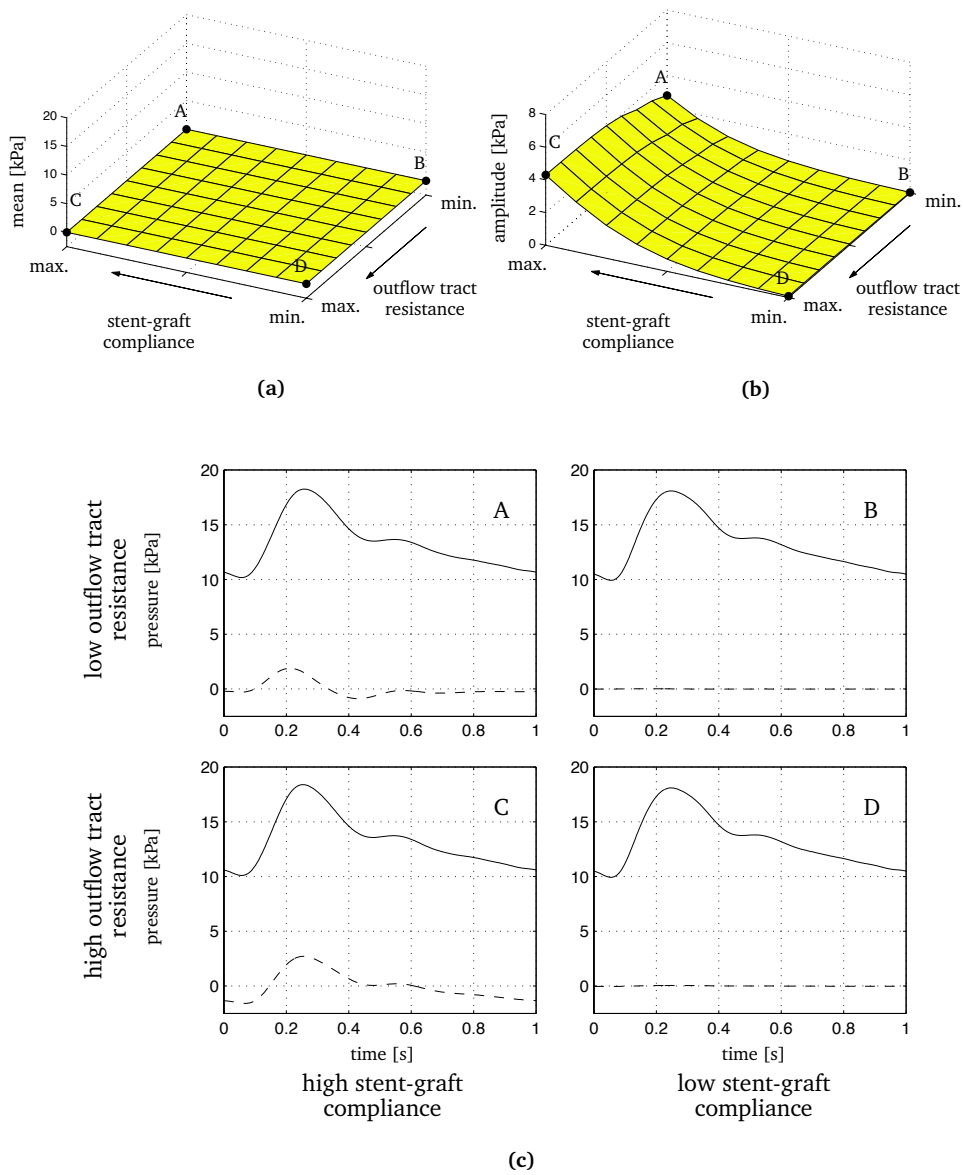


Figure 5.6: Simulated pressures in the absence of endoleak: intrasac pressure mean (a) and amplitude (b) as a function of both outflow tract resistance and stent-graft compliance, and systemic (solid) and intrasac (dashed) pressures for the limiting cases A, B, C, and D, as indicated (c).

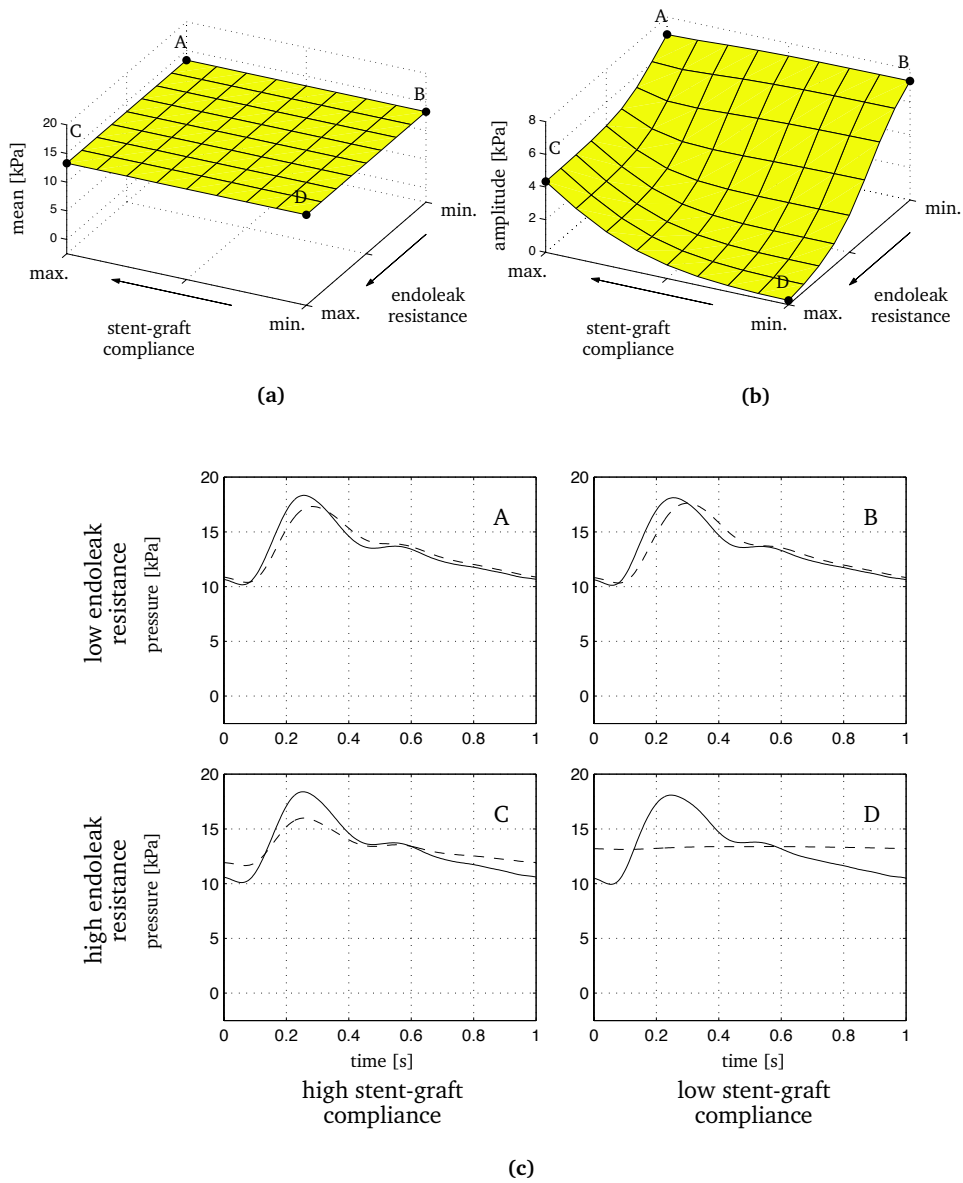


Figure 5.7: Simulated pressures in the absence of an outflow tract: intrasac pressure mean (a) and amplitude (b) as a function of both endoleak resistance and stent-graft compliance, and systemic (solid) and intrasac (dashed) pressures for the limiting cases A, B, C, and D, as indicated (c).

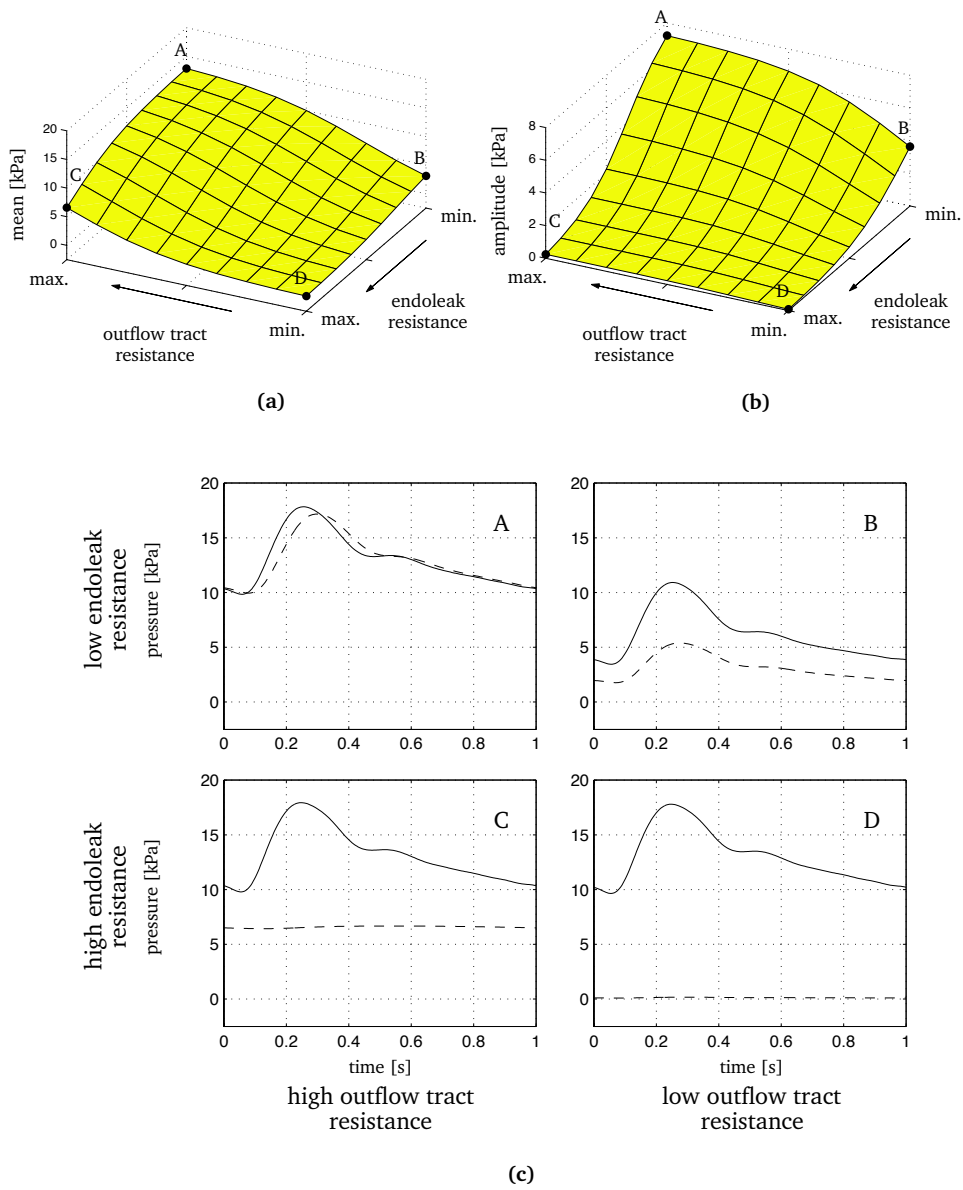


Figure 5.8: Simulated pressures in the absence of stent-graft compliance: intrasac pressure mean (a) and amplitude (b) as a function of both endoleak and outflow tract resistance, and systemic (solid) and intrasac (dashed) pressures for the limiting cases A, B, C, and D, as indicated (c).

is capable of representing the intrasac pressure variations in an incompletely excluded AAA. The intrasac mean pressure and pressure oscillations as well as the flow through the endoleak channel can be captured. It should be noted that, to obtain these results, the outflow resistance of the numerical model was determined based on the mean systemic pressure and flow measured in the experiment. Additionally, the endoleak channel resistance, the main tube compliance and the aneurysm compliance were scaled in order to match measured results. These adjustments, however, do not undermine the practical value of the model. The imposed outflow resistance can be considered as merely a boundary condition similar to the prescribed flow at the input. In this respect, the scaling of the endoleak channel resistance, main tube compliance, and aneurysm compliance seems more of an infringement. Still, this poses no problem as long as the model is used in parameter variation studies.

The differences found between the measured and simulated results in the experimental validation may indicate that for application of the model in exact simulations rather than parameter variation studies, some model properties and boundary conditions need to be optimised. For instance, the need for scaling the endoleak channel resistance may indicate that the non-linear effects that were neglected in determining its value have a considerable effect that, in that case, should still be incorporated (see, e.g., Idelchik, 1994). Further, since a non-optimal choice of filter parameters may induce amplitude and phase changes to the filtered signal, the model response may be improved by optimisation of the Butterworth filter applied to the inlet flow signal. In the current study, such amplitude changes may be the reason for the shape differences in the endoleak channel flow rates, and probable, less apparent differences in the systemic and intrasac pressures. The effect on the overall amplitudes may be limited, however, due to the scaling of the model response. Phase changes, on the other hand, cannot have been induced by the filter, since this was of the zero-phase type. Possibly, phase shifts observed in the results are due to limited spatial discretisation. Since the amplitude and phase changes observed in the current study are small, they do not invalidate the model for application in parameter variation studies. Finally, the measured difference between \bar{p}_{sac} and \bar{p}_{sys} not present in the simulation, may indicate the need for incorporating a gravitational effect. Since the mean difference is in the order of 0.65 kPa (see Table 5.1), while the height difference bridged by the endoleak channel is around 6.5 cm, the difference is suspected to be due to gravitational forces that need to be overcome during the transfer of fluid from the main tube to the aneurysm. Yet again, in parameter variational studies, the current model remains valid.

The results of the physiologic model show that by means of lumped parameter models of the human aortic tree, the effects of endoleak can be simulated in a physiologic context. It makes the model extendable to simulate experiments concerning type II endoleak, in which there is persistent flow into the aneurysm sac through collateral branches (e.g., Dayal *et al.*, 2004; Diaz *et al.*, 2004; Mousa *et al.*, 2005). In that case, by connecting the branches to other parts of the circulation, the collateral flow could be generated rather than prescribed as originating from a separate source. The current study, however, focuses on endoleak originating from the aortic lumen. In this study, neither of the endoleak resistance, outflow tract resistance, and stent-

graft compliance is based on physiologic measurements. The representing parameter values, however, are varied in such an approach, that the intrasac mean and pulse pressure values cover almost full ranges between zero and the systemic mean and pulse pressure values, respectively. This ensures that physiologic model parameter values are included in the study. Nevertheless, it should be noted that, especially towards the boundaries of the applied parameter value intervals, not all modelled situations will be realistic. See, e.g., Figure 5.8, case B, where the endoleak resistance and the outflow tract resistance both are at such low levels, that the systemic pressure cannot be sustained. Such limiting behaviour can still be helpful, however, in the understanding of the general phenomena associated with endoleak.

By combining the results of the different physiologic situations simulated, it can be concluded that the presence of endoleak leads to elevated intrasac pressure, the mean of which is mainly governed by the outflow tract resistance, while the pulse pressure is governed by both the endoleak resistance and the stent-graft compliance. In general, the effect of a higher degree of endoleak is an increased intrasac pulse pressure (see Figures 5.7(b) and 5.8(b)). The general effect of a higher degree of stent-graft compliance is a more pronounced transmission through the stent-graft to the aneurysmal sac of the systemic pulse pressure (see Figure 5.6(b)). In the absence of endoleak, a higher degree of stent-graft compliance leads to an increased intrasac pulse pressure at zero mean pressure (see Figure 5.6, case C). In the presence of endoleak it has a similar effect, in which the mean is at the level of the systemic mean pressure (see Figure 5.7, case C). The general effect of a decreased outflow tract resistance is mainly a reduction of the intrasac mean pressure in the presence of endoleak (see Figure 5.8(a)). Additionally, it may result in attenuation of the intrasac pulse pressure resulting from either the presence of endoleak (see Figure 5.8(b)) or a high degree of stent-graft compliance (see Figure 5.6(b)). Based on these observations, it seems that, in order to minimise the intrasac pressure, the most favourable situation is one of maximal resistance of a possible endoleak combined with minimal stent-graft compliance and minimal outflow tract resistance.

Based on the agreement of the current results with previous findings, it can be concluded that the lumped parameter modelling method provides a useful numerical tool for validating experimental endoleak studies. The finding that, in the presence of endoleak, \bar{p}_{sac} equals \bar{p}_{sys} (Schurink *et al.*, 2000a; Skillern *et al.*, 2002; Chong *et al.*, 2003), is consistent with the results of the current study in case there is no outflow tract. Further, the findings that the intrasac pressure pulsatility is inversely related to the endoleak channel diameter (Schurink *et al.*, 2000a; Chong *et al.*, 2003) and is obliterated by thrombosis (Schurink *et al.*, 2000a) are consistent with the current finding that Δp_{sac} is inversely related to the endoleak resistance. This finding also substantiates the findings on the reduction of $p_{\text{sac}}^{\text{s}}$ in case of thrombosed endoleak channels by Mehta *et al.* (2001). Further, the reducing effect of the presence of an outflow tract on the intrasac pressure as found by Parodi *et al.* (2001) and Chong *et al.* (2003) is consistent with the current finding that \bar{p}_{sac} and Δp_{sac} are reduced for decreased values of the outflow tract resistance. Finally, the intrasac pressure pulsatility in fully excluded aneurysms as observed by Parodi *et al.* (2001), Chong *et al.* (2003), and Mehta *et al.* (2003), is consistent with the current finding that for higher

degrees of stent-graft compliance, the systemic pulse pressure is transmitted through the stent-graft to the aneurysmal sac. Also the finding of Schurink *et al.* (1998) that the intrasac pressure is obliterated in fully excluded aneurysms is consistent with the current results, if it supposed that a relatively stiff stent-graft was applied.

Findings of previous studies that could not be confirmed may indicate that for the simulation of measurements on experimental setups, dedicated model configurations and boundary conditions are necessary. For instance, the finding of Schurink *et al.* (1998) that with endoleak in the absence of an outflow tract p_{sac}^s and \bar{p}_{sac} are decreased compared to p_{sys}^s and \bar{p}_{sys} , may indicate that the conditions applicable to the experiment were different from the conditions currently simulated. Based on the current model, it would be expected for p_{sac}^s and \bar{p}_{sac} to be equal. In case of a net mean pressure difference, the endoleak channel would be subject to a net mean flow that would not vanish until the two pressures had levelled. Similarly, an increased \bar{p}_{sac} compared to \bar{p}_{sys} as found by Parodi *et al.* (2001) could not be confirmed either. In the current model, again the resulting pressure difference would result in a net mean flow that would not vanish until the two values had levelled. Finally, the observation of p_{sac}^d and p_{sac}^s values both higher than p_{sys}^s as observed by Mehta *et al.* (2003) remains unconfirmed. Based on the current model, due to leakage back into the main circulation, all intrasac pressures would be expected to level at least somewhere below p_{sys}^s .

In the interpretation of the results of this study, it should be noted that there may be additional factors affecting the aneurysm intrasac pressure that were not studied or incorporated in the numerical model. One of these is the compliance of the aneurysm itself, which in turn is influenced by the aneurysm volume and its wall thickness. Both these factors have experimentally been shown to affect the intrasac pressure increase, in which an increased volume and a decreased wall thickness each have a damping effect (Gawenda *et al.*, 2003b, 2004). Further, it is not unlikely that the compliance is also affected by the presence of thrombus inside the aneurysm, by means of either an influence on the amount of fluid that is contained, or a contribution to the total stiffness. Additionally, the presence of thrombus may influence the intrasac pressure increase by affecting the resistance to intrasac fluid flow. Although the presence of thrombus itself does not necessarily reduce the pressure acting on the aneurysm wall (Schurink *et al.*, 2000b), a resulting decreased intrasac flow may induce complete aneurysm thrombosis, which is related to a decrease of both the intrasac pressure pulsatility and the intrasac mean pressure (Schurink *et al.*, 2000a). Finally, the degree of the intrasac pressure decrease due to the presence of the outflow tract will be dependent on the tract's reference pressure. In a physiologic situation this will be the pressure in the connected vascular bed, and a high pressure may even lead to type II endoleakage back into the aneurysm. Although Chong *et al.* (2003) for a certain degree of flow through the tract observed no influence of the outflow pressure, this will be different if the tract flow is left to be influenced by this pressure by means of a constant tract resistance.

5.5 Conclusion

The lumped parameter modelling method is capable of representing the intrasac pressure variations in an incompletely excluded AAA. By means of lumped parameter models of the human aortic tree, the effects of endoleak can be simulated in a physiologic context. It is concluded that the presence of endoleak leads to elevated intrasac pressure, the mean of which is mainly governed by the outflow tract resistance, while the pulse pressure is governed by both the endoleak resistance and the stent-graft compliance. Based on the agreement of the current results with previous findings, it is further concluded that the lumped parameter modelling method provides a useful numerical tool for validating experimental endoleak studies.

Chapter 6

General discussion

6.1 Introductory remarks

The general objectives of this thesis were (1) to provide computational tools for improved decision making in the treatment of AAA and (2) to provide insight into the level of detail required by such models. These objectives were pursued by application of computational FSI modelling techniques. The objectives were founded on the assumption that computational models of FSI in AAA could help to better predict AAA development and rupture before treatment as well as to assess the effects of endoleak on the risk of rupture after EVAR. With respect to the situation before treatment, this thesis builds on previous studies using patient-specific models of solely the wall stress (Raghavan and Vorp, 2000b; Thubrikar *et al.*, 2001b; Fillinger *et al.*, 2002; Wang *et al.*, 2002; Venkatasubramaniam *et al.*, 2004) and on studies also including fluid-dynamic effects (Di Martino *et al.*, 2001; Leung *et al.*, 2006; Papaharilaou *et al.*, 2007; Scotti and Finol, 2007). With respect to the effects of endoleak on the risk of rupture after EVAR, this thesis builds on previous findings on the relation between endoleak and the aneurysm intrasac pressure both from experimental and animal studies (Schurink *et al.*, 2000a; Mehta *et al.*, 2001, 2003; Parodi *et al.*, 2001; Skillern *et al.*, 2002; Chong *et al.*, 2003; Gawenda *et al.*, 2003a) and a small number of numerical studies (Li and Kleinstreuer, 2005a,b, 2006). The studies described in the different chapters of this thesis were motivated by specific issues raised by the results of these previous studies and/or by their applied methods.

6.2 Study results

Although the behaviour of the AAA wall inherently is influenced by the behaviour of the comprised blood, at the time of writing, previously published models for patient-specific assessment of the wall stress predominantly had not included fluid-dynamic effects. In order to facilitate the incorporation of FSI in the assessment of the wall

stress, in Chapter 2, a method for generating patient-specific hexahedral finite element meshes of the AAA lumen and wall was presented. The applicability of the meshes was illustrated by simulations of the wall stress, blood velocity distribution and WSS in a characteristic AAA. It was concluded that the presented method yields a flexible, semi-automated approach for generating patient-specific hexahedral meshes of the AAA lumen and wall with pre-defined element distributions. The combined fluid-solid mesh allows for simulations of AAA blood dynamics and AAA wall mechanics and the interaction between the two.

Furthermore, in previous patient-specific computational models of FSI in AAA, the initial wall stress resulting from the diastolic pressure load had not been incorporated. To investigate the importance of incorporating the initial stress, in Chapter 3, an FSI simulation of an idealised AAA was performed both in the presence and in the absence of initial stress. The two cases were compared by considering the differences in wall deformation, the wall stress distribution, the velocity distribution, and WSS. Additionally, by varying the wall thickness and considering a rigid wall case, the effects of the wall distensibility were studied. It was concluded that neglect of the initial wall stress leads to an overestimation of the wall deformation, overall stress level, and peak wall stress, and promotes a more smooth stress distribution. It further leads to an underestimation of the recirculation inside the aneurysm, and an underestimation of the WSS. Incorporating the initial stress, however, mostly is important for accurate modelling of the wall stress. The WSS pattern in the presence of initial stress can be well approximated using a rigid geometry.

For the simulation of endoleak, previously, in a small number of studies, numerical models had been developed based on coupled FSI. Although such models can provide useful information on the fluid dynamics and structural deformations in aneurysms after EVAR, they may computationally be too expensive if one is solely interested in the effects of endoleak on the risk of aneurysm rupture. To assess the value of computationally more efficient lumped parameter models, in Chapter 4, a lumped parameter-based computational model of an incompletely excluded AAA was developed as well as one based on coupled FSI. Both models were used to study the aneurysm intrasac pressure as a function of the degree of endoleak and the stent-graft compliance. Based on the agreement of the results of the two models it was concluded that the lumped parameter modelling method provides a useful alternative to coupled FSI for modelling the aneurysm intrasac pressure in the presence of endoleak and to give a pressure boundary condition for solid stress analyses to predict the risk of aneurysm rupture after EVAR.

The causes and effects of endoleak, however, had mainly been investigated in experimental studies. To both reconcile and physically substantiate various experimental findings, in Chapter 5, after experimental validation, a lumped parameter model of an incompletely excluded AAA was applied to study the effects on the intrasac pressure of the degree of endoleak, the degree of stent-graft compliance, and the resistance of a possible outflow tract in a physiologic context. It was concluded that the presence of endoleak leads to elevated intrasac pressure, the mean of which is mainly governed by the outflow tract resistance, while the pulse pressure is governed by both the endoleak resistance and the stent-graft compliance. Based on the

agreement of the results with previous findings, it was further concluded that the lumped parameter modelling method provides a useful numerical tool for validating experimental endoleak studies.

6.3 General conclusions and future perspective

In summary, the studies described in this thesis covered several aspects of FSI in AAA. In Chapters 2 and 3, the situation before surgical intervention was studied. In Chapters 4 and 5, the focus was on the effects of endoleak occurring after EVAR. The different studies were further distinguished by the type of computational modelling that was applied. The first two studies were based on the modelling using finite element methods. In the last two studies, the aim was to describe different phenomena using lumped parameters. As a result, several aspects of the computational modelling methods have been considered. The conclusions drawn in the different studies therefore covered a range of subjects.

With respect to the general objective of this thesis, the first part, regarding the development of computational tools for improved decision making in AAA, was addressed in Chapters 2, 4, and 5. The main result of Chapter 2 was a developed semi-automated method for generating patient-specific hexahedral meshes of the AAA lumen and wall. The meshes could be applied in FSI simulations to compute mechanical quantities that could be included in clinical trials in search of risk factors for AAA rupture, and to study the role of blood-wall interaction in processes related to AAA formation such as wall adaptation and thrombus formation. In Chapters 4 and 5 a lumped parameter model of endoleak was developed. This model could be applied in the assessment of post-operative rupture risk due to endoleak by providing a boundary condition for 3D wall stress simulations.

The second part of the general objective, to provide insight into the level of detail required by the above computational models, was addressed in Chapters 3, 4, and 5. In Chapter 3 it was found that incorporation of the initial stress has significant influence on the results of AAA wall stress simulations, and additional effects on the WSS pattern in simulations based on FSI modelling techniques. As a result, it can be concluded that the initial stress should be included in both wall stress simulations and FSI simulations using a compliant wall. However, based on the resemblance of the WSS pattern in the presence of the initial stress with that in a rigid geometry, it can also be concluded that for simulation of the WSS in AAA, the compliance of the wall needs not be incorporated. With respect to the endoleak models, based on the resemblance of the lumped parameter model results with the results of the FSI simulation in Chapter 4 and with the experimental measurements in Chapter 5, it can be concluded that for the prediction of the AAA intrasac pressure in the presence of endoleak, a full 3D FSI simulation is not necessary.

Currently, the results and conclusions of this thesis are mainly of importance within the scope of previous and future studies aimed at better understanding the development and pathogenesis of AAA and significance of endoleak after EVAR. In this respect, attention should be paid to the framework in which the different conclusions

were obtained. For extrapolation to other situations, extensions and alterations of the developed models may be necessary. In addition, the accuracy of the results computed using these models could possibly benefit from the incorporation of increased degrees of detail. For instance, the patient-specific model of FSI in AAA developed in Chapter 2 could be extended with a thrombus model, and the wall thickness and wall mechanical properties could be spatially varied to account for calcifications and other wall property variations. The finite element based FSI models in Chapters 3 and 4 could benefit from similar alterations and from incorporation of more realistic geometries. For a detailed comparison with lumped parameters models as presented in Chapters 4, the latter, however, should also be altered to account for the new features. Such adjustments, however, are mainly important with regard to quantitative studies of FSI in AAA and endoleak after EVAR in specific situations. In the search for statistical indicators of rupture risk, the comparison of different modelling methods, and parameter sensitivity studies, a qualitative approach as applied in several of the studies currently presented is sufficient.

For application of the developed models in clinical practice, additional model developments are required and the added value of the simulated quantities in clinical decision making needs to be further demonstrated. In general, computational modelling of cardiovascular problems is believed to be a useful tool in a clinical setting if it provides information of interest that could not be obtained by other means without too much difficulty or harm to the patient. Clinical guidelines based on such information, however, can only be determined after extensive validation of the predictive value of the computed quantities in focussed clinical trials. Research on the wall stress as a possible indicator of rupture risk is believed to enter this stage within several years, after completion of continued improvements to constitutive modelling, imaging, image segmentation, and 3D reconstruction techniques, and after completion of rigorous retrospective and prospective validation trials (Vorp, 2007). With respect to the blood velocity distribution and WSS it seems reasonable to believe that for the time being research will continue on a more academic level. This is partly due to lack of a clear connection with acute rupture, and partly due to existing possibilities for measuring the velocity distribution on a patient-specific basis using magnetic resonance imaging and ultrasound. Simulation of these parameters becomes indispensable, however, if computational models such as those developed in this thesis are to be incorporated in tools for simulating the outcome of surgical procedures. For the moment, simulations of the intrasac pressure after EVAR will also remain the subject of more fundamental research. On a patient-specific basis, this pressure can also be measured using implantable sensors. By helping to better understand the causes and effects of endoleak, however, the simulations of the effects of endoleak on the intrasac pressure as presented in this thesis can still indirectly contribute to improving the outcome of endovascular treatment.

On a more general note, it can be concluded that the incorporation of FSI in computational tools for decision making in the treatment of AAA mostly is important for simulating the effects of endoleak after EVAR. Based on the demonstrated possibility for simulating the WSS in the presence of initial wall stress using a rigid wall model, with regard to the situation before treatment, FSI needs not be modelled explicitly.

However, as demonstrated, by application of a lumped parameter model, explicit modelling of FSI can also be omitted from simulations of endoleak. With these findings, this thesis provides the foundation for a simplification of the decision making tools being developed, that is expected to positively influence their impact in clinical practice. The developed method for patient-specific mesh generation of the AAA lumen and wall is as useful a tool in uncoupled simulations of the AAA wall stress, WSS, and other quantities of interest as in simulations with incorporated FSI.

References

- Baum, R. A., Carpenter, J. P., Cope, C., Golden, M. A., Velazquez, O. C., Neschis, D. G., Mitchell, M. E., Barker, C. F., and Fairman, R. M. (2001). Aneurysm sac pressure measurements after endovascular repair of abdominal aortic aneurysms. *J Vasc Surg*, **33**(1), 32–41.
- Bird, R. B., Stewart, W. E., and Lightfoot, E. N. (1960). *Transport Phenomena*. John Wiley and Sons, Inc., New York.
- Blankensteijn, J. D., de Jong, S. E. C. A., Prinssen, M., van der Ham, A. C., Buth, J., van Sterkenburg, S. M. M., Verhagen, H. J. M., Buskens, E., and Grobbee, D. E. (2005). Two-year outcomes after conventional or endovascular repair of abdominal aortic aneurysms. *N Engl J Med*, **352**(23), 2398–2405. Clinical Trial.
- Bluestein, D., Niu, L., Schoepfoerster, R. T., and Dewanjee, M. K. (1996). Steady flow in an aneurysm model: correlation between fluid dynamics and blood platelet deposition. *J Biomech Eng*, **118**(3), 280–286.
- Borghi, A., Wood, N., Mohiaddin, R., and Xu, X. (2008). Fluid-solid interaction simulation of flow and stress pattern in thoracoabdominal aneurysms: A patient-specific study. *J Fluid Struct*, **24**(2), 270–280.
- Breeuwer, M., Götte, U., Hoogeveen, R., Wolters, B. J. B. M., de Putter, S., v.d. Bosch, H., Buth, J., Rouet, J.-M., and Laffargue, F. (2004). Assessment of the rupture risk of abdominal aortic aneurysms by patient-specific hemodynamic modeling – initial results. In *Proceedings of the 18th International Congress and Exhibition on Computer Assisted Radiology and Surgery*, pages 1090–1095. Elsevier Science.
- Buth, J., Harris, P. L., Van Marrewijk, C., and Fransen, G. (2003). Endoleaks during follow-up after endovascular repair of abdominal aortic aneurysm. Are they all dangerous? *J Cardiovasc Surg*, **44**(4), 559–566.
- Choke, E., Cockerill, G., Wilson, W. R. W., Sayed, S., Dawson, J., Loftus, I., and Thompson, M. M. (2005). A review of biological factors implicated in abdominal aortic aneurysm rupture. *Eur J Vasc Endovasc Surg*, **30**(3), 227–244.
- Chong, C. K., How, T. V., Gilling-Smith, G. L., and Harris, P. L. (2003). Modeling endoleaks and collateral reperfusion following endovascular AAA exclusion. *J Endovasc Ther*, **10**(3), 424–432.

- Cronenwett, J. L. (1996). Variables that affect the expansion rate and rupture of abdominal aortic aneurysms. *Ann NY Acad Sci*, **800**(56-6), 56–67.
- Dayal, R., Mousa, A., Bernheim, J., Hollenbeck, S., Henderson, P., Prince, M., Gordon, R., Badimon, J., Fuster, V., Marin, M. L., Craig Kent, K., and Faries, P. L. (2004). Characterization of retrograde collateral (type II) endoleak using a new canine model. *J Vasc Surg*, **40**(5), 985–994.
- De Putter, S., Wolters, B. J. B. M., Rutten, M. C. M., Breeuwer, M., Gerritsen, F. A., and Van de Vosse, F. N. (2007). Patient-specific initial wall stress in abdominal aortic aneurysms with a backward incremental method. *J Biomech*, **40**(5), 1081–90.
- Di Martino, E., Mantero, S., Inzoli, F., Melissano, G., Astore, D., Chiesa, R., and Fumero, R. (1998). Biomechanics of abdominal aortic aneurysm in the presence of endoluminal thrombus: experimental characterisation and structural static computational analysis. *Eur J Vasc Endovasc Surg*, **15**(4), 290–299.
- Di Martino, E. S. and Vorp, D. A. (2003). Effect of variation in intraluminal thrombus constitutive properties on abdominal aortic aneurysm wall stress. *Ann Biomed Eng*, **31**(7), 804–809.
- Di Martino, E. S., Guadagni, G., Fumero, A., Ballerini, G., Spirito, R., Biglioli, P., and Redaelli, A. (2001). Fluid-structure interaction within realistic three-dimensional models of the aneurysmatic aorta as a guidance to assess the risk of rupture of the aneurysm. *Med Eng Phys*, **23**(9), 647–655.
- Dias, N. V., Ivancev, K., Malina, M., Resch, T., Lindblad, B., and Sonesson, B. (2004). Intra-aneurysm sac pressure measurements after endovascular aneurysm repair: differences between shrinking, unchanged, and expanding aneurysms with and without endoleaks. *J Vasc Surg*, **39**(6), 1229–1235.
- Diaz, S., Uzieblo, M. R., Desai, K. M., Talcott, M. R., Bae, K. T., Geraghty, P. J., Parodi, J. C., Sicard, G. A., Sanchez, L. A., and Choi, E. T. (2004). Type II endoleak in porcine model of abdominal aortic aneurysm. *J Vasc Surg*, **40**(2), 339–344.
- Dubost, C., Allary, M., and Oeconomos, N. (1952). Resection of an aneurysm of the abdominal aorta: reestablishment of the continuity by a preserved human arterial graft, with result after five months. *AMA Arch Surg*, **64**(3), 405–408.
- Egelhoff, C. J., Budwig, R. S., Elger, D. F., Khraishi, T. A., and Johansen, K. H. (1999). Model studies of the flow in abdominal aortic aneurysms during resting and exercise conditions. *J Biomech*, **32**(12), 1319–1329.
- Eilers, P. H. C. (2003). A perfect smoother. *Anal Chem*, **75**(14), 3631–3636.
- Ellozy, S. H., Carroccio, A., Lookstein, R. A., Minor, M. E., Sheahan, C. M., Juta, J., Cha, A., Valenzuela, R., Addis, M. D., Jacobs, T. S., Teodorescu, V. J., and Marin, M. L. (2004). First experience in human beings with a permanently implantable intrasac pressure transducer for monitoring endovascular repair of abdominal aortic aneurysms. *J Vasc Surg*, **40**(3), 405–412.

- Fillinger, M. F., Raghavan, M. L., Marra, S. P., Cronenwett, J. L., and Kennedy, F. E. (2002). In vivo analysis of mechanical wall stress and abdominal aortic aneurysm rupture risk. *J Vasc Surg*, **36**(3), 589–597.
- Fillinger, M. F., Marra, S. P., Raghavan, M. L., and Kennedy, F. E. (2003). Prediction of rupture risk in abdominal aortic aneurysm during observation: wall stress versus diameter. *J Vasc Surg*, **37**(4), 724–732.
- Fillinger, M. F., Racusin, J., Baker, R. K., Cronenwett, J. L., Teutelink, A., Schermerhorn, M. L., Zwolak, R. M., Powell, R. J., Walsh, D. B., and Rzucidlo, E. M. (2004). Anatomic characteristics of ruptured abdominal aortic aneurysm on conventional CT scans: implications for rupture risk. *J Vasc Surg*, **39**(6), 1243–1252.
- Finol, E. A., Keyhani, K., and Amon, C. H. (2003). The effect of asymmetry in abdominal aortic aneurysms under physiologically realistic pulsatile flow conditions. *J Biomech Eng*, **125**(2), 207–217.
- Formaggia, L., Lamponi, D., and Quarteroni, A. (2003). One-dimensional models for blood flow in arteries. *J Eng Math*, **47**(3-4), 251–276.
- Fritsch, F. N. and Carlson, R. E. (1980). Monotone piecewise cubic interpolation. *SIAM J Numer Anal*, **17**(2), 238–246.
- Gawenda, M., Jaschke, G., Winter, S., Wassmer, G., and Brunkwall, J. (2003a). Endotension as a result of pressure transmission through the graft following endovascular aneurysm repair—an in vitro study. *Eur J Vasc Endovasc Surg*, **26**(5), 501–505.
- Gawenda, M., Winter, S., Jaschke, G., Wassmer, G., and Brunkwall, J. (2003b). Endotension is influenced by aneurysm volume: experimental findings. *J Endovasc Ther*, **10**(6), 1091–1096.
- Gawenda, M., Knez, P., Winter, S., Jaschke, G., Wassmer, G., Schmitz-Rixen, T., and Brunkwall, J. (2004). Endotension is influenced by wall compliance in a latex aneurysm model. *Eur J Vasc Endovasc Surg*, **27**(1), 45–50.
- Gerard, O., Billon, A. C., Rouet, J.-M., Jacob, M., Fradkin, M., and Allouche, C. (2002). Efficient model-based quantification of left ventricular function in 3-D echocardiography. *IEEE Trans Med Imaging*, **21**(9), 1059–1068.
- Gijssen, F. J. H., Allanic, E., van de Vosse, F. N., and Janssen, J. D. (1999). The influence of the non-Newtonian properties of blood on the flow in large arteries: unsteady flow in a 90 degrees curved tube. *J Biomech*, **32**(7), 705–713.
- Greenhalgh, R. M., Brown, L. C., Kwong, G. P. S., Powell, J. T., and Thompson, S. G. (2004). Comparison of endovascular aneurysm repair with open repair in patients with abdominal aortic aneurysm (EVAR trial 1), 30-day operative mortality results: randomised controlled trial. *Lancet*, **364**(9437), 843–848.

- Hatakeyama, T., Shigematsu, H., and Muto, T. (2001). Risk factors for rupture of abdominal aortic aneurysms based on three-dimensional study. *J Vasc Surg*, **33**(3), 453–461.
- Hinchliffe, R. J. and Hopkinson, B. R. (2003). Current concepts and controversies in endovascular repair of abdominal aortic aneurysms. *J Cardiovasc Surg*, **44**(4), 481–502.
- Hua, J. and Mower, W. R. (2001). Simple geometric characteristics fail to reliably predict abdominal aortic aneurysm wall stresses. *J Vasc Surg*, **34**(2), 308–315.
- Idelchik, I. E. (1994). *Handbook of hydraulic resistance*. CRC Press, Inc., Boca Raton, FL.
- Inzoli, F., Boschetti, F., Zappa, M., Longo, T., and Fumero, R. (1993). Biomechanical factors in abdominal aortic aneurysm rupture. *Eur J Vascular Surg*, **7**(6), 667–674.
- Johnston, K., Rutherford, R., Tilson, M., Shah, D., Hollier, L., and Stanley, J. (1991). Suggested standards for reporting on arterial aneurysms. Subcommittee on Reporting Standards for Arterial Aneurysms, Ad Hoc Committee on Reporting Standards, Society for Vascular Surgery and North American Chapter, International Society for Cardiovascular Surgery. *J Vasc Surg*, **13**, 452–458.
- Karkos, C. D., Mukhopadhyay, U., Papakostas, I., Ghosh, J., Thomson, G. J., and Hughes, R. (2000). Abdominal aortic aneurysm: the role of clinical examination and opportunistic detection. *Eur J Vasc Endovasc Surg*, **19**(3), 299–303.
- Kazi, M., Thyberg, J., Religa, P., Roy, J., Eriksson, P., Hedin, U., and Swedenborg, J. (2003). Influence of intraluminal thrombus on structural and cellular composition of abdominal aortic aneurysm wall. *J Vasc Surg*, **38**, 1283–1292.
- Lakatta, E. G. (2002). Age-associated cardiovascular changes in health: impact on cardiovascular disease in older persons. *Heart Fail Rev*, **7**(1), 29–49.
- Lasheras, J. C. (2007). The biomechanics of arterial aneurysms. *Annu Rev Fluid Mech*, **39**, 293–319.
- Lederle, F. A., Wilson, S. E., Johnson, G. R., Reinke, D. B., Littooy, F. N., Acher, C. W., Ballard, D. J., Messina, L. M., Gordon, I. L., Chute, E. P., Krupski, W. C., Busuttill, S. J., Barone, G. W., Sparks, S., Graham, L. M., Rapp, J. H., Makaroun, M. S., Moneta, G. L., Cambria, R. A., Makhoul, R. G., Eton, D., Ansel, H. J., Freischlag, J. A., and Bandyk, D. (2002a). Immediate repair compared with surveillance of small abdominal aortic aneurysms. *N Engl J Med*, **346**(19), 1437–1444.
- Lederle, F. A., Johnson, G. R., Wilson, S. E., Ballard, D. J., Jordan, W. D., Blebea, J., Littooy, F. N., Freischlag, J. A., Bandyk, D., Rapp, J. H., and Salam, A. A. (2002b). Rupture rate of large abdominal aortic aneurysms in patients refusing or unfit for elective repair. *JAMA*, **287**(22), 2968–72.

- Leung, J., Wright, A., Cheshire, N., Crane, J., Thom, S., Hughes, A., and Xu, Y. (2006). Fluid structure interaction of patient specific abdominal aortic aneurysms: a comparison with solid stress models. *Biomed Eng Online*, **5**, 33.
- Leurs, L. J., Buth, J., and Laheij, R. J. F. (2007). Long-term results of endovascular abdominal aortic aneurysm treatment with the first generation of commercially available stent grafts. *Arch Surg*, **142**(1), 33–41.
- Li, Z. and Kleinstreuer, C. (2005a). Blood flow and structure interactions in a stented abdominal aortic aneurysm model. *Med Eng Phys*, **27**(5), 369–382.
- Li, Z. and Kleinstreuer, C. (2005b). Fluid-structure interaction effects on sac-blood pressure and wall stress in a stented aneurysm. *J Biomech Eng*, **127**(4), 662–671.
- Li, Z. and Kleinstreuer, C. (2006). Effects of major endoleaks on a stented abdominal aortic aneurysm. *J Biomech Eng*, **128**(1), 59–68.
- Lu, J., Zhou, X., and Raghavan, M. L. (2007a). Computational method of inverse elastostatics for anisotropic hyperelastic solids. *Int J Numer Meth Eng*, **69**(6), 1239–1261.
- Lu, J., Zhou, X., and Raghavan, M. (2007b). Inverse elastostatic stress analysis in pre-deformed biological structures: Demonstration using abdominal aortic aneurysms. *J Biomech*, **40**, 693–696.
- MacSweeney, S. T. R., Powell, J. T., and Greenhalgh, R. M. (1994). Pathogenesis of abdominal aortic aneurysm. *Brit J Surg*, **81**(7), 935–941.
- McArdle, W. D., Katch, F. I., and Katch, V. L. (1996). *Exercise physiology: energy, nutrition, and human performance*. Williams and Wilkins, Baltimore, 4th edition.
- Mehta, M., Ohki, T., Veith, F. J., and Lipsitz, E. C. (2001). All sealed endoleaks are not the same: a treatment strategy based on an ex-vivo analysis. *Eur J Vasc Endovasc Surg*, **21**(6), 541–544.
- Mehta, M., Veith, F. J., Ohki, T., Lipsitz, E. C., Cayne, N. S., and Darling III, R. C. (2003). Significance of endotension, endoleak, and aneurysm pulsatility after endovascular repair. *J Vasc Surg*, **37**(4), 842–846.
- Milner, R., Verhagen, H. J. M., Prinssen, M., and Blankensteijn, J. D. (2004). Non-invasive intrasac pressure measurement and the influence of type 2 and type 3 endoleaks in an animal model of abdominal aortic aneurysm. *Vascular*, **12**(2), 99–105.
- Milnor, W. R. (1989). *Hemodynamics*. Williams and Wilkins, Baltimore, 2nd edition.
- Mousa, A., Dayal, R., Bernheim, J., Henderson, P., Hollenbeck, S., Trocciola, S., Prince, M., Gordon, R., Badimon, J., Fuster, V., Marin, M. L., Kent, K. C., and Faries, P. L. (2005). A canine model to study the significance and hemodynamics of type II endoleaks. *J Surg Res*, **123**(2), 275–283.

- Mower, W. R., Quiñones, W. J., and Gambhir, S. S. (1997). Effect of intraluminal thrombus on abdominal aortic aneurysm wall stress. *J Vasc Surg*, **26**(4), 602–608.
- Olufsen, M. S., Peskin, C. S., Kim, W. Y., Pedersen, E. M., Nadim, A., and Larsen, J. (2000). Numerical simulation and experimental validation of blood flow in arteries with structured-tree outflow conditions. *Ann Biomed Eng*, **28**(11), 1281–1299.
- Papaharilaou, Y., Ekaterinaris, J., Manousaki, E., and Katsamouris, A. (2007). A decoupled fluid structure approach for estimating wall stress in abdominal aortic aneurysms. *J Biomech*, **40**, 367–377.
- Parodi, J. C., Palmaz, J. C., and Barone, H. D. (1991). Transfemoral intraluminal graft implantation for abdominal aortic aneurysms. *Ann Vasc Surg*, **5**(6), 491–499. Case Reports.
- Parodi, J. C., Berguer, R., Ferreira, L. M., La Mura, R., and Schermerhorn, M. L. (2001). Intra-aneurysmal pressure after incomplete endovascular exclusion. *J Vasc Surg*, **34**(5), 909–914.
- Perktold, K. and Rappitsch, G. (1995). Computer simulation of local blood flow and vessel mechanics in a compliant carotid artery bifurcation model. *J Biomech*, **28**, 845–856.
- Pleumeekers, H. J. C. M., Hoes, A. W., van der Does, E., Van Urk, H., and Grobbee, D. E. (1994). Epidemiology of abdominal aortic aneurysms. *Eur J Vascular Surg*, **8**(2), 119–128.
- Raghavan, M. L. and Vorp, D. A. (2000a). Toward a biomechanical tool to evaluate rupture potential of abdominal aortic aneurysm: identification of a finite strain constitutive model and evaluation of its applicability. *J Biomech*, **33**(4), 475–482.
- Raghavan, M. L. and Vorp, D. A. (2000b). Wall stress distribution on three-dimensionally reconstructed models of human abdominal aortic aneurysm. *J Vasc Surg*, **31**(4), 760–769.
- Raghavan, M. L., Ma, B., and Fillinger, M. F. (2006). Non-invasive determination of zero-pressure geometry of arterial aneurysms. *Ann Biomed Eng*, **34**(9), 1414–1419.
- Rutten, M. (1998). *Fluid-solid interaction in large arteries*. Ph.D. thesis, Eindhoven University of Technology.
- Sacks, M. S., Vorp, D. A., Raghavan, M. L., Federle, M. P., and Webster, M. W. (1999). In vivo three-dimensional surface geometry of abdominal aortic aneurysms. *Ann Biomed Eng*, **27**(4), 469–479.
- Salsac, A., Sparks, S., Chomaz, J., and Lasheras, J. (2006). Evolution of the wall shear stresses during the progressive enlargement of symmetric abdominal aortic aneurysms. *J Fluid Mech*, **560**, 19–51.

- Schurink, G. W., Aarts, N. J., Van Baalen, J. M., Kool, L. J., and Van Bockel, J. H. (2000a). Experimental study of the influence of endoleak size on pressure in the aneurysm sac and the consequences of thrombosis. *Br J Surg*, **87**(1), 71–78.
- Schurink, G. W., van Baalen, J. M., Visser, M. J., and van Bockel, J. H. (2000b). Thrombus within an aortic aneurysm does not reduce pressure on the aneurysmal wall. *J Vasc Surg*, **31**(3), 501–506.
- Schurink, G. W. H., Aarts, N. J. M., Wilde, J., van Baalen, J. M., Chuter, T. A. M., Schultze Kool, L. J., and van Bockel, J. H. (1998). Endoleakage after stent-graft treatment of abdominal aneurysm: implications on pressure and imaging—an in vitro study. *J Vasc Surg*, **28**(2), 234–241.
- Scotti, C. M. and Finol, E. A. (2007). Compliant biomechanics of abdominal aortic aneurysms: A fluid–structure interaction study. *Comput Struct*, **85**, 1097–1113.
- Sho, E., Nanjo, H., Sho, M., Kobayashi, M., Komatsu, M., Kawamura, K., Xu, C., Zarins, C. K., and Masuda, H. (2004). Arterial enlargement, tortuosity, and intimal thickening in response to sequential exposure to high and low wall shear stress. *J Vasc Surg*, **39**(3), 601–612.
- Singh, K., Bønaa, K. H., Jacobsen, B. K., Bjørk, L., and Solberg, S. (2001). Prevalence of and risk factors for abdominal aortic aneurysms in a population-based study: The Tromsø study. *Am J Epidemiol*, **154**(3), 236–244.
- Skillern, C. S., Stevens, S. L., Piercy, K. T., Donnell, R. L., Freeman, M. B., and Goldman, M. H. (2002). Endotension in an experimental aneurysm model. *J Vasc Surg*, **36**(4), 814–817.
- Speelman, L., Bohra, A., Bosboom, E., Schurink, G., Van de Vosse, F., Makaorun, M., and Vorp, D. (2007). Effects of wall calcifications in patient-specific wall stress analyses of abdominal aortic aneurysms. *J Biomech Eng*, **129**, 105–109.
- Stergiopoulos, N., Meister, J. J., and Westerhof, N. (1994). Simple and accurate way for estimating total and segmental arterial compliance: the pulse pressure method. *Ann Biomed Eng*, **22**(4), 392–397.
- Stergiopoulos, N., Westerhof, B. E., and Westerhof, N. (1999). Total arterial inertance as the fourth element of the windkessel model. *Am J Physiol*, **276**(1 Pt 2), 81–88.
- Stringfellow, M. M., Lawrence, P. F., and Stringfellow, R. G. (1987). The influence of aorta-aneurysm geometry upon stress in the aneurysm wall. *J Surg Res*, **42**(4), 425–433.
- Szilagyi, D. E., Elliott, J. P., and Smith, R. F. (1972). Clinical fate of the patient with asymptomatic abdominal aortic aneurysm and unfit for surgical treatment. *Arch Surg*, **104**(4), 600–606.

- Taubin, G. (1995). A signal processing approach to fair surface design. In *Proceedings of the 22nd Annual Conference on Computer Graphics and Interactive Techniques*, pages 351–358. ACM Press.
- Thubrikar, M. J., Labrosse, M., Robicsek, F., Al-Soudi, J., and Fowler, B. (2001a). Mechanical properties of abdominal aortic aneurysm wall. *J Med Eng Technol*, **25**(4), 133–142.
- Thubrikar, M. J., Al-Soudi, J., and Robicsek, F. (2001b). Wall stress studies of abdominal aortic aneurysm in a clinical model. *Ann Vasc Surg*, **15**(3), 355–366.
- Thurston, G. B. (1979). Rheological parameters for the viscosity, viscoelasticity and thixotropy of blood. *Biorheology*, **16**(3), 149–162.
- Torii, R., Oshima, M., Kobayashi, T., Takagi, K., and Tezduyar, T. E. (2007). Influence of wall elasticity in patient-specific hemodynamic simulations. *Comput Fluids*, **36**, 160–168.
- Truijers, M., Pol, J., Schultzekool, L., Van Sterkenburg, S., Fillinger, M., and Blankensteijn, J. (2007). Wall stress analysis in small asymptomatic, symptomatic and ruptured abdominal aortic aneurysms. *Eur J Vasc Endovasc Surg*, **33**, 401–407.
- UK Small Aneurysm Trial participants (1998). Mortality results for randomised controlled trial of early elective surgery or ultrasonographic surveillance for small abdominal aortic aneurysms. *Lancet*, **352**(9141), 1649–1655.
- UK Small Aneurysm Trial participants (2002). Long-term outcomes of immediate repair compared with surveillance of small abdominal aortic aneurysms. *N Engl J Med*, **346**(19), 1445–1452.
- Van Dam, E., Dams, S., Peters, G., Rutten, M., Schurink, G., Buth, J., and Van de Vosse, F. (2008). Non-linear viscoelastic behavior of abdominal aortic aneurysm thrombus. *Biomech Model Mechanobiol*, **7**, 127–137.
- van de Vosse, F. N., de Hart, J., van Oijen, C. H. G. A., Bessems, D., Gunther, T. W. M., Segal, A., Wolters, B. J. B. M., Stijnen, J. M. A., and Baaijens, F. P. T. (2003). Finite-element-based computational methods for cardiovascular fluid-structure interaction. *J Eng Math*, **47**(3-4), 335–368.
- van Marrewijk, C., Buth, J., Harris, P. L., Norgren, L., Nevelsteen, A., and Wyatt, M. G. (2002). Significance of endoleaks after endovascular repair of abdominal aortic aneurysms: The EUROSTAR experience. *J Vasc Surg*, **35**(3), 461–473.
- van Marrewijk, C. J., Fransen, G., Laheij, R. J. F., Harris, P. L., and Buth, J. (2004). Is a type II endoleak after EVAR a harbinger of risk? Causes and outcome of open conversion and aneurysm rupture during follow-up. *Eur J Vasc Endovasc Surg*, **27**(2), 128–137.

- van Straten, M., Venema, H. W., Streekstra, G. J., Reekers, J. A., den Heeten, G. J., and Grimbergen, C. A. (2003). Removal of arterial wall calcifications in CT angiography by local subtraction. *Med Phys*, **30**(5), 761–770.
- Veith, F. J., Baum, R. A., Ohki, T., Amor, M., Adiseshiah, M., Blankensteijn, J. D., Buth, J., Chuter, T. A. M., Fairman, R. M., Gilling-Smith, G., Harris, P. L., Hodgson, K. J., Hopkinson, B. R., Ivancev, K., Katzen, B. T., Lawrence-Brown, M., Meier, G. H., Malina, M., Makaroun, M. S., Parodi, J. C., Richter, G. M., Rubin, G. D., Stelter, W. J., White, G. H., White, R. A., Wisselink, W., and Zarins, C. K. (2002). Nature and significance of endoleaks and endotension: summary of opinions expressed at an international conference. *J Vasc Surg*, **35**(5), 1029–1035.
- Venkatasubramaniam, A. K., Fagan, M. J., Mehta, T., Mylankal, K. J., Ray, B., Kuhan, G., Chetter, I. C., and McCollum, P. T. (2004). A comparative study of aortic wall stress using finite element analysis for ruptured and non-ruptured abdominal aortic aneurysms. *Eur J Vasc Endovasc Surg*, **28**(2), 168–176.
- Verhoeven, E., Kapma, M., Groen, H., Tielliu, I., Zeebregts, C., Bekkema, F., and van den Dungen, J. (2008). Mortality of ruptured abdominal aortic aneurysm treated with open or endovascular repair. *J Vasc Surg*.
- Vorp, D. (2007). Biomechanics of abdominal aortic aneurysm. *J Biomech*, **40**, 1887–1902.
- Vorp, D. A., Raghavan, M. L., and Webster, M. W. (1998). Mechanical wall stress in abdominal aortic aneurysm: influence of diameter and asymmetry. *J Vasc Surg*, **27**(4), 632–639.
- Vorp, D. A., Lee, P. C., Wang, D. H., Makaroun, M. S., Nemoto, E. M., Ogawa, S., and Webster, M. W. (2001). Association of intraluminal thrombus in abdominal aortic aneurysm with local hypoxia and wall weakening. *J Vasc Surg*, **34**(2), 291–299.
- Wang, D. H. J., Makaroun, M. S., Webster, M. W., and Vorp, D. A. (2002). Effect of intraluminal thrombus on wall stress in patient-specific models of abdominal aortic aneurysm. *J Vasc Surg*, **36**(3), 598–604.
- Westerhof, N., Bosman, F., de Vries, C. J., and Noordergraaf, A. (1969). Analog studies of the human systemic arterial tree. *J Biomech*, **2**, 121–143.
- Westerhof, N., Elzinga, G., and Sipkema, P. (1971). An artificial arterial system for pumping hearts. *J Appl Physiol*, **31**(5), 776–781.
- White, G. H. and May, J. (2000). How should endotension be defined? History of a concept and evolution of a new term. *J Endovasc Ther*, **7**(6), 435–438.
- White, G. H., Yu, W., May, J., Chaufour, X., and Stephen, M. S. (1997). Endoleak as a complication of endoluminal grafting of abdominal aortic aneurysms: classification, incidence, diagnosis, and management. *J Endovasc Surg*, **4**(2), 152–68.

- White, G. H., May, J., Waugh, R. C., Chaufour, X., and Yu, W. (1998). Type III and type IV endoleak: toward a complete definition of blood flow in the sac after endoluminal AAA repair. *J Endovasc Surg*, **5**(4), 305–309.
- Wills, A., Thompson, M. M., Crowther, M., Sayers, R. D., and Bell, P. R. F. (1996). Pathogenesis of abdominal aortic aneurysms – cellular and biochemical mechanisms. *Eur J Vasc Endovasc*, **12**(4), 391–400.
- Wink, O., Niessen, W. J., Frangi, A. J., Verdonck, B., and Viergever, M. A. (2002). 3D MR coronary axis determination using a minimum cost path approach. *Magnet Reson Med*, **47**, 1169–1175.
- Wolf, Y. G. and Bernstein, E. F. (1994). A current perspective on the natural history of abdominal aortic aneurysms. *Cardiovasc Surg*, **2**(1), 16–22.
- Wolters, B. J. B. M., Rutten, M. C. M., Schurink, G. W. H., Kose, U., de Hart, J., and Van de Vosse, F. N. (2005). A patient-specific computational model of fluid-structure interaction in abdominal aortic aneurysms. *Med Eng Phys*, **27**(10), 871–883.
- Wolters, B. J. B. M., Emmer, M., Rutten, M. C. M., Schurink, G. W. H., and van de Vosse, F. N. (2007). Assessment of endoleak significance after endovascular repair of abdominal aortic aneurysms: a lumped parameter model. *Med Eng Phys*, **29**, 1106–1118.
- Zienkiewicz, O. C. and Taylor, R. L. (2000). *The Finite Element Method – Volume 1: The Basis*. Butterworth-Heinemann, Oxford, 5th edition.

Appendix A

Appendices to Chapter 2

A.1 Centreline description

Depending on their orientation with respect to the apex of the boundary surface, different line sections of the original centrelines are assigned to either the trunk of the bifurcation or its left and right branches. Further, the proximal end point of the trunk line is chosen distal to the branch points of the renal arteries, and the distal end point is chosen near the split point of the original centrelines. The proximal end points of the branch lines are determined as the centreline points that are closest to the apex of the boundary surface, and the distal end-points are chosen proximal to the iliac bifurcations (see Figure 2.2(c)).

Of each of the trunk and branch lines, a continuous description is determined using piecewise cubic Hermite interpolation (Fritsch and Carlson, 1980). Initially, each of the lines is described by a set of discrete points $\{\mathbf{x}_0, \mathbf{x}_1, \dots, \mathbf{x}_i, \dots, \mathbf{x}_{n-1}, \mathbf{x}_n\}$, with $\mathbf{x}_i = (x_{1,i}, x_{2,i}, x_{3,i})$ the coordinates of point i and n the number of points. By interpolation of each of the coordinate sequences, for every line an interpolating function C is derived that for every interval $[\mathbf{x}_i, \mathbf{x}_{i+1}]$ can be written as

$$C_i = \begin{pmatrix} a_{1,i}\theta_i^3 + b_{1,i}\theta_i^2 + c_{1,i}\theta_i + d_{1,i} \\ a_{2,i}\theta_i^3 + b_{2,i}\theta_i^2 + c_{2,i}\theta_i + d_{2,i} \\ a_{3,i}\theta_i^3 + b_{3,i}\theta_i^2 + c_{3,i}\theta_i + d_{3,i} \end{pmatrix}, \quad (\text{A.1})$$

where $0 \leq \theta_i \leq 1$, $C_i(0) = \mathbf{x}_i$ and $C_i(1) = \mathbf{x}_{i+1}$, with θ_i the interpolation parameter on the interval, and with $a_{j,i}|_{j=1,2,3}$, $b_{j,i}|_{j=1,2,3}$, $c_{j,i}|_{j=1,2,3}$ and $d_{j,i}|_{j=1,2,3}$ the function coefficients. The interpolation parameter and the index i are related to the relative axial position t along the centreline through the following expressions:

$$\begin{aligned} i &= (n-1)t - \text{mod}((n-1)t, 1), \\ \theta_i &= \text{mod}((n-1)t, 1), \end{aligned} \quad (\text{A.2})$$

where $0 \leq t \leq 1$. In order to obtain smooth interpolating functions, prior to the interpolation, mild second-order penalised least squares smoothing according to Eilers (2003) is applied to the original coordinate data.

A.2 Mesh transformation

By an initial transformation, the fluid domain is reshaped to a mother channel with two parallel daughter channels (see Figure A.1(a)). The lengths of the channels are determined by the lengths of the reconfigured centrelines. In this respect, the mother channel is extended by the distance between the distal trunk line end point and the initial mesh apex, defined in between the proximal branch line end points (see Figure 2.2(c)). The distance between the latter points is applied as the distance between the daughter channel mid-lines. The channel diameters are defined by setting the radius of curvature at the bifurcation equal to the daughter channel radius.

Along the centrelines, local coordinate systems $(\mathbf{n}_1, \mathbf{n}_2, \mathbf{n}_3)$ are defined as depicted in Figure A.1(b). At a certain axial position, \mathbf{n}_3 is determined from the local centerline tangent \mathbf{t} as

$$\mathbf{n}_3(t) = -\frac{\mathbf{t}(t)}{\|\mathbf{t}(t)\|_2} = -\frac{\partial \mathbf{C}(t)}{\partial t} \left(\left\| \frac{\partial \mathbf{C}(t)}{\partial t} \right\|_2 \right)^{-1}. \quad (\text{A.3})$$

The axis \mathbf{n}_1 is defined as the normalised projection of \mathbf{a}_1 onto the plane perpendicular to \mathbf{n}_3 , where \mathbf{a}_1 is defined as the vector from the apex to the proximal end point of the left branch line (see Figure A.1(b)). Further, \mathbf{n}_2 is defined as the outer product of \mathbf{n}_3 and \mathbf{n}_1 :

$$\mathbf{n}_2(t) = \mathbf{n}_3(t) \times \mathbf{n}_1(t). \quad (\text{A.4})$$

The vector \mathbf{a}_1 is also treated as an axis of a coordinate system $(\mathbf{a}_1, \mathbf{a}_2, \mathbf{a}_3)$ defined at the apex (see Figure A.1(b)). The axis \mathbf{a}_3 is defined as the normalised projection onto the plane normal to \mathbf{a}_1 of the averaged tangent at the proximal branch line end points. Further, \mathbf{a}_2 is defined by

$$\mathbf{a}_2 = \mathbf{a}_3 \times \mathbf{a}_1. \quad (\text{A.5})$$

Further, the trunk line and its local coordinate system are extended towards the apex by a third order polynomial curve that fits both the trunk line tangent and \mathbf{a}_3 (see Figure 2.2(c)).

For every cross section of the initially transformed mesh, as a function of the axial position t along the considered mesh part (see Figure A.1(a)), a rotation matrix \underline{R} is defined determining its orientation in the fully transformed mesh. For the trunk, \underline{R} is directly defined as:

$$\underline{R}(t) = [\mathbf{n}_1(t) \ \mathbf{n}_2(t) \ \mathbf{n}_3(t)], \quad (\text{A.6})$$

with $\mathbf{n}_j(t)|_{j=1,2,3}$ the column representation of $\mathbf{n}_j(t)$. For the branches, to obtain a smooth transition near the apex, \underline{R} is defined by interpolation with the apex local coordinate system:

$$\underline{R}(t) = (1-t) [\underline{\mathbf{a}}_1 \ \underline{\mathbf{a}}_2 \ \underline{\mathbf{a}}_3] + t [\mathbf{n}_1(t) \ \mathbf{n}_2(t) \ \mathbf{n}_3(t)]. \quad (\text{A.7})$$

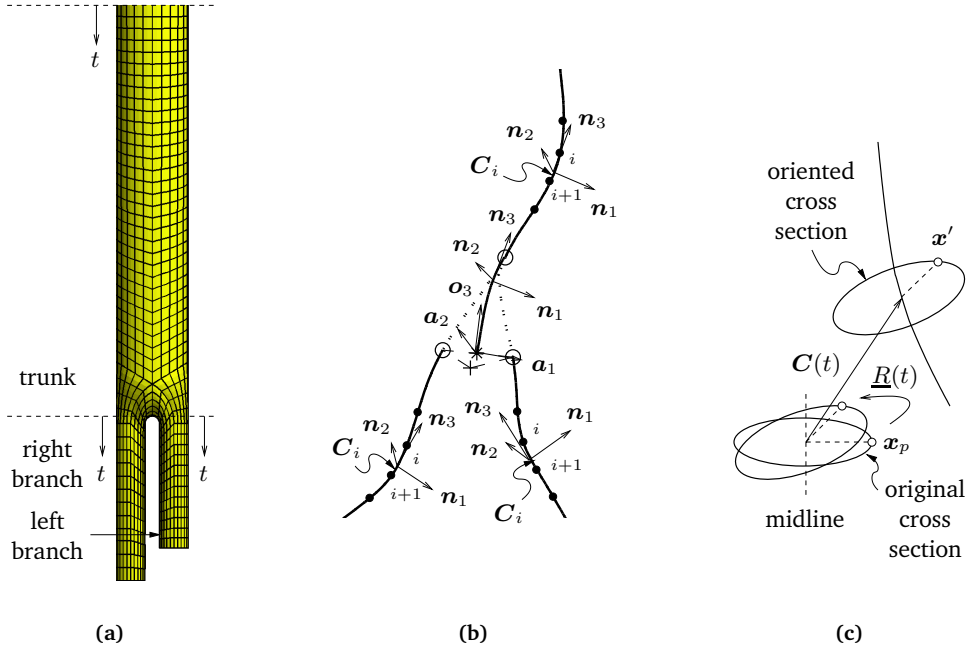


Figure A.1: Fluid domain of the standardised mesh after initial transformation (a); centreline-based local coordinate systems (b); orientation of a mesh cross section (c).

The complete transformation of a cross section can then be written as:

$$\underline{x}' = \underline{R}(t) \underline{x}_p + \underline{C}(t), \quad (\text{A.8})$$

with $\underline{x}_p = (x_{1,p}, x_{2,p}, 0)$ the in-plane position of a cross section point with respect to the mid-line of the considered mesh part, and x' its position in the transformed mesh (see Figure A.1(c)).

A.3 Point-surface projection

The projection distance d of a point x to the triangulated boundary surface is determined as follows. First, the closest vertex of the surface x_s is found. Next, the orthogonal projections of x onto the triangles connected to x_s are determined. Depending on the number of projections that exist, a local surface normal n and a projection vector v are calculated, distinguishing between the following cases (see Figure A.2).

- If no projections exist, for n , take the mean of the normals to all triangles attached to x_s ; for v , take the vector from x to x_s (see Figure A.2(a)).

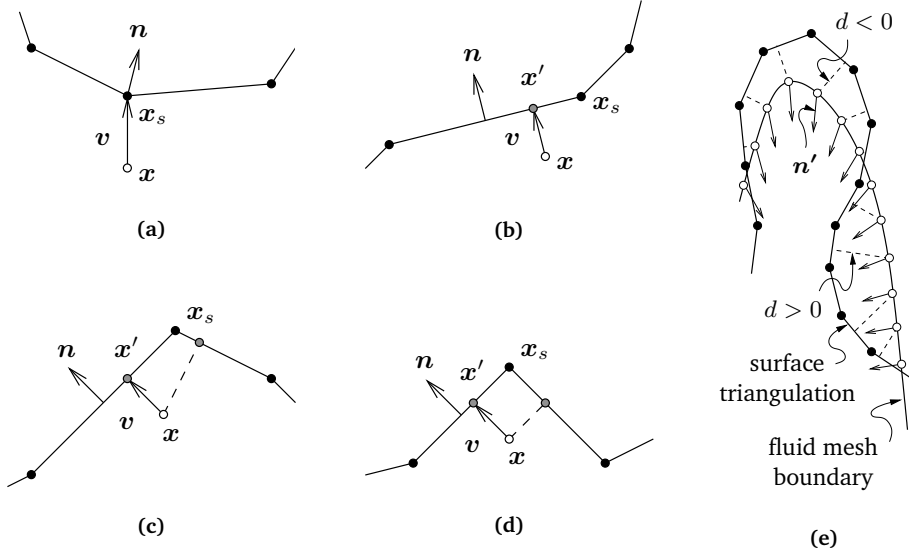


Figure A.2: 2-Dimensional analogs of the cases distinguished in the calculation of the surface normal n and the projection vector v as a function of the projected point x and the triangles connected to the closest vertex x_s (a-d); projection distance and smoothed surface normals of the fluid mesh boundary points (e).

- If only one projection x' exists, for n , take the outward normal to the triangle containing x' ; for v , take the vector from x to x' (see Figure A.2(b)).
- If two or more projections exist at varying distance from x , for x' , take the projection closest to x ; for n , take the outward normal to the triangle containing x' ; for v , take the vector from x to x' (see Figure A.2(c)).
- If two or more projections exist at equal distance from x , for x' , take either projection; for n , take the outward normal to the triangle containing x' ; for v , take the vector from x to x' (see Figure A.2(d)).

Finally, d is defined as

$$d = \text{sign}(n \cdot v) \|v\|_2. \quad (\text{A.9})$$

Depending on whether a point is located inside or outside the triangulation, d is positive or negative (see Figure A.2(e)). If d equals zero, the point is located on the triangulation itself.

Appendix B

Appendices to Chapter 5

B.1 Windkessel module parameters

The parameter R_c in Figure 5.1(d) accounts for the resistance of the vessel segment just distal to the connected tree end. Its value equals that of the characteristic impedance Z_c (see Westerhof *et al.*, 1971), defined by

$$Z_c = \sqrt{\frac{L_c}{C_c}}, \quad (\text{B.1})$$

with L_c and C_c the inertance and the compliance, respectively, of the connected tree end last segment. Further, R_p accounts for the resistance of the local periphery. Its value is determined as the remainder of Z_c subtracted from the total resistance of the represented vascular bed R_v :

$$R_p = R_v - Z_c. \quad (\text{B.2})$$

The value R_v is computed as a fraction of the systemic peripheral resistance R_s :

$$R_v = \frac{R_s}{f_q}, \quad (\text{B.3})$$

with f_q the fraction of the systemic flow associated with the considered body part (see Table B.1). The value of R_s is computed as a desired systemic mean pressure \bar{p} divided by the mean flow \bar{q} of a flow signal prescribed at the input of the model:

$$R_s = \frac{\bar{p}}{\bar{q}}. \quad (\text{B.4})$$

Finally, the parameter C accounts for the local peripheral compliance. Its value is determined from the time constant τ associated with the R_p, C -circuit, defined by

$$\tau = R_p C. \quad (\text{B.5})$$

Table B.1: Distribution of the systemic flow among the body parts represented by the Windkessel modules of the lumped parameter model (based on McArdle *et al.*, 1996).

| body part | fraction of the systemic flow |
|--------------------------------|-------------------------------|
| upper body: | |
| brain right side and right arm | 0.19 |
| brain left side | 0.07 |
| left arm | 0.12 |
| liver | 0.27 |
| kidneys | 0.22 |
| legs | 0.13 |

This so-called RC-time indicates at what rate the modelled fluid volume stored in the capacitor is released through the resistor. Of each of the different Windkessel modules, the RC-time is set equal to the RC-time of the total system τ_s , defined by

$$\tau_s = R_s C_s, \quad (\text{B.6})$$

with R_s again the systemic peripheral resistance as defined by (B.4) and C_s the total systemic compliance. The systemic RC-time indicates the rate of decay of the systemic pressure during diastole. Its value is determined by estimating the value of C_s using the pulse pressure method proposed by Stergiopoulos *et al.* (1994). In this procedure, using a least-squares optimisation technique, C_s is determined such that the pressure response of an R_s, C_s -circuit to the flow signal to be prescribed at the input of the aortic tree model attains both the desired mean pressure \bar{p} and a desired pulse pressure Δp .

B.2 Physiologic model properties

The segmental module properties of the lumped parameter model depicted in Figure 5.1 are given in Table B.2. The Windkessel module properties are given in Table B.3.

B.3 Experimental model properties

The dimensions of the different tubular sections of the experimental setup depicted in Figure 5.3 upon which the segmental module properties of the lumped parameter model depicted in Figure 5.3(c) were based are given in Table B.4. The properties of the remaining elements of the model along with associated scaling factors as applied in the simulations are given in Table B.5.

Table B.2: Resistance (R), inductance (L), and capacitance (C) of the segmental modules of the physiologic lumped parameter model (after Westerhof *et al.*, 1969).

| module | artery | R 10^5 Pa s/m^3 | L $10^5 \text{ Pa s}^2/\text{m}^3$ | C $10^{-11} \text{ m}^3/\text{Pa}$ |
|--------|----------------------|--------------------------------|---|---|
| 1 | aorta ascendens | 0.0327 | 0.309 | 53.4 |
| 2 | aorta ascendens | 0.0358 | 0.322 | 51.0 |
| 3 | arcus aorta | 0.0971 | 0.533 | 29.6 |
| 4 | arcus aorta | 0.227 | 1.14 | 52.1 |
| 5 | aorta thoracalis | 0.397 | 1.74 | 59.7 |
| 6 | aorta thoracalis | 1.62 | 3.82 | 25.1 |
| 7 | aorta thoracalis | 2.31 | 4.18 | 22.5 |
| 8 | aorta abdominalis | 2.88 | 4.72 | 20.4 |
| 9 | aorta abdominalis | 1.06 | 0.716 | 3.62 |
| 10 | stent-graft | 4.22 | 2.86 | variable |
| 11 | stent-graft | 4.75 | 3.62 | variable |
| 12 | aorta abdominalis | 1.19 | 0.904 | 3.16 |
| 13 | a. iliaca communis | 24.4 | 14.3 | 6.88 |
| 14 | a. iliaca externa | 62.8 | 23.0 | 3.88 |
| 15 | a. iliaca externa | 27.0 | 9.94 | 1.72 |
| 16 | a. anonyma | 2.96 | 1.76 | 13.5 |
| 17 | a. carotis com. sin. | 14.4 | 24.0 | 7.12 |
| 18 | a. subclavia | 6.35 | 8.11 | 5.60 |
| 19 | a. coelica | 2.20 | 3.30 | 1.36 |
| 20 | a. renalis | 15.8 | 53.5 | 1.67 |

Table B.3: Characteristic resistance (R_c), peripheral resistance (R_p), and capacitance (C) of the Windkessel modules of the physiologic lumped parameter model.

| module | body part | R_c 10^8 Pa s/m^3 | R_p 10^8 Pa s/m^3 | C $10^{-10} \text{ m}^3/\text{Pa}$ |
|--------|-----------------------------------|----------------------------------|----------------------------------|---|
| A | brain right side and right arm | 0.468 | 7.39 | 19.6 |
| B | brain left side | 1.42 | 20.0 | 7.28 |
| C | left arm | 1.06 | 11.7 | 12.8 |
| D | liver | 1.27 | 52.0 | 34.6 |
| E | kidneys | 3.08 | 12.8 | 14.0 |
| F | legs | 2.84 | 21.6 | 7.23 |

Table B.4: Length (l) and radius (r) of different tubular sections of the experimental setup.

| section | material | l mm | r mm |
|---------|----------|-----------|-----------|
| 1 | plastic | 35 | 12.5 |
| 2 | PU | 25 | 12.5 |
| 3 | PU | 25 | 12.5 |
| 4 | PU | 35 | 12.5 |
| 5 | PU | 35 | 12.5 |
| 6 | glass | 40 | 12.0 |
| 7 | glass | 30 | 12.0 |
| 8 | glass | 30 | 12.0 |
| 9 | glass | 30 | 12.0 |
| 10 | glass | 40 | 12.0 |
| 11 | PU | 35 | 12.5 |
| 12 | PU | 35 | 12.5 |
| 13 | plastic | 35 | 12.5 |
| 14 | plastic | 40 | 7.0 |
| 15 | plastic | 40 | 7.0 |
| 16 | plastic | 40 | 7.0 |
| 17 | plastic | 40 | 7.0 |
| 18 | plastic | 40 | 7.0 |

Table B.5: Resistance (R) and capacitance (C) of different elements of the experimental lumped parameter model along with associated scaling factors as applied in the simulations.

| property | value | factor |
|---------------------|------------------------------|--------|
| R | 10^8 Pa s/m ³ | |
| endoleak channel: | | |
| small | 39 | 2.0 |
| medium | 3.2 | 5.0 |
| large | 0.73 | 10 |
| main tube outlet | 7.5 | - |
| silicone tube inlet | 3.0 | - |
| C | 10^{-9} m ³ /Pa | |
| main tube, per m | 9.9 | 0.84 |
| aneurysm | 2.3 | 0.57 |
| air chamber | 3.9 | - |

Samenvatting

Een aneurysma van de abdominale aorta (AAA) is een lokale verwijding van de aorta in de buik. Het scheuren, of ruptuur, van een AAA kan voor de patiënt een levensbedreigende situatie opleveren. Ruptuur van een gediagnosticeerd AAA kan voorkomen worden door het plaatsen van een reguliere vaatprothese met een open buikoperatie, of door het plaatsen van een zogenaamde endoprothese met een minimaal-invasieve ingreep (endovasculaire behandeling). Een open buikoperatie is een relatief zware ingreep voor de patiënt. Een geplaatste reguliere vaatprothese geeft echter een tamelijk duurzame afname van de kans op ruptuur. Endovasculaire behandeling daarentegen gaat gepaard met een relatief laag risico voor de patiënt. Na het plaatsen van een endoprothese is er echter een relatief grote kans op complicaties, waardoor patiënten na de operatie intensief gevolgd moeten blijven worden.

Bij de beslissing tot een chirurgische ingreep, moeten de risico's die gepaard gaan aan de ingreep zelf en aan eventuele complicaties achteraf worden afgewogen tegen de kans op ruptuur. Deze afweging is niet triviaal. In de huidige klinische praktijk wordt de ruptuurkans hoog geacht wanneer de diameter van een AAA groter is dan 5.5 cm. Er is echter geen garantie dat een kleiner AAA niet zal scheuren. Een groter AAA zou daarentegen stabiel kunnen blijven. Wat betreft complicaties achteraf bij endovasculaire behandeling is de belangrijkste complicatie die van endolekkage, ofwel lekkage naar de afgesloten holte van het AAA. Hoewel is aangetoond dat endolekkage leidt tot het voortbestaan van de kans op ruptuur en derhalve bestreden dient te worden, zijn de oorzaken en effecten van endolekkage op patiënt-specifieke basis nog onduidelijk.

De doelstellingen van het onderzoek beschreven in dit proefschrift zijn (1) het ontwikkelen van numerieke gereedschappen voor het verbeteren van klinische beslissingen in de behandeling van AAA en (2) het geven van inzicht in de mate van detaillering die benodigd is voor dergelijke modellen. Hierbij wordt in het bijzonder gebruik gemaakt van technieken voor het modelleren van vloeistof/vaste stof-interactie (FSI), waarbij wordt aangenomen dat deze kunnen helpen bij zowel het beter voorspellen van de ontwikkeling en de ruptuur van een onbehandeld AAA, als het bepalen van de effecten van endolekkage op de kans op ruptuur na behandeling. Deze doelstellingen zijn gebaseerd op eerdere studies waarin een verband is aangetoond tussen de kans op ruptuur en de numeriek berekende spanning in de vaatwand. Daarnaast bouwt dit onderzoek voort op eerdere studies naar mechanische en vloeistofdynamische grootheden in patiënt-specifieke modellen van AAA en op experimentele studies

naar de effecten van endolekkage op de druk in de afgesloten holte van het AAA na behandeling.

Met betrekking tot het modelleren van FSI in een onbehandeld AAA wordt onder andere een methode ontwikkeld voor het genereren van een patiënt-specifieke eindige elementen-mesh van het AAA lumen en de vaatwand. Het nut van een dergelijke mesh wordt geïllustreerd met een simulatie van de wandspanning, de snelheidsverdeling in het bloed, en de wandschuifspanning (WSS) in een karakteristiek AAA. Daarnaast wordt het belang van het meenemen van de initiële wandspanning onderzocht. In voorgaande studies van FSI in AAA werd de initiële spanning, ofwel de wandspanning die reeds aanwezig is bij de diastolische druk, niet meegenomen. Het blijkt echter dat het negeren van de initiële spanning leidt tot een overschatting van de wanddeformatie, het gemiddelde spanningsniveau, en de piekspanning. Daarnaast levert het een meer gladde spanningsverdeling op en leidt het tot een onderschatting van de WSS. Het blijkt echter ook dat de WSS bij het meenemen van de initiële spanning goed kan worden benaderd met behulp van een starre wand.

Met betrekking tot het modelleren van endolekkage worden onder andere de voordelen van zogenaamde lumped-parameter modellering ten opzichte van gekoppelde FSI onderzocht. Met beide typen van modellering wordt de druk in de afgesloten holte van een behandeld AAA bestudeerd als functie van de mate van endolekkage en de compliantie van de endoprothese. Uit de resultaten blijkt dat lumped-parameter modellering een goed en goedkoper alternatief biedt voor het modelleren van endolekkage met gekoppelde FSI en dat de druk in de holte van het AAA uitgerekend met een dergelijk model goed gebruikt zou kunnen worden als randvoorwaarde voor berekeningen aan de vaatwand voor het bepalen van de ruptuurkans na behandeling. Daarnaast wordt lumped-parameter modellering toegepast om verschillende resultaten van eerdere experimentele studies naar endolekkage met elkaar in overeenstemming te brengen. Hierbij blijkt dat bij endolekkage de gemiddelde druk in de holte van het AAA voornamelijk afhankelijk is van de weerstand van een eventueel verbonden uitstroomvat, terwijl de pulsatie van de druk afhankelijk is van zowel de grootte van het lek als de compliantie van de prothese.

De resultaten en conclusies van dit onderzoek zijn momenteel voornamelijk van belang in het kader van eerdere en toekomstige studies gericht op betere begripsvorming van de ontwikkeling en het ontstaan van AAA en de relevantie van endolekkage. Voor toepassing van de ontwikkelde modellen in de klinische praktijk, moeten de modellen verder ontwikkeld worden en moet de toegevoegde waarde van de gesimuleerde grootheden bij de klinische besluitvorming verder worden aangetoond. Echter, gebaseerd op de aangetoonde mogelijkheden voor het simuleren van de effecten van endolekkage met behulp van lumped-parameter modellering en voor het simuleren van de WSS bij meegenomen initiële wandspanning met behulp van een starre wand, kan worden geconcludeerd dat bij het simuleren van relevante grootheden voor de behandeling van AAA, FSI niet noodzakelijkerwijs expliciet hoeft te worden meegenomen. Met deze conclusie legt het huidige onderzoek de basis voor een vereenvoudiging van de te ontwikkelen numerieke gereedschappen die naar verwachting het effect ervan in de klinische praktijk positief zal beïnvloeden.

Dankwoord

Hoewel onderzoek op zich nooit af is, is er aan dit stukje dan toch een einde gekomen. Het behalen van dit einde heb ik niet in mijn eentje gedaan, en daarom wil ik bij deze graag een aantal mensen bedanken.

Ten eerste mijn promotor. Frans, met dit boekje komt er een einde aan een lange samenwerking. Vanaf mijn eerste stage heb ik al mijn wetenschappelijke bezigheden aan de TU bij jou in de buurt uitgevoerd, en dat was niet zonder reden. Je hebt een prettige manier van begeleiden, waarbij je veel vrijheid laat voor eigen invulling, en indien nodig nuttige input levert. Dit is voor mij een belangrijke voorwaarde geweest voor het kunnen opzetten en afronden van mijn promotie.

Ten tweede de copromotoren. Marcel, ook jou ben ik op de TU regelmatig blijven tegenkomen. We hebben veel technisch-inhoudelijke discussies gevoerd, waarbij de beoogde inpassing van het besprokene in het onderzoek nogal eens heeft gevarieerd. Terugkijkend heb je een grote bijdrage geleverd aan dit boekje, en dat zit in meer dan de (hopelijk) correcte toepassing van het Brits Engels. Geert Willem, ik geloof dat het voor ons allebei wennen was om elkaars taal te leren spreken. Hoewel sommige van de dingen die ik uiteindelijk bekeken heb misschien nog ver van de klinische praktijk af liggen, heb ik genoten van onze discussies, en heb ik het gewaardeerd om een kijkje te kunnen nemen in de wereld van de witte jassen.

Natuurlijk ook alle anderen die, op welke wijze dan ook, hebben bijgedragen aan de inhoud van dit proefschrift. Iedereen die bij het Hemodyn-project betrokken is geweest wil ik bedanken voor het mogelijk maken van een groter geheel waaraan ik mijn eigen steentje kon bijdragen. Daarnaast wil ik alle kamergenoten en collega's die ik in de loop van de jaren gehad heb bedanken voor alle gezelligheid en afleiding, en voor het al dan niet informeren naar de voortgang. Verder wil ik mijn stagiairs en afstudeerders bedanken voor de prettige ervaringen die ik zelf als begeleider heb opgedaan. Marcia, zonder jou had hoofdstuk 5 er heel anders uitgezien!

En als laatste, maar zeker niet als minste, mijn vrienden en familie. Bedankt voor jullie steun, in welke vorm dan ook, en bedankt dat jullie ervoor zorgen dat er meer is in het leven dan promoveren alleen. Juist dit heeft ervoor gezorgd dat ik een punt kan zetten aan het eind van deze zin, en hierna weer fris aan nieuwe hoofdstukken kan beginnen.

Berent Wolters, 1 maart 2009

Curriculum vitae

Berent Wolters werd op 28 juni 1976 geboren te Eindhoven. In 1994 behaalde hij zijn Gymnasiumdiploma aan het Van Maerlantlyceum in Eindhoven. Vervolgens begon hij aan de Technische Universiteit Eindhoven aan de opleiding Werktuigbouwkunde. In 1999 liep hij stage aan het Department of Aeronautics van Imperial College in Londen, waar hij onderzoek deed naar het numeriek modelleren van vloeistof/vaste stof-interactie in bloedvaten. In 2000 behaalde hij zijn ingenieursdiploma. Zijn afstudeerproject had als onderwerp de invloed van vaatbeweging op de wandschuifspanning in kransslagaders. In 2001 begon hij aan een promotie-onderzoek in de groep Cardiovascular Biomechanics van de faculteit Biomedische Technologie van de Technische Universiteit Eindhoven. De resultaten van dit onderzoek staan beschreven in dit proefschrift. Tussen 2005 en 2007 was Berent werkzaam bij TNO DIANA BV in Delft. Vanaf april 2007 is hij werkzaam bij Philips Applied Technologies in Eindhoven.